August 27, 1975

To the Graduate Council:

I am submitting herewith a thesis written by Upender Krishen Kaul entitled "Turbulent Atmospheric Flow Over a Backward-Facing Step." I recommend that it be accepted in partial fulfillment of the requirements for the degree of Master of Science, with a major in Mechanical Engineering.

Walter Frost

Walter Frost, Major Professor

We have read this thesis
and recommend its acceptance:

James R. Maus

Jami-Yeh Wu

H.C. Reddy

Accepted for the Council:

Hilton A. Smith

Vice Chancellor
Graduate Studies and Research

A

TURBULENT ATMOSPHERIC FLOW OVER A BACKWARD-FACING STEP

A Thesis

Presented for the

Master of Science

Degree

The University of Tennessee

Upender Krishen Kaul

December 1975

1266339

ACKNOWLEDGMENTS

The work reported herein was supported by the National Aeronautics and Space Administration, Marshall Space Flight Center, Aerospace Environment Division, under the contract number NAS8-29584, and by the National Science Foundation, Engineering Division, Fluid Mechanics Program, under the contract number GK 42992.

The author wishes to especially thank Dr. George H. Fichtl of the Marshall Space Flight Center for his cooperation and valuable suggestions in carrying out this investigation.

The author is deeply grateful to his advisor, Dr. Walter Frost, for his constant encouragement and guidance throughout the course of this project. Thanks are due Dr. Jain-Ming Wu, Dr. James R. Maus, Jr., and Dr. K. C. Reddy for their helpful suggestions. The assistance given by Mr. Juergen Bitte in computer programming is sincerely appreciated.

The author would also like to thank Mrs. Jeannie Harper for her excellent typing.

ABSTRACT

The phenomenon of atmospheric shear layer separation over a man-made structure such as a building (modeled as a backward-facing step) has been analyzed theoretically by (1) solving the two-dimensional equations of motion in the two variables, stream function and vorticity, and (2) employing an approximate integral technique. Boundary conditions for the undisturbed flow are that of the turbulent atmospheric shear flow over a rough terrain.

1. In this approach a two-equation model of turbulence, which was used at higher Reynolds number, introduces two more conservation equations into the analysis. These elliptic partial differential equations for the vorticity, stream function, turbulence kinetic energy, and turbulence length scale are solved by a finite-difference technique developed by Gosman, et al., at the Imperial College of Science and Technology, London.

The predicted results are reasonable, and the recirculation zone length behind the step is found to be realistic.

2. The approximate technique which integrates the horizontally-directed momentum equation

utilizes empirical information about the flow field behind the backward-facing step. Recirculation zone velocity profile is assumed to follow a polynomial expression which satisfies prescribed matching conditions at the dividing mean streamline and some governing boundary conditions.

The presence of the corner eddy is predicted to be in the region of negative surface pressure gradient. The magnitude of the reversed flow velocity in the recirculation eddy has been found to agree with that found from experiments. Also, a surface eddy viscosity distribution has resulted in the method which realistically follows the magnitude of the surface pressure gradient distribution as found experimentally.

TABLE OF CONTENTS

CHAPTER		PAGE
I.	INTRODUCTION AND STATEMENT OF THE PROBLEM.	1
II.	THEORETICAL REVIEW	3
	Separation	3
	Mechanics of the Flow Region	6
	Flow between separation and reattachment . . .	6
	Flow downstream of reattachment.	15
	Review of Analytical Models.	29
III.	SOLUTION OF GENERAL NAVIER-STOKES EQUATIONS AS APPLICABLE TO ATMOSPHERIC FLOW.	64
	Governing Equations for the Turbulent Atmospheric Flow	64
	Boundary Conditions for the Atmospheric Shear Flow	66
	Eddy Viscosity Model	66
	Prandtl-Kolmogorov Model of Turbulence	68
	Algebraic equations for the transport properties	68
	Equations to be Solved	69
	Derivation of the Finite Difference Equation . .	73
	Complete Successive Substitution Formula	79
	Setting up and Discussion of the Boundary Conditions	81

CHAPTER PAGE

Algebraic equations for and substitution formulae derived from the boundary conditions 83

Boundary conditions for the stream function 84

Boundary conditions for the vorticity. . . . 86

Boundary conditions for the turbulence kinetic energy 90

Boundary conditions on ℓ 96

Numerical Solution of the Finite Difference Equation 96

Grid Distribution. 99

Selection of Constants 99

Discussion on Convergence, Accuracy, and Economy of the Solution Procedure. 102

Convergence. 102

Accuracy and economy 107

Discussion of Results. 110

Laminar solution (Reynolds number as a parameter) 111

Eddy viscosity model (Reynolds number as a parameter) 119

TKL model. 123

Conclusions and Summary. 134

CHAPTER PAGE

IV. APPROXIMATE INTEGRAL TECHNIQUE 136

Empirical Information. 136

Governing Boundary Conditions for the Problem. 138

Normalized Form of the Equations to be Solved 147

Correlation of the Spreading Rate Parameter with the Experimental Data 149

Solution Procedure 151

Comments on Convergence, Accuracy, and Economy of the Integral Method 152

Discussion of Results. 154

Suggestions to Improve the Model 159

BIBLIOGRAPHY 162

APPENDIX 169

VITA 173

LIST OF FIGURES

FIGURE		PAGE
2- 1.	Separation of the Boundary Layer [22]	5
2- 2.	Definition of Flow Zones Near a Sharp-Edged Building [2].	7
2- 3.	General Behavior of Typical Reattaching Flow [4].	10
2- 4.	Separated Flow Model Over a Backward-Facing Step [8].	10
2- 5.	Pressure Distribution on the Step Face and the Bottom Face [8]	11
2- 6.	Distribution of Streamwise Mean Velocity, Turbulence Intensity, and Turbulent Shear Stress Behind a Backward-Facing Step [8]. . .	13
2- 7.	Maximum Shear Stress in Shear Layer [4]	16
2- 8.	Velocity Profiles in Air Flow Past Roughness Elements [10]	23
2- 9.	Downstream Redevelopment of Mean Flow [10]. . .	24
2-10.	Turbulent Shear-Stress Profile at x/k = 4.5 Behind 0.75-inch Element [10]	24
2-11.	Turbulence Profiles Behind Roughness Elements [10]	26
2-12.	Downstream Variation in Turbulence Quantities [10]	27

FIGURE PAGE

2-13. Static Pressure Measured Through the Wake Behind a Bluff Plate [2]. 28

2-14. Flow Model for Derivation of the Second Outflow Function [17] 31

2-15. The Subsonic Steady Base Flow Past a Blunt Body; Mean Streamlines and Pressure Distribution, Schematically [17]. 32

2-16. Velocity Profile in the Mixing Region at the End of the Outflow Region [17]. 34

2-17. Influence of Wedge Angle on the Similarity Parameter of the Mixing Region for Incompressible Flow [17]. 36

2-18. Effect of Shear Layer Profile on Velocity Along Zero Streamline [27]. 41

2-19. Typical Static Pressure Variation on a Flat Plate in Supersonic Flow with Separation Induced by an Incident Shock Wave 43

2-20. Correlation of Velocity in the Shear Layer with Error Function Profile [2] 45

2-21. Flow Model for Pre-asymptotic Region [21] . . . 48

2-22. Pre-asymptotic Velocity Profile Description [21]. 49

2-23. Variation of Velocity Profile Slope at the Half-Free-Stream Velocity Point with Distance from Separation [21] 50

FIGURE PAGE

2-24. Comparison of Theory with Incompressible Measurements of Charwat and Der [21]. 52

2-25. Comparison of Different Velocity Profiles [19] 54

2-26. Illustration of the Matching of Various Profiles with the Common Scale as the Transverse Coordinate of the Error Function Profile [19]. 55

2-27. Free Shear Layer Model [20] 57

2-28. Streamline Coordinates System [34]. 60

2-29. Shearing Stress Along Zero Streamline [34]. . . 63

3- 1. Portion of the Finite-Difference Grid 65

3- 2. Distribution of the Mixing Length in the Flow Field Enclosed by the Control Volume 1-2-3-4-5-6-1 82

3- 3. Distribution of the Finite-Difference Grid Over the Entire Flow Field. 98

3- 4. Streamlines Over a Back Step in Laminar Flow (Reynolds Number = 6.9) 112

3- 5. Streamlines Over a Back Step in Laminar Flow (Reynolds Number = 69). 113

3- 6. Streamlines Over a Back Step in Laminar Flow (Reynolds Number = 6.9×10^3) 114

3- 7. Flow Direction Over a Back Step in Laminar Flow (Reynolds Number = 6.9). 115

FIGURE PAGE

3- 8. Flow Direction Over a Back Step in Laminar Flow (Reynolds Number = 69) 116

3- 9. Flow Direction Over a Back Step in Laminar Flow (Reynolds Number = 6.9×10^3) 117

3-10. Streamlines Over a Back Step in Turbulent Flow Using the Eddy Viscosity Model (Reynolds Number = 6.9×10^6) 122

3-11. Streamlines Over a Back Step in Turbulent Flow Using the TKL Model (Reynolds Number = 6.9×10^6), $C_{\mu_\infty} = 1.0$, $C_{b_\infty} = C_{d_\infty} = 0.1$, $C_s = 1.0$. 126

3-12. Streamlines Over a Back Step in Turbulent Flow Using the TKL Model (Reynolds Number = 6.9×10^6), $C_{b_\infty} = C_{d_\infty} = C_{\mu_\infty} = 0.1$, $C_s = 1.0$ 127

3-13. Streamlines Over a Back Step in Turbulent Flow Using the TKL Model (Reynolds Number = 6.9×10^6), $C_{\mu_\infty} = 0.08$, $C_{b_\infty} = C_{d_\infty} = 0.1$, $C_{s_\infty} = 1.0$. . . . 128

3-14. Streamlines Over a Back Step in Turbulent Flow Using the TKL Model (Reynolds Number = 6.9×10^6), $C_{\mu_\infty} = 0.05$, $C_{b_\infty} = C_{d_\infty} = 0.1$, $C_{s_\infty} = 1.0$. . . . 129

FIGURE PAGE

3-15. Streamlines Over a Back Step in Turbulent Flow Using the TKL Model (Reynolds Number = 6.9×10^6), $C_{\mu_\infty} = 0.1$, $C_{b_\infty} = C_{d_\infty} = 1.0$, $C_{s_\infty} = 0.5$ 130

3-16. Streamlines Over a Back Step in Turbulent Flow Using the TKL Model (Reynolds Number = 6.9×10^6), $C_{\mu_\infty} = 0.1$, $C_{d_\infty} = C_{b_\infty} = 1.0$, $C_{s_\infty} = 0.4$ 131

3-17. Streamlines Over a Back Step in Turbulent Flow Using the TKL Model (Reynolds Number = 6.9×10^6) $C_{\mu_\infty} = 0.1$, $C_{b_\infty} = C_{d_\infty} = 1.0$, $C_{s_\infty} = 0.35$ 133

4- 1. Variation of Surface Pressure Coefficient Behind a Back Step [8] 137

4- 2. Model of Separated Flow Over a Back Step . . . 139

4- 3. Illustration of the Conservation of Momentum Principle. 141

4- 4. Velocity Profiles in the Recirculation Zone, the New Shear Layer and the Initial Boundary Layer 143

4- 5. Illustration of the Matching of the Error Function and Power Law Profiles in the Base Region 153

4- 6. Velocity Profiles Behind a Back Step 155

FIGURE PAGE

4- 7. Variation of Surface Pressure Gradient and Surface Eddy Viscosity Behind a Back Step . . 156

4- 8. Variation of the Nondimensional Maximum Shear Stress in the Shear Layer with the Nondimensional Distance Along the Ground. . . 160

NOMENCLATURE

x,z	Horizontal and vertical Cartesian coordinates, respectively
p	Local pressure
p_r	Reference pressure in the undisturbed flow
ρ	Density
κ	von Karman universal constant (= 0.4)
u^*	Friction or shear stress velocity, $(\tau_w/\rho)^{1/2}$
z_0	Surface roughness length
μ	Laminar absolute viscosity of the fluid
ν	Laminar kinematic viscosity of the fluid
τ	Shear stress
u_r	Reference velocity in the undisturbed flow
C_p	Coefficient of pressure defined as $(p-p_r)/\frac{1}{2}\rho u_r^2$
h	Height of the step
h_0	Height of the control volume (Figure 3-2)
R	Local Reynolds number
R_t	Reynolds number of turbulence, $\rho k^{1/2}\ell/\mu$
ℓ	Prandtl mixing length or local turbulence length scale
k	Turbulence kinetic energy
ω	Two-dimensional fluid vorticity (Equation (3.13))
ψ	Stream function (Equations (3.14) and (3.15))
C_μ	Function in the expression for effective viscosity (Equation (3.9))

C_d Function in the source term for turbulence kinetic energy (Table 3-2)

C_b, C_s Functions in the source term for turbulence length scale (Table 3-2)

a,b,c Coefficients in the general elliptic equation (Equation (3.16))

d Source term in the general elliptic equation (Equation (3.16))

ϕ Dependent variable of the general elliptic equation

$\sigma_{k,eff}$ Effective Schmidt number for turbulence energy

$\sigma_{\ell,eff}$ Effective Schmidt number for turbulence length scale

Γ_{false} False exchange coefficient (Equation (3.56))

$\Gamma_{k,eff}$ Effective exchange coefficient for turbulence kinetic energy, $\mu_{eff}/\sigma_{k,eff}$

$\Gamma_{\ell,eff}$ Effective exchange coefficient for turbulence length scale

$\Delta x, \Delta z$ Numerical step sizes in the x- and z-directions, respectively

W_{skt} Rate of generation of turbulence kinetic energy by turbulent shear stresses (Table 3-2)

Subscripts

i,0 Pertain to the inlet and outlet of the control volume (Figure 3-2)

w,s Pertain to the solid wall

P	Pertains to the node at which the dependent variable is being calculated currently
NP	Refers to a node lying adjacent to a boundary node
E,W,N,S	Refer to the neighboring nodes which lie east, west, north, and south of the node P, respectively
t	Denotes a turbulent flow quantity
eff	Denotes an effective transport property comprising both turbulent and laminar parts
∞	Refers to a quantity when turbulence Reynolds number tends to infinity
r	Pertains to a reference quantity in the undisturbed flow
*	Denotes a dimensionless quantity
1,2,3	Finite difference indices (Figure 3-3)
IN,JN,	Finite difference indices (Figure 3-3)
INM,JNM	Finite difference indices (Figure 3-3)

Superscripts

*	Refers to shear stress (friction) velocity
'	Denotes fluctuations in the mean velocity components, u and v
$\bar{}$	Time averaging
n	Index of iteration

CHAPTER I

INTRODUCTION AND STATEMENT OF THE PROBLEM

The study of atmospheric flow over buildings or other man-made surface obstructions has gained momentum in recent years due to the possibility of the operation of short take-off and landing (STOL) aircraft in addition to helicopters from within the heart of a city. Unsteady flow phenomena such as induced vortex fields, cross-winds, and separated flows near these obstructions pose a danger to the operation of low-speed aircraft, especially in a strong turbulent wind. In fact, some accidents involving small aircraft while taking off from or landing in around airport terminal buildings have been traced to these flow phenomena. In structural design of buildings or bridges the civil engineer has always been concerned about the dynamical loads induced by these complex flow phenomena on such structures, for the lack of understanding of which, a conservative factor of safety has been used in their design. Even then, occasional incidents of glass panes being shattered out of buildings in strong winds have been reported. Aero-elastic phenomena such as buffeting and stalling arise primarily out of the separation phenomenon. Vibration problems involved with the collapse of the Tacoma Narrows bridge stemmed from these flow phenomena in a strong turbulent wind. There have

also been reports of severely unpleasant situations around downtown shopping centers due to strong recirculating flow behind the buildings.

These flow phenomena are so complex that they have to be dealt with separately. In this study the problem of flow separation behind an obstruction, its reattachment to the ground, and the recirculating flow in the cavity or the wake zone thus formed has been investigated and solved by considering the simple configuration of a rearward-facing step. Some experimental data are available for such an obstruction and permit computational solutions to be compared with experimental findings. To simplify the problem further only two-dimensional flow is considered.

The problem has been attacked two ways. While the first method is the solution of general Navier-Stokes equations as applicable to turbulent atmospheric flow, the second approach is an integral technique to predict the velocity profiles in the recirculation region by making use of the experimentally known pressure fields. From the former approach vorticity and stream function are obtained as a solution without taking recourse to the knowledge of pressure. However, once the solution is obtained, pressure field can readily be achieved.

CHAPTER II

THEORETICAL REVIEW

In this chapter major theories that have been put forward to predict the separation phenomenon of laminar and turbulent flows over an obstacle are discussed. Results from experiments conducted by various authors are reviewed to furnish appropriate empirical data in terms of constants and parameters which are used in both approaches to the numerical solution of the problem presented herein.

This chapter is divided into three sections. In the first section an introductory paragraph about the phenomenon of separation is given. In the second section the mechanics of the flow region between separation and reattachment and that downstream of reattachment is reviewed. In the third section various analytical models as proposed by different authors to predict the parameters associated with the laminar and turbulent separation, for example, velocity, eddy viscosity and turbulence intensity in the free shear layer, and base pressure are discussed.

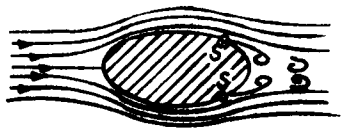
I. SEPARATION

The phenomenon of separation occurs due to the presence of either viscosity and a pressure gradient or of an abrupt change of geometry. In the latter case, on most

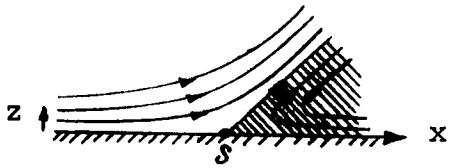
structures, it occurs from the sharp edges. Separated flows are formed, for example, upstream of a forward-facing step, downstream of a backward-facing step, within a cutout in a body surface, and on the upper surface of an airfoil at high angle of attack.

When a two-dimensional flow separates due to viscosity in an adverse pressure gradient, retardation of the fluid close to the surface causes a rapid thickening of the boundary layer. The point where the velocity gradient at the surface in the direction normal to the wall decreases to zero is defined as the point of separation. Downstream of this point flow reversal takes place near the surface (Figure 2-1). At the separation point the shear stress is reduced to zero. Experimentally, the occurrence of zero shear stress and the flow reversal near the surface has been found for strictly a steady, two-dimensional, incompressible laminar flow. When turbulence and three-dimensional effects, as in the case of a building, are introduced, this phenomenon is not well defined.

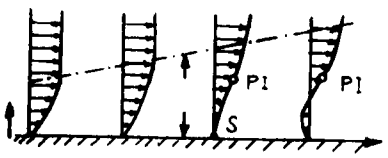
Rearward-facing step-flow separation is characterized by a relatively small angle of incidence between the streamline and the body at the point of separation and at the point of reattachment; but in the case of bluff-body-flow separation, the streamline at separation and reattachment points is inclined almost perpendicularly to the body and the reattaching surface. The step-flow and



(a) Flow past a body with separation
(S = point of separation)



(b) Shape of streamlines near point of separation



$$\left(\frac{\partial u}{\partial z}\right)_0 > 0; \quad \left(\frac{\partial u}{\partial z}\right)_0 = 0; \quad \left(\frac{\partial u}{\partial z}\right)_0 < 0$$

(c) Velocity distribution near the point of separation
(PI = point of inflection)

Figure 2-1. Separation of the boundary layer [22].

bluff-body-flow types of separation arise due to an abrupt geometrical change in configuration of the body. Separation bubbles on airfoils occur due to the dynamical interactions of viscosity and an adverse pressure gradient which sets up recirculating motion on the airfoil surface.

The flow separation depends heavily on whether the flow is laminar, turbulent, or transitional. In subsonic flow pure laminar separated flow does not hold any practical importance [1];[1] but for compressible flow, and especially at higher Mach number, laminar separation is important, since it is very stable and may persist to high Reynolds numbers. In this study, however, only low Mach number incompressible flow is considered.

II. MECHANICS OF THE FLOW REGION

Flow Between Separation and Reattachment

Shear and turbulence in the incident flow are two important features of flow separation around a surface obstruction. The distorted flow over a block geometry building consists of a displacement zone, a wake region which encloses the rear separation bubble, and an upstream separation bubble (Figure 2-2). Shear generates a swirling flow in the wake or cavity zone, which can be interpreted as the accumulation of vortex lines in the wake region by the

---

[1]Numbers in brackets refer to similarly numbered references in the bibliography.

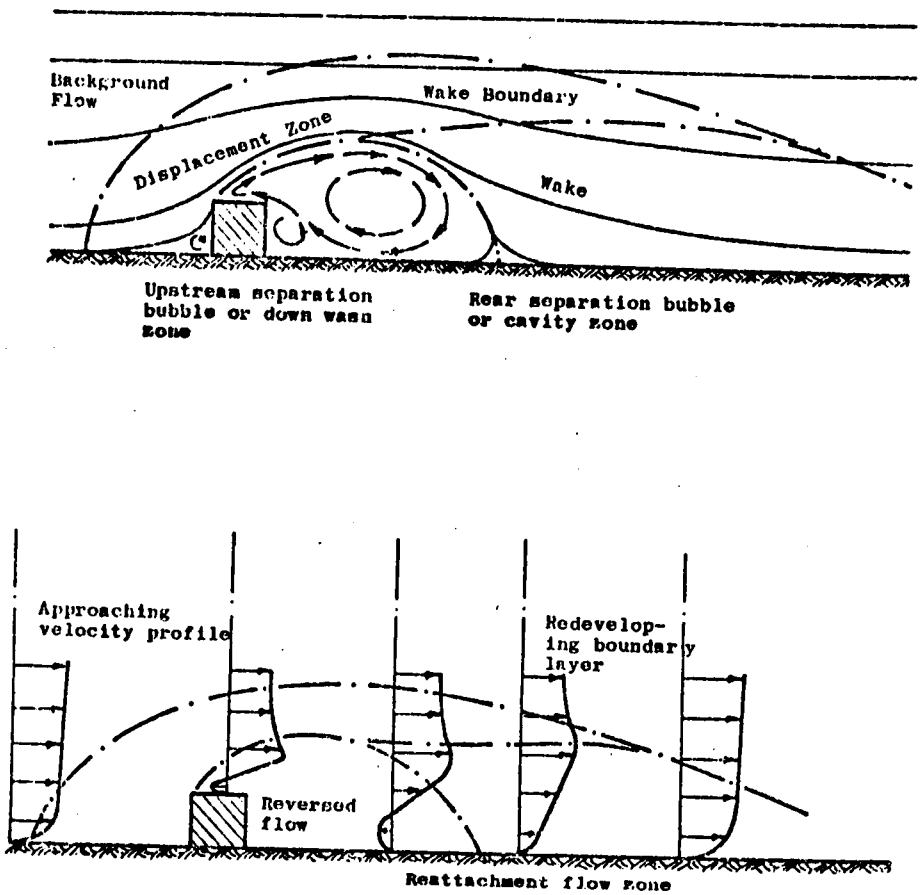


Figure 2-2. Definition of flow zones near a sharp-edged building [2].

passing flow. Turbulence thickens the shear layer which encloses the wake region. For some distance over the obstruction, and in the wake zone, turbulence is very large. The fluctuating component can be as high as 40% of the steady component [2] and is generally largest on the edge of the shear layer. In most cases the vortices of the separated flow are unsteady, and their experimental study is difficult.

Wind tunnel studies of separation over rearward-facing steps and bluff geometries [1 through 11] provide some insight into the physical aspects of flow separation and recirculating flow formation in the cavity zone. When a two-dimensional turbulent flow separates from the sharp corner of a back step, a shear layer with high vorticity and low static pressure is formed which spreads linearly downstream (for steady, two-dimensional laminar flow the spreading is parabolic). Momentum diffuses from this turbulent mixing layer into the cavity zone which sets the wake fluid into motion, and thus the sharp velocity discontinuity at the wake boundary is smoothed out. In the reattachment zone the pressure increase arising out of the compression creates a steep pressure gradient near the surface such that part of the flow near the surface returns upstream to feed the recirculation zone. Due to this entrainment process the velocity and pressure variations are large, and the wake boundary is not well defined. For

theoretical analyses, however, this boundary, also called the dividing mean streamline, is chosen as the streamline, $\psi = 0$. This line separates the mixing layer, which comprises the original and part of the new shear layer, and the outer (undisturbed) flow from the recirculation region (Figure 2-3) where the fluid recirculates as a large eddy. The corner eddy is formed as a result of a shear-layer separation which is induced by the reverse flow now approaching the step as a forward-facing step. Alternately, for theoretical analyses the steady state shape of the recirculation bubble may be assumed to arise from the balance of the rate of entrainment from the bubble into the turbulent mixing layer along the bubble boundary and the rate of reversal of fluid back into the bubble [2].

Tani, et al. [8], used the model shown in Figure 2-4 for turbulent flow separation behind a back step, measuring surface pressure coefficients averaged over a set of measurements,

$$C_p = \frac{p-p_r}{1/2\ \rho u_r^2} ,$$

where p and p_r are the local and undisturbed static pressures, respectively. These are plotted versus the nondimensional distance, x/h, in Figure 2-5, where x is the horizontal distance downstream from the step of height h. Except for steps of very small heights, the base pressure

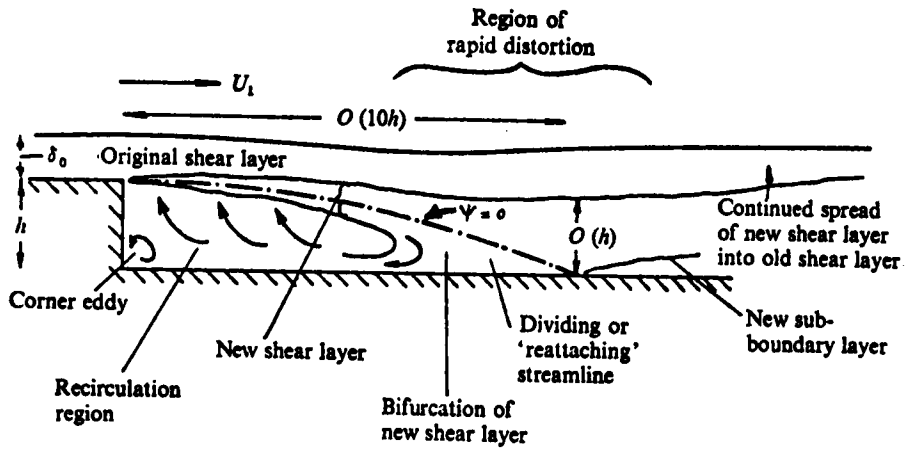


Figure 2-3. General behavior of typical reattaching flow [4].

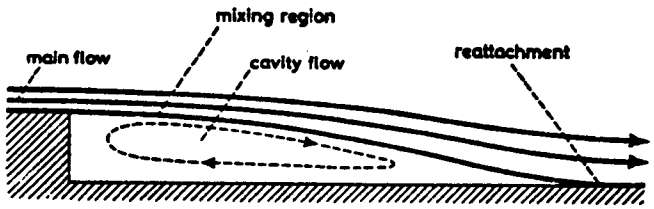


Figure 2-4. Separated flow model over a backward-facing step [8].

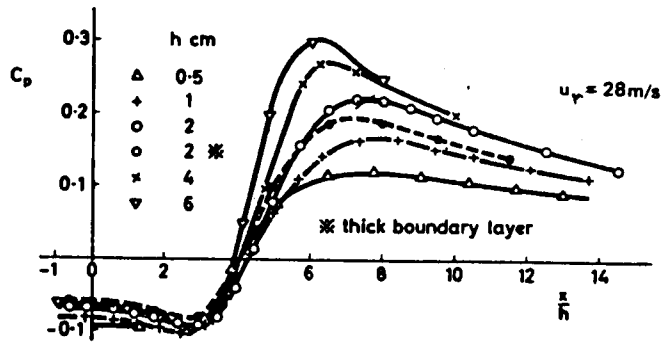


Figure 2-5. Pressure distribution on the step face and the bottom face [8].

was found to be insensitive to the step height and to the initial boundary layer thickness, the reason apparently being that the cavity flow is chiefly maintained by the turbulent shear stress, which is almost independent of the step height and the approaching boundary layer. It was seen (Figure 2-6) that turbulence and shear stress increase downstream in the mixing region and that the distribution across the mixing region of mean velocity, turbulence intensity, and shear stress is also insensitive to the step height and initial boundary layer thickness. The reattachment length was found to be equal to about seven step heights downstream of the step.

Experiments conducted by Bradshaw and Wong [4] show that for a wind tunnel speed of 25 meters per second, the recirculation zone is about six step heights long for a step height of 2.5 cms. It was found that after reattachment the turbulent shear layer splits up, part of which proceeds downstream with the eddy length scale considerably reduced, and the other part of which turns back upstream toward the recirculating region to supply the entrainment. Large eddies in the shear layer are virtually split in two if the fraction of the shear-layer mass flow that is deflected upstream at reattachment is appreciable, which is the case with a large initial boundary layer thickness and hence the atmospheric boundary layer. As a consequence, the turbulence structure is drastically different from that

h = 2 cm

u_r = 28 m/sec

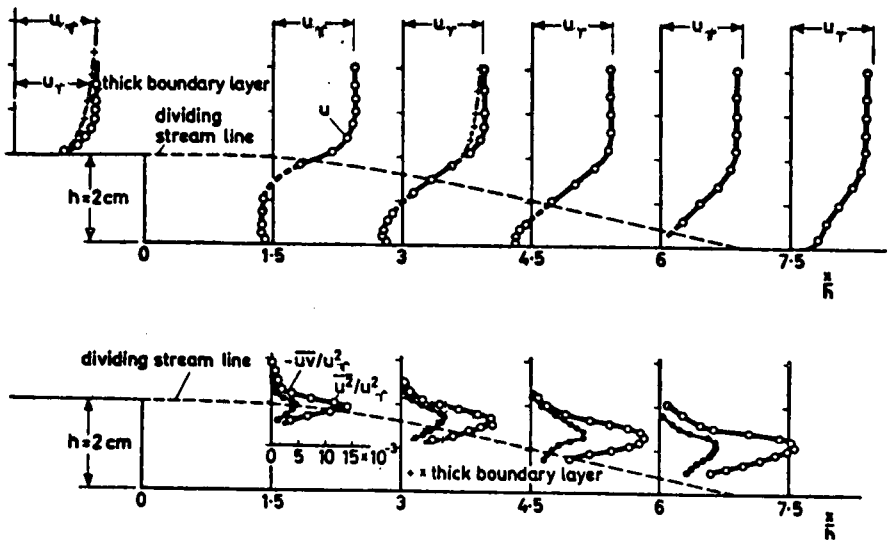


Figure 2-6. Distribution of streamwise mean velocity, turbulence intensity, and turbulent shear stress behind a backward-facing step [8].

found in any conventional shear flow. It had been argued earlier that large eddies are deflected alternately upstream and downstream rather than split as proposed by Bradshaw and Wong [4]. This would lead to a stronger unsteadiness in the wake than is normally found. At reattachment the thickness of the new shear layer is of the order of a step height (Figure 2-3, page 10). Curvature of the mean streamlines and a rapid distortion due to the pressure field near reattachment are the factors causing the initial shear layer to split roughly in half at reattachment (Figure 2-3).

As measured by Tani, et al. [8], and Mueller and Robertson [9], the shear stress in the free shear layer is much higher than the value of 0.01 ρU_1^2 (U_1 is the free stream velocity) found in a plane mixing layer. This is true even though the curvature of the streamlines associated with a free shear layer tends to decrease the shear stress and turbulence intensity. The reason for higher stress is that the effective velocity difference across the shear layer is more than U_1 due to the reversed flow in the separated region. Although the reverse flow velocity does not seem to exceed 0.2 U_1 , the shear stress exceeds $(1 + 0.2)^2$ times the plane shear layer value. Shear stress in the reversed flow region is not negligible [7, 10, 11], and it seems that the shear stress in the shear layer is increased by the "feedback" or the re-entrainment of

stress-bearing fluid from the separated-flow region. Such a mechanism needs further experimental investigation.

The mean velocity gradient, $\frac{\partial U}{\partial z}$, on a given streamline will be nearly the same before and after the region of rapid distortion at reattachment [4], that is to say, the mean vorticity is nearly conserved along a streamline; but despite this the decrease in Reynolds stress, $-\overline{u'v'}_{max}$, accounts for a sudden drop in the value of maximum shear stress near reattachment (Figure 2-7). Evidently large changes in turbulence structure occur when the shear layer bifurcates at reattachment.

As has been reported by many authors, for a thick initial boundary layer the maximum shear stress occurs near the dividing streamline throughout most of the separated shear layer except near reattachment where the Reynolds stress, $-\overline{u'v'}$, decreases rapidly to a value of zero. The turbulence intensity on the dividing streamline also decreases, but less rapidly. Although the measurements of shear stress near reattachment are not completely reliable [4], it is fairly well known that the surface shear stress rises rapidly after reattachment.

Flow Downstream of Reattachment

On the basis of experimental evidence, Bradshaw and Wong [4] define and classify the perturbation in the initially thin shear layer with the value of the parameter,

+ Arie and Rouse

□ Tani, et al., Muller and Robertson

△ $\delta_0/h = 0.5$

◭ $\delta_0/h = 0.33$

◇ Present results (measurement at x/h = 10, calculation thereafter)

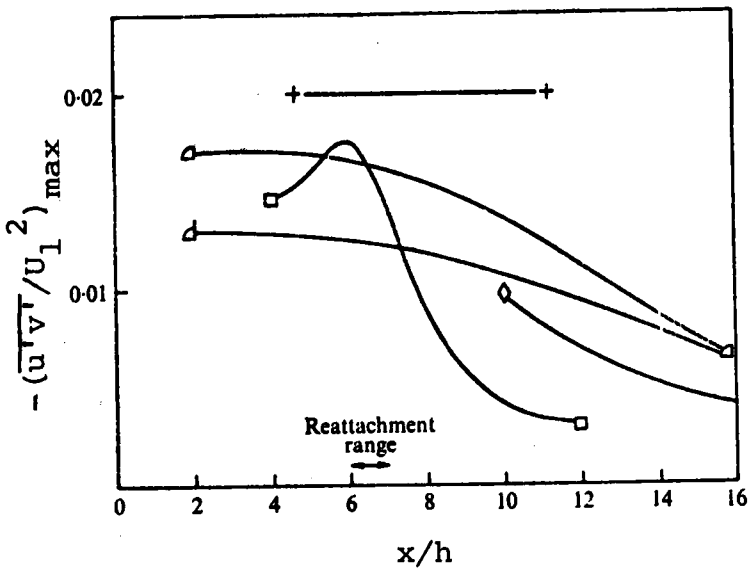


Figure 2-7. Maximum shear stress in shear layer [4].

h/δ_0 (step-height/boundary layer thickness measured at the separation point), as follows:

1. Weak perturbation : $h/\delta_0 << 1$.
2. Strong perturbation : $h/\delta_0 = O(1)$.
3. Overwhelming perturbation: $h/\delta_0 >> 1$.

(This parameter has also been found useful for classifying the flow downstream of reattachment.) An example of an overwhelming perturbation is the mutation of a boundary layer to a wake or a mixing layer. The flow of a thin boundary layer over a downstream-facing step involves two such perturbations, boundary layer to mixing layer and mixing layer back to boundary layer. The first perturbation can be ignored, and the flow can be treated as if a fully developed mixing layer appeared at the separation point. Since the atmospheric shear layer is generally large relative to any step height, that is, $h/\delta_0 << 1$, a building in atmosphere could be classified as a weak perturbation.

An equilibrium boundary layer is defined as one for which the turbulence structure is not strongly disturbed. The relaxation of the boundary layer after reattachment, a process where the disturbed boundary layer returns to its equilibrium state, has been found to be very slow [4, 12, 15]. It is generally assumed that the distribution of the average velocity can be described by universal laws applied to two layers in the turbulent boundary layer, the "Law of the Wall" and the "Law of the Wake." If this average

velocity distribution follows these universal laws, it will be assumed that the turbulent boundary layer is in an equilibrium state [12].

The "Law of the Wall" and the "Law of the Wake," for instance, as defined by Coles [13] are written as follows:

$$\frac{\bar{u}}{u_\tau} = \frac{1}{\kappa} \ell n \frac{z u_\tau}{\nu} + c + \frac{2\pi}{\kappa} \sin^2\left(\frac{\pi}{2} \frac{z}{\delta}\right) .$$

$\bar{u}$: average velocity with respect to z,

z : perpendicular distance from the wall,

u_τ: $\sqrt{\tau_w/\rho}$, shear stress velocity,

ν : kinematic viscosity,

π : a function of pressure,

κ : 0.4 (von Karman's constant).

Townsend [14] has an alternate approach to the definition of an equilibrium turbulent boundary layer. Townsend defines the state of equilibrium to exist between the production of Reynolds shear stress and the dissipation of turbulence energy which introduces gradient terms such as $\frac{\partial \bar{u}}{\partial z}$ and $\frac{\partial \tau}{\partial z}$ in the analysis. Obviously, the law of the wall and wake is a simpler approach.

The characteristic lengths that describe the average velocity in a turbulent boundary layer are ν/u_τ in the range of the Law of the Wall and δ in the range of the Law of the Wake. It is reasonable to assume that the

relaxation process could as well be characterized by any two lengths [13]. However, in the author's belief [12], additional parameters seem necessary to determine the process of relaxation completely. Once experimentally determined, they could be incorporated into the calculation procedures. However, these parameters are yet unknown.

The relaxation of the shear layer after reattachment to the ordinary boundary layer has been found to be very slow and non-monotonic [4]. Earlier reports suggested that the relaxation was monotonic [8, 10]. However, the results of [4] show that the surface shear stress does not return monotonically to the constant pressure equilibrium value and that it takes more than 50 step heights to return to its equilibrium value. These results correspond to an almost overwhelming perturbation, [$h/\delta_0 = O(10)$]. But even for just a strong perturbation, [$h/\delta_0 = O(1)$], Wauschkuhn and Ram [12] found that more than 20 step heights downstream were required to reach the equilibrium state. The results of Wu, et al. [15], from experiments to investigate different features of flow separation over a back step (a strong perturbation) also indicate that this relaxation distance is very large; and it was observed that static pressure takes a shorter distance to return to its equilibrium value than the velocity in the shear layer. These results indicate that the earlier belief which considered the mean velocity as

following the logarithmic law of the wall close to the surface in the relaxation region is wrong.

The recovery of the boundary layer after reattachment depends appreciably on the obstacle shape, even when the separation occurs from a sharp edge. In other words, obstacle shape affects the strength of the recirculation in the cavity zone. Relaxation behavior of the boundary layer after experiencing an adverse pressure gradient, for example, on a flat plate, which is monotonic in nature, is different from that of the boundary layer after reattachment, in the case of a step-flow, the primary reason being the rapid distortion of the flow in the reattachment region. The relaxing boundary layer in the case of a strong perturbation experiences more severe disturbance than in that of an overwhelming perturbation, although recovery from the former is quicker for a given initial boundary layer thickness, δ_0.

After reattachment, the turbulent length scales, especially the dissipation length parameter, L (for ordinary boundary layer, $L = \kappa z$), are almost independent of z except for a sudden drop to a value of zero at the surface [4]. This reduces the velocity gradient and hence the velocity in the inner layer below the value predicted by the logarithmic law,

$$\frac{\partial U}{\partial z} = \frac{(\tau_w/\rho)^{1/2}}{\kappa z} \quad ,$$

which demonstrates that the Law of the Wall is inapplicable under these conditions. Alternatively, the local-equilibrium form of the mixing-length formula [14],

$$\frac{\partial U}{\partial z} = \frac{(\tau/\rho)^{1/2}}{\kappa z} ,$$

gives even higher values of the velocity gradient. The failure of this formula can be traced to the fact that turbulence is not in local (energy) equilibrium, but changes rapidly in the streamwise direction, and that the length scale of turbulence is not proportional to z, but increases much more rapidly with z near the wall.

The outer layer, defined as one which retains the characteristics of the mixing layer, may take longer to return to the normal boundary layer state, since the outer-layer eddies, being larger, have longer lifetime than the inner-layer eddies. The effects of rapid distortion in the reattachment region propagate to the outer layer and change its mixing-length characteristics. Due to bifurcation of the mixing layer in the reattachment zone, the central region of the mixing layer comes into close contact with the surface; and hence there is a sudden jump in the value of apparent mixing length or true length scale of turbulence,

$$L = \frac{(-\overline{u'v'})^{3/2}}{\text{dissipation rate}} ,$$

above the local equilibrium value with increasing z.

Mueller and Robertson [10] conducted experiments on wedge-type roughness elements in air for the element-height Reynolds numbers such that the shear layer was turbulent downstream of the element. Turbulence was kept low by using mesh screens. The reattachment point was determined as the location where the shear stress value was zero, which was roughly seven element heights downstream. The mean velocity profiles behind the elements are shown in Figure 2-8. Boundary layer thickness is seen to increase slowly with distance downstream. Local skin friction coefficients, C_f , were obtained from the profiles near the wall from the Law of the Wall given below:

$$\frac{u}{u_r} = 5{\cdot}6\left(\frac{C_f}{2}\right)^{1/2}\left[1 + \log\left(\frac{zu_r}{\nu}\right) + \frac{1}{2}\log\left(\frac{C_f}{2}\right)\right] .$$

The results are shown in Figure 2-9. With the assumptions of a fully developed mixing region for the largest element, shear stress at the edge of the separation bubble, the dividing streamline, was calculated from the error function curve [16]. The calculated and the measured shear-stress profiles are compared in Figure 2-10. The width of this mixing region was found to increase linearly with distance from the roughness element.

The authors [10] classify the turbulence structure behind an obstacle into two stages. The first, one of excitation, from separation to the reattachment and the

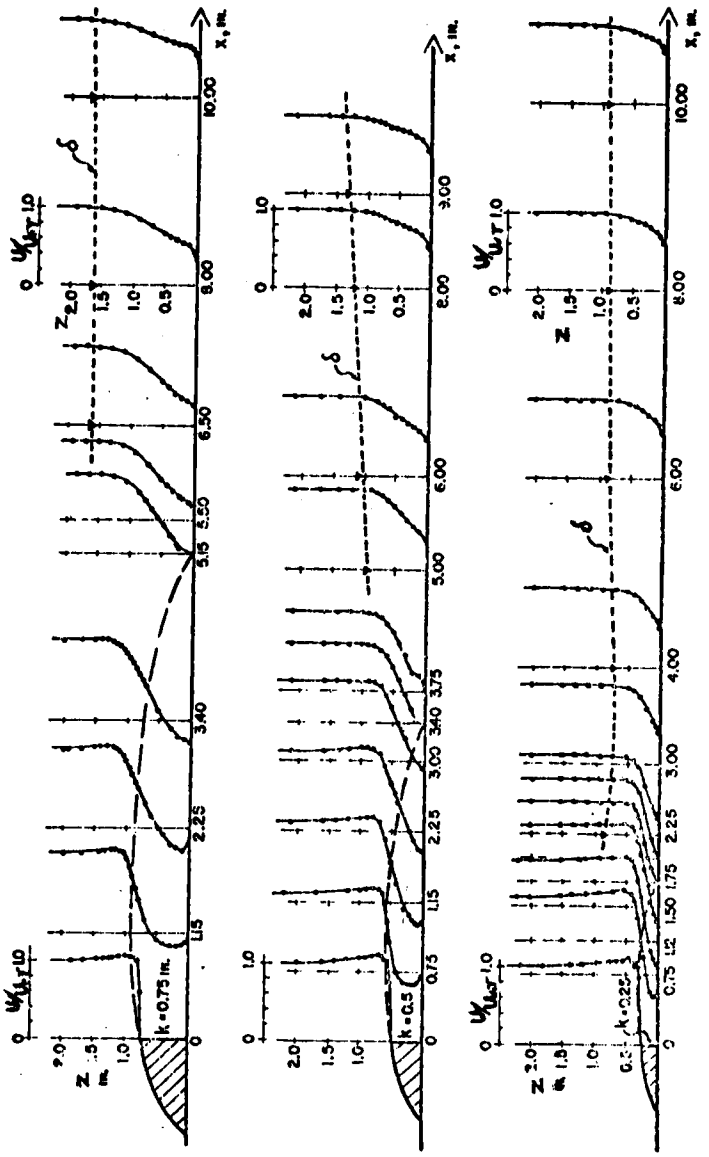


Figure 2-8. Velocity profiles in air flow past roughness elements [10].

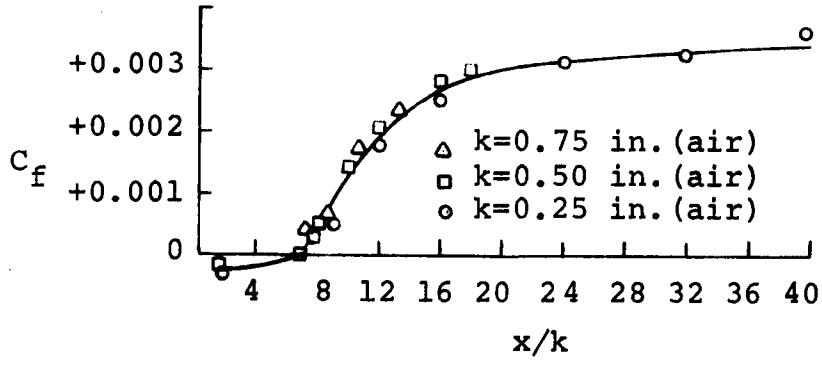


Figure 2-9. Downstream redevelopment of mean flow [10].

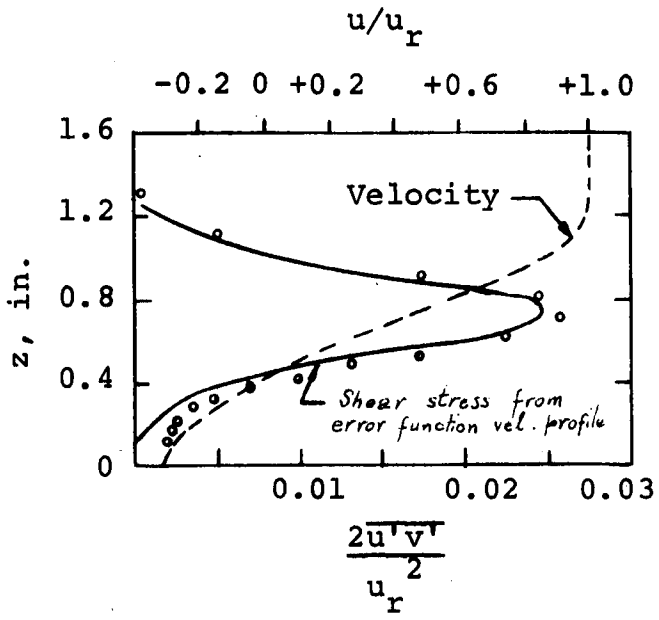


Figure 2-10. Turbulent shear-stress profile at x/k = 4.5 behind 0.75-inch element [10].

second, one of decay, after reattachment to the equilibrium state downstream. These two regions are clearly defined in Figure 2-11. From Figure 2-12 it can be seen that the shear stress has an initially high value in the excitation region. It decays downstream to the normal boundary layer value. For smaller elements there is a different maximum shear stress curve for the excitation region which indicates that the mixing layer did not reach the fully developed stage. Also, interference from the base could affect the shear stress curve for smaller elements. For the smallest element the boundary layer was seen to have achieved the equilibrium state 40 element heights downstream of the element (Figure 2-8). At this location the boundary layer was approximately three times the element heights thick. Also, the sequence of profile shapes downstream of reattachment is just the opposite to that found in the case of approaching separation in a boundary layer flow. These experimental results were obtained for a strong or overwhelming perturbation, ($\delta_0/h \leq 1$), and the initial boundary layer had no influence on the results.

Good and Joubert [5] experimentally obtained the static pressure variations across the separated region behind a bluff plate at various stations (Figure 2-13). An important feature of these profiles is that the locus of their minimums is approximately parallel to the ground and that it traces the region of high turbulence which initially

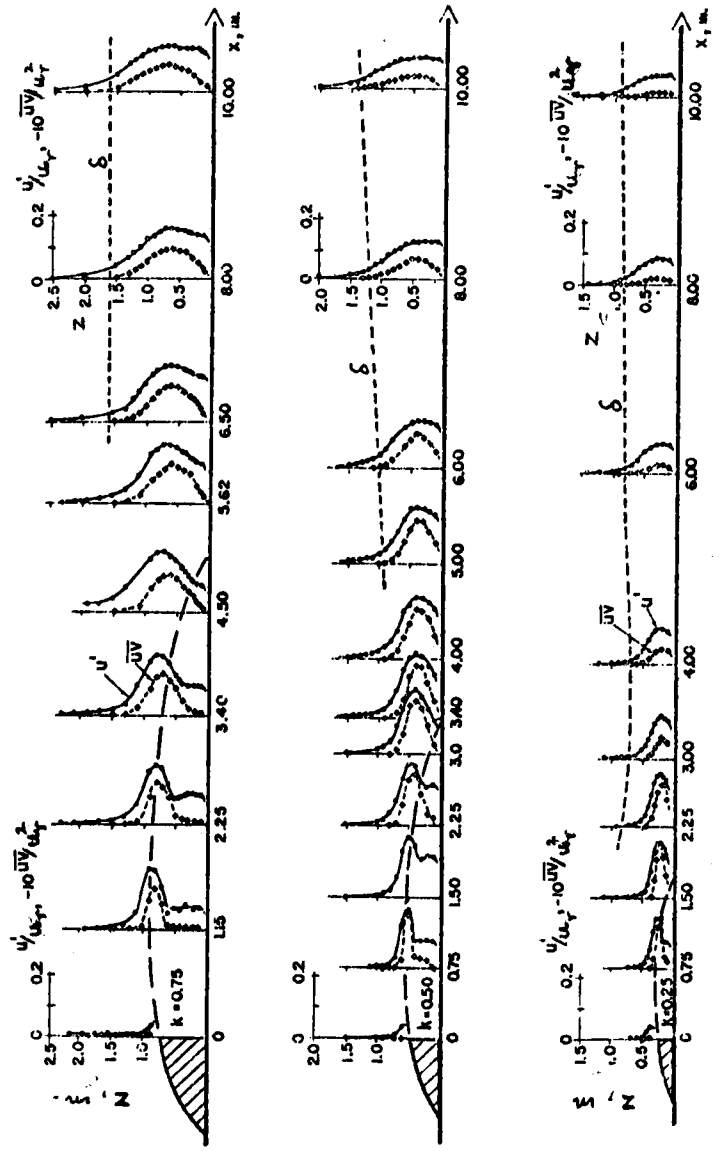


Figure 2-11. Turbulence profiles behind roughness elements [10].

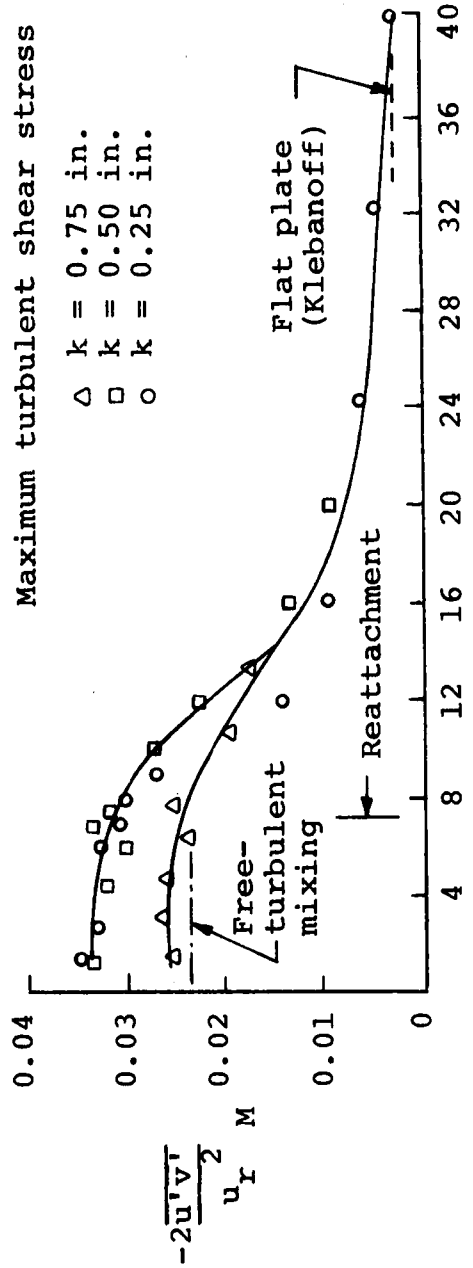


Figure 2-12. Downstream variation in turbulence quantities [10].

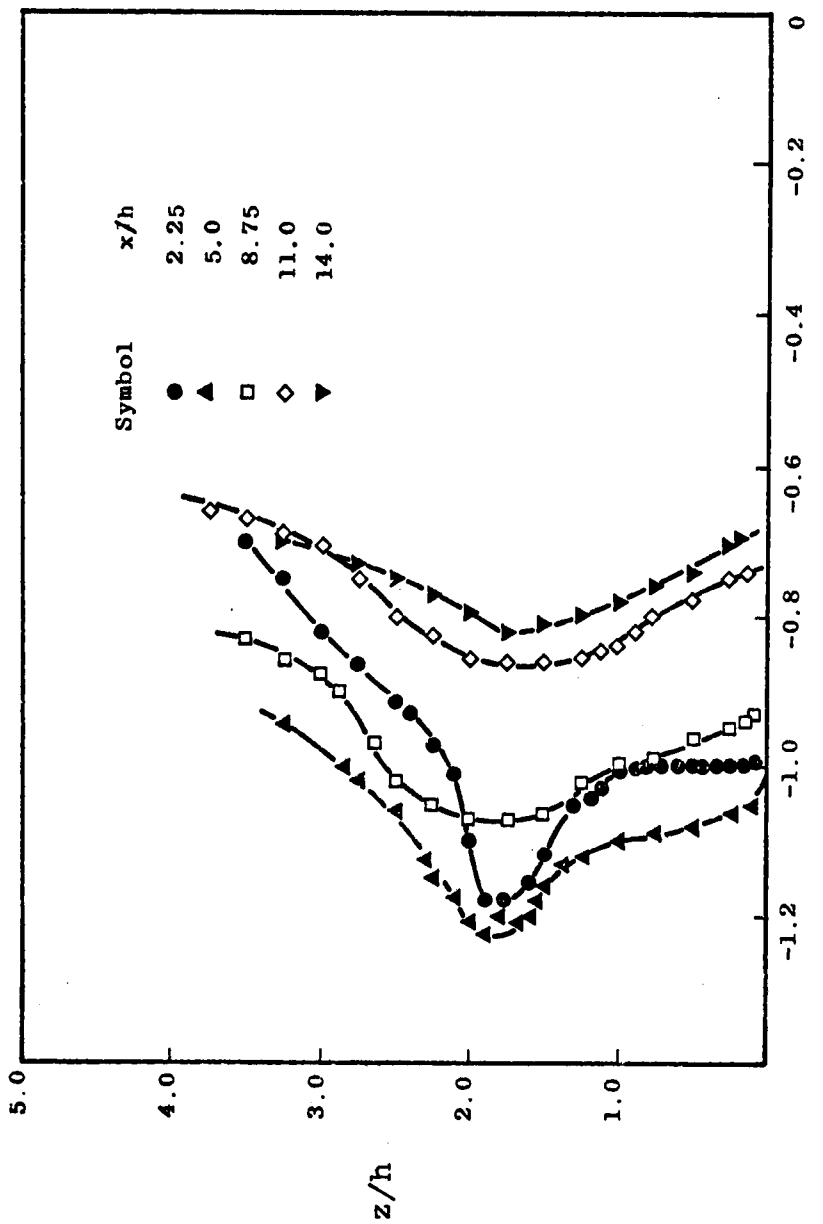


Figure 2-13. Static pressure measured through the wake behind a bluff plate [2].

coincides with the dividing mean streamline but continues to remain constant in height from the ground towards the end of the wake. The pressure losses associated with these minimums in the profile are believed to balance the large gradients in the transverse Reynolds stresses.

III. REVIEW OF ANALYTICAL MODELS

There is literature available regarding the determination of base pressure for two-dimensional steady (without vortex shedding) base flow. Tanner [17] has compared the theories of Chapman, Korst, Nash, and Kirk. The theory of Tanner has been discussed in comparison to these theories [17].

Most of these models assume very thin boundary layer at separation so that the assumption of similar velocity profiles is valid. In order to take the effects of boundary layer thickness into account, Kirk assumes that the shear or the mixing layer behaves as if it started some distance ahead of the base instead of starting at the separation point. It was seen that the base pressure calculated thus will be higher than that for vanishing boundary layer thickness. Also, neglecting the curvature of streamlines at separation (true for an "ideal" jet boundary), the pressure of the uniform stream ahead of separation and the pressure at the outer edge of the mixing zone are the same. In particular, in the calculation of base pressure Chapman

assumes that a balance exists between mass flow drawn from the base region by the mixing layer and mass flow reversed back into the base region by the pressure rise through the reattachment zone, and also that the compression through the reattachment zone is isentropic along the dividing streamline. Owing to the former assumption, for steady flow without bleeding into the wake region, the dividing streamline, as calculated from the mixing layer theory, must also be a dividing streamline at reattachment. Nash improved the reattachment criterion by taking into account the fact that the pressure at the reattachment point, p_r , is not equal to the final recovery pressure, p_1 , far downstream as had previously been assumed, but is actually less than p_1. Nash's reattachment parameter,

$$N = \frac{p_r - p_B}{p_1 - p_B} ,$$

where p_B is base pressure, was determined experimentally for a back step for Mach number equal to zero to be equal to 1.6, and not equal to unity.

The integral theory of Tanner predicts base pressure for subsonic flows and could be extended to apply in supersonic flow also. The main interest in Tanner's model as far as this investigation is concerned is not in how the base pressure is calculated, but in the way the wake region is modeled. Referring to Figures 2-14 and 2-15, a mixing process is assumed to occur in the region from the

(1) Outer boundary of mixing region

(2) Boundary of dead-air region

(3) Dividing streamline

(4) Particular streamline cutting boundary (1) at section I

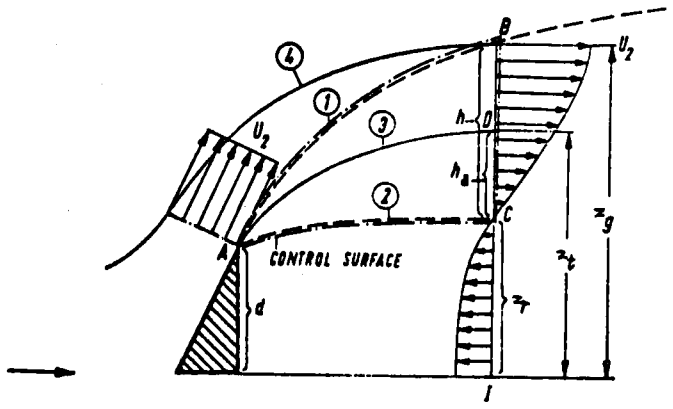


Figure 2-14. Flow model for derivation of the second outflow function [17].

R Reattachment point

I Section at which the outflow from the dead-air region ceases

(1) Outer boundary of mixing region

(2) Boundary of dead-air region

(3) Dividing streamline

(4) Particular streamline cutting boundary 1 at section I

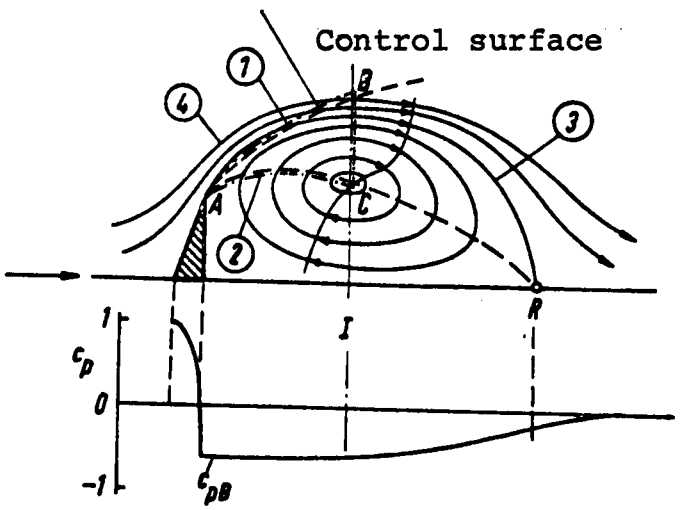


Figure 2-15. The subsonic steady base flow past a blunt body; mean streamlines and pressure distribution, schematically [17].

separation point A to the section I which corresponds to constant pressure mixing between a uniform external stream and fluid at rest. Due to this mixing, fluid is withdrawn from the dead-air region. This phenomenon will be called "outflow from the dead-air region." The dividing or reattachment streamline (3) separates the outer flow fluid from that withdrawn from the dead-air region. Experimental results [18] show that the velocity and hence the pressure at the boundary (1), which separates the external flow from the mixing region, tend to remain constant approximately up to a section midway between the separation and the reattachment points. At section I the mass flow between the boundary (2) through which the mass outflow from the dead-air region takes place and the dividing streamline (3) has its maximum value because then the backflow into the dead-air region begins. This maximum value is given by

$$m_a = \int_{z_r}^{z_t} \rho U dz \, . \tag{2.1}$$

Tanner relates m_a to the pressure drag and hence the base pressure and proposes the following expression for the velocity profile in the mixing region (Figure 2-16):

$$\frac{U}{U_2} = \frac{1}{2}\left[1 + \sin\left\{\frac{\pi(z-z_r)}{h} - \frac{\pi}{2}\right\}\right] ,$$

where U_2 is the outer-flow velocity. This profile is an

$$\frac{U}{U_2} = \frac{1}{2}\left[1 + \sin\left(\frac{\pi(z-z_r)}{h} - \frac{\pi}{2}\right)\right]$$

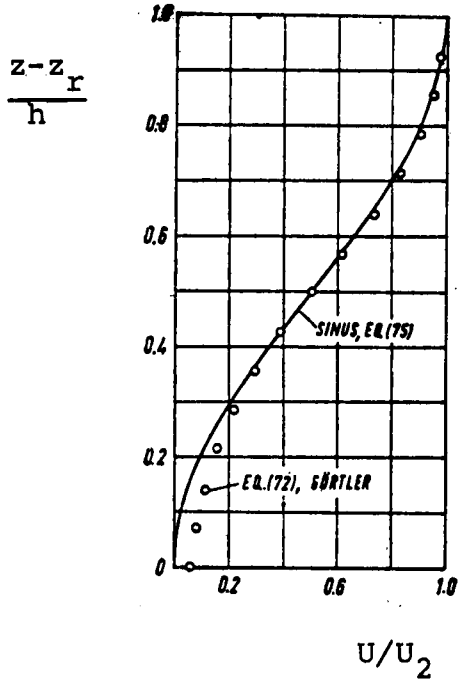


Figure 2-16. Velocity profile in the mixing region at the end of the outflow region [17].

approximation to the error function profile which is generally valid in a mixing layer.

Considering the static pressure throughout the control volume ABCA in Figure 2-15, page 32 (the flow approximates the flow in a free-jet boundary), as constant, the momentum equation reduces to

$$\int_{z_r}^{z_g} \rho U^2 dz - U_2 \int_{z_r}^{z_g} \rho U dz = 0 \text{ .} \qquad (2.2)$$

Making use of Equations (2.1), (2.2), and some empirical parameters such as h/d, Tanner calculates what is called the second outflow function. Considering the region between I and R, Tanner then calculates the first outflow function. The intersection of these two functions gives the base pressure coefficient. However, the parameter, h/d, which is closely related to the spread rate parameter, σ [19 through 25], as used in other theories, cannot be determined theoretically. As the spreading of the turbulent mixing zone is linear, σ will be constant at constant Mach number. Different values of σ have been used in the literature. For incompressible flow, σ as a function of the wedge angle, ϕ (for flat plate perpendicular to the air stream, $\phi = 180°$; for flow past a back step, $\phi = 0°$), is shown plotted in Figure 2-17 (experiments conducted by Tanner [17]). To account for compressibility, σ is given by the relation, $\sigma/\sigma_0 = 1 + 0.23\ M_2$, where σ_0 is the value of

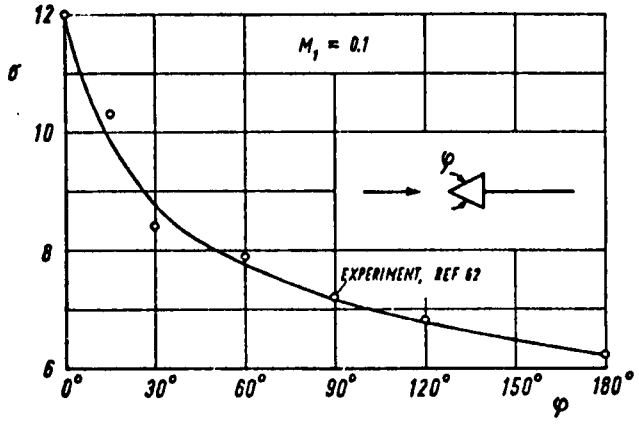


Figure 2-17. Influence of wedge angle on the similarity parameter of the mixing region for incompressible flow [17].

the spreading rate parameter corresponding to incompressible flow, and where M_2 is the Mach number at the outer edge of the mixing layer.

The two-dimensional problem of constant pressure mixing of laminar two-parallel streams has been considered by Yen [26]. The interface velocity and the location of the interface in the mixing region has been determined by considering the conservation of z-direction momentum through a control volume analysis. Due to mixing, there arises a transverse force acting on the dividing wall. For a free stream velocity ratio of 0.5 and 0, the interface deflects towards the higher and the lower velocity streams, respectively.

Kubota and Dewey [27] used a momentum integral technique to find the velocity profiles in the constant pressure laminar free shear layer. The shear layer was divided into two parts, one above and the other below the zero streamline; and separate polynomial and exponential expressions were used to describe the velocity profiles in these two regions. Closed form solutions of the momentum equations were obtained.

The constant pressure laminar mixing problem was solved assuming the boundary layer approximations to be valid for the free shear layers with finite initial thickness. The continuity, momentum, and energy equations were reduced to the incompressible form by using Howarth

transformation. By using suitable matching conditions the momentum equation is decoupled from the energy equation. In the transformed coordinate,

$$z = \int_0^{\bar{z}} (\rho/\rho_e)\, d\bar{z} \ ,$$

and the streamwise coordinate, s, the equations to be solved are of the incompressible form,

$$\frac{\partial u}{\partial s} + \frac{\partial v}{\partial z} = 0$$

$$u \frac{\partial u}{\partial s} + v \frac{\partial u}{\partial z} = \nu_e \frac{\partial^2 u}{\partial z^2} \ ,$$

where s and $\bar{z}$ are the distances measured along and normal to the dividing streamline, and ρ_e and ν_e are the values of density and kinematic viscosity in the undisturbed stream.

The velocity profile is represented by an analytic function containing several parameters as functions of s. The total number of boundary conditions applied at the extremities of the shear layer, at z = 0, and the moment equations obtained by multiplying the streamwise momentum equation by $u^j (j = 0,1,2,....)$ must equal the number of parameters appearing in the velocity profile. As the downstream velocity profile is quite different from the initial profile due to the non-similar growth of the free shear layers with a finite initial thickness, it is difficult to

represent the profile as a whole by a single expression. Hence the layer is divided into two regions, one above the zero streamline and the other below it. The profiles for these two regions are assumed to be of the form,

$$\frac{u}{u_e} = f = A_0 + e^{-\sigma\eta} \sum_{k=0}^{m} a_k \eta^k \ , \ \eta = \frac{z}{\delta_1}$$

and

$$\frac{u}{u_e} = g = B_0 + e^{\sigma h} \sum_{k=0}^{n} b_k h^k \ , \ h = \frac{z}{\delta_2} \ ,$$

respectively; δ_1 and δ_2 are the upper and lower shear layer thicknesses, respectively; m and n are so chosen that the profile is realistically approximated. The profile parameters, A_0 , a_k , B_0 , b_k , δ_1 , and δ_2 are determined by the boundary conditions at the lower and upper extremities of the shear layer, the continuity of the velocity and its derivatives at z = 0, and the moment equations. The possible boundary conditions for the outer and inner boundaries are, respectively,

$$\left.\begin{array}{ll} \sigma = 0 & \eta = 1 \\ \sigma = 1 & \eta \to \infty \end{array}\right\} \ f = 1 \ , \ f' = f'' = \cdots = 0$$

and

$$\left.\begin{array}{ll} \sigma = 0 & h = -1 \\ \sigma = 1 & h \to -\infty \end{array}\right\} \ g = 0 \ , \ g' = g'' = \cdots = 0 \ ,$$

where the primes denote derivatives of f and g with respect to η and h, respectively. The matching conditions at z = 0 are given by

$$\left(\frac{\partial^j f}{\partial \eta^j}\right)_{z=0} = \left(\frac{\delta_1}{\delta_2}\right)^j \left(\frac{\delta^j g}{\delta h^j}\right)_{z=0} \quad ; \; j = 0,1,2,\cdots .$$

For a quadratic profile, $\sigma = 0$ and $m = n = 2$; letting $j = (0,1)$, it was shown that $(u/u_e)_{z=0}$ was 0.596, which is very close to the exact value of 0.587 found by Chapman [28]. Using an exponential profile, ($\sigma = 1$), letting $m = n = 0$, and $j = (0,1)$, $(u/u_e)_{z=0}$ was found to be 0.618.

At the separation point, $s = 0$, $(u/u_e)_{z=0} = 0$, $\delta_2 = 0$, and δ_1 is equal to the initial shear layer thickness, δ_0. In the quadratic and the exponential profiles only one parameter, (z/δ_0), specifies the initial profile. If two or more such parameters were available, the effect of the initial profile on the rate of growth of $(u)_{z=0}$ would be known. Figure 2-18 shows the effect of the shear-layer profile on velocity along the zero streamline.

The Karman-Pohlhausen method for two-dimensional laminar flows does not give reasonable results in the region of adverse pressure gradient, and particularly when separation occurs. Between the separation and reattachment points this method fails to represent any real situation.

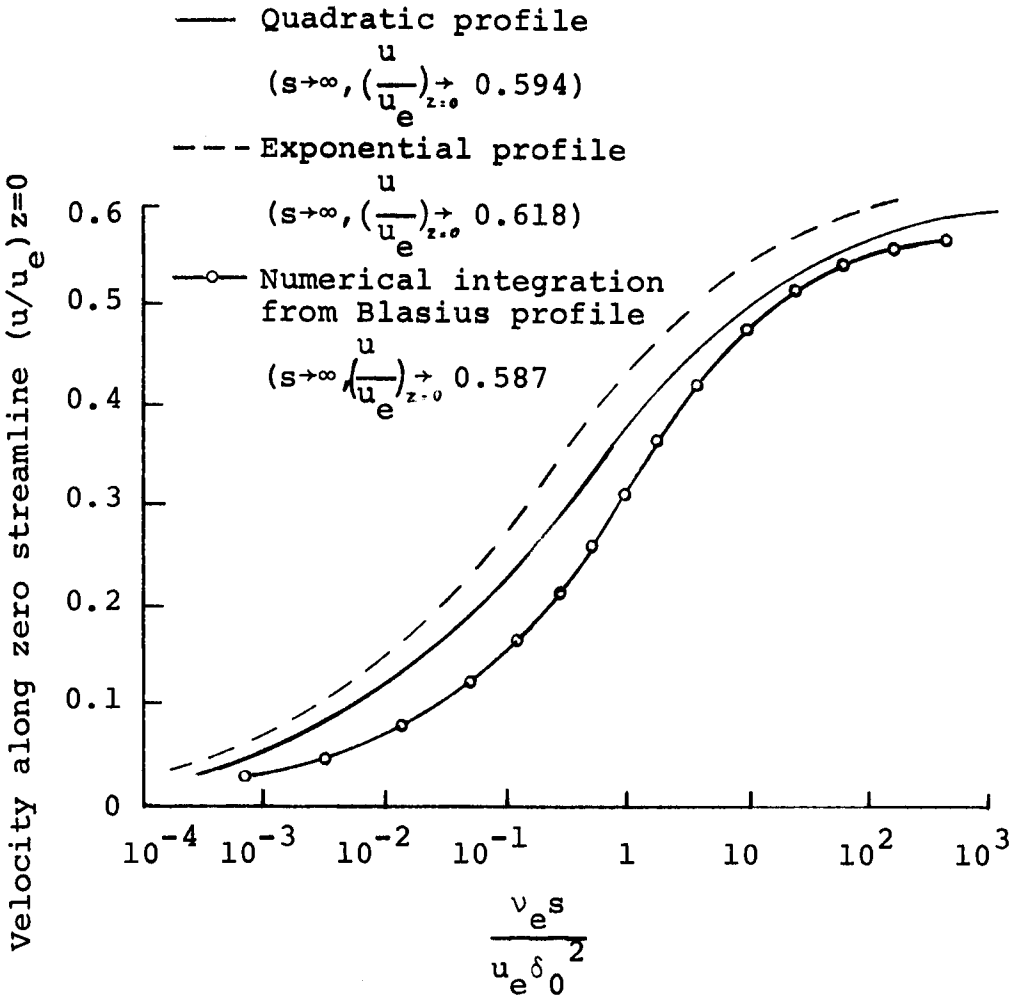


Figure 2-18. Effect of shear layer profile on velocity along zero streamline [27].

Where the pressure gradient is zero, the Karman-Pohlhausen method must yield an attached Blasius-type velocity profile. In Figure 2-19 reattachment will be predicted upstream of B, the region of zero pressure gradient, where in actual fact reattachment occurs downstream of B. An integral method first proposed by Walz [29] and modified by Tani [30] has been demonstrated by Lees and Reeves [31] to produce profiles with reverse flow even for zero pressure gradient and, therefore, could predict the behavior of separated flows. Also, this method does not require the empirical data which other methods require, for example, modified Crocco-Lees theory [32].

Modeling the flow separating from the sharp edge of a back step as a free-jet boundary between the outer flow with initial velocity, u_r , and a lower stream with a velocity of zero, and assuming zero initial boundary layer thickness, similar velocity profiles are given by the expression for the velocity profile in the region of a jet interaction [22] as

$$u = \frac{u_r}{2} (1 + \text{erf } \xi) ,$$

where the transverse coordinate,

$$\xi = \sigma \frac{z}{x} ,$$

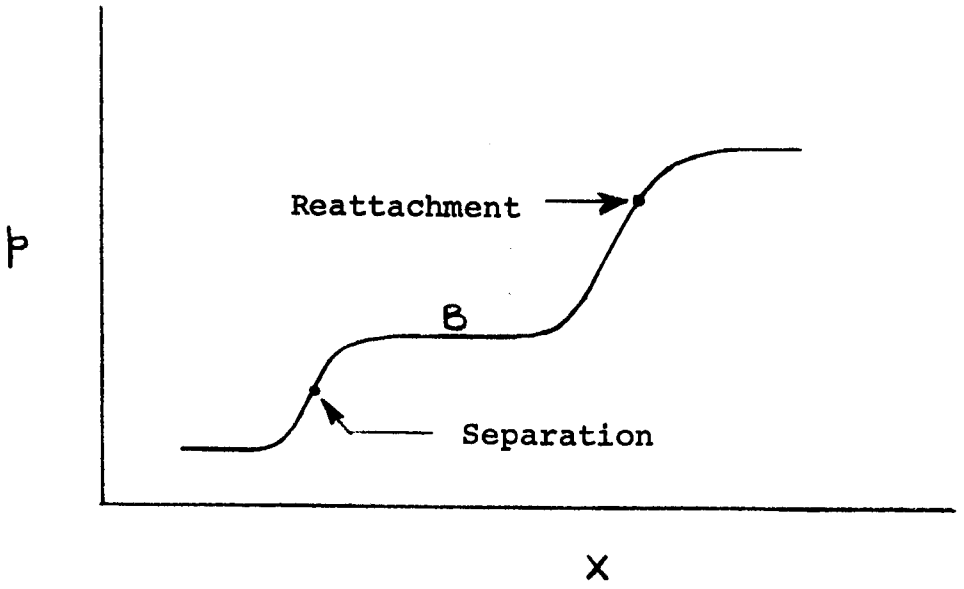


Figure 2-19. Typical static pressure variation on a flat plate in supersonic flow with separation induced by an incident shock wave.

and

$$\text{erf } \xi = \frac{2}{\sqrt{\pi}} \int_0^{\xi} e^{-t^2} \, dt \ .$$

The spreading parameter, σ, is an empirical constant. Various values of σ ranging from 9 to 15 have been used for back steps for incompressible flow. Plate [23] used $\sigma = 14.5$; and the x-axis was taken as the locus of points where $u/u_r = 0.5$, and the z-axis as perpendicular to x. Comparison of Plate's solutions with the experimental data (Figure 2-20) shows some disagreement at the negative value of ξ where the lower boundary begins to influence the data. This is attributed to the theoretical model which assumes that the lower velocity stream extends to minus infinity. The theory of free-jet boundary yields a Gaussian shear stress distribution, which is in good agreement with the experimentally measured shear stress distribution [33].

To make use of the error function profile, the curve given by $u/u_r = 0.5$ must be known either experimentally or theoretically. A theoretical prediction (work in progress by Bitte and Frost at The University of Tennessee Space Institute) can be made on the basis of free streamline theory, which is based on the velocity distribution in the undisturbed boundary layer, the shape of the obstacle, and some empirical input related to pressures on the obstacle and the reattachment length.

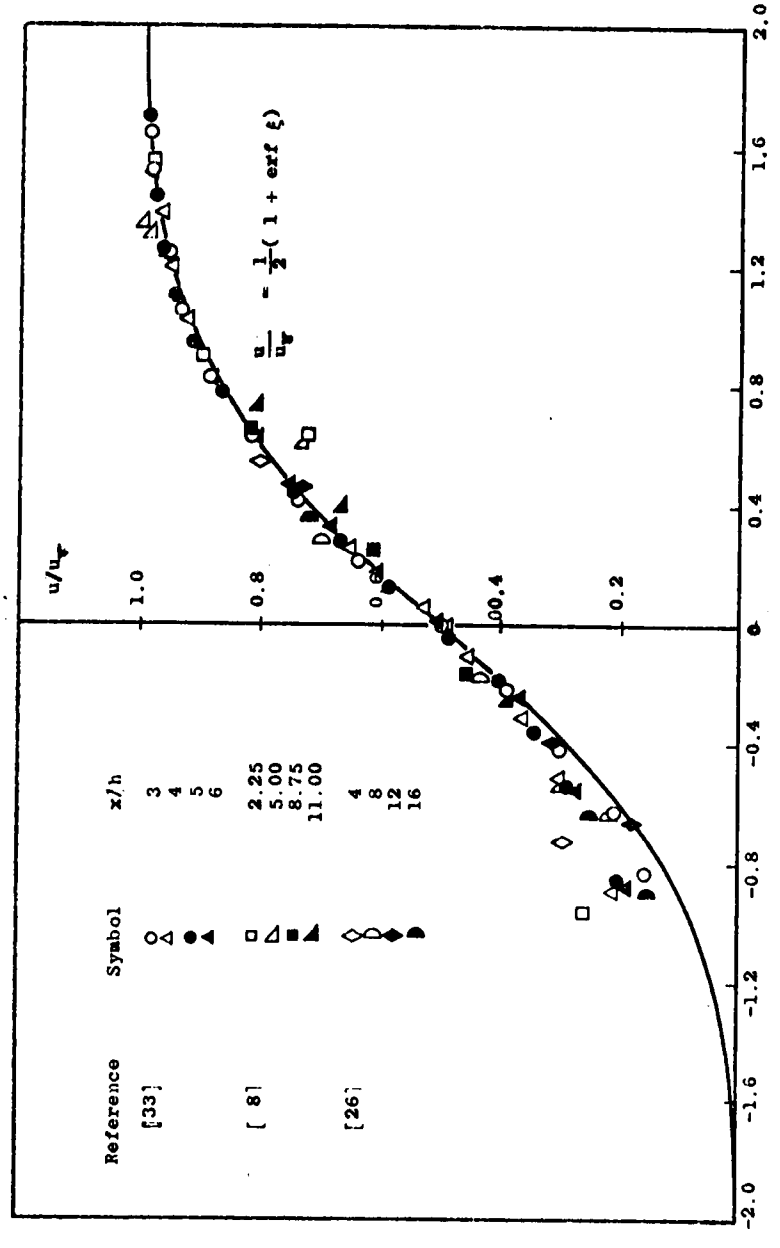


Figure 2-20. Correlation of velocity in the shear layer with error function profile [2].

Camarata [21] correlates the velocity profiles obtained from experimental data in the similarity region close to separation with the power law profiles,

$$\frac{u}{u_e} = \left(\frac{z}{\delta_0}\right)^{1/n} ,$$

with n varying from 6 to 9. The correlation parameter is

$$\frac{d\phi}{d\xi} \; (u/u_e = 0.5) ,$$

where

$$\phi = u/u_e$$

and

$$\xi = z/\delta_0 .$$

u_e: free stream velocity,

δ_0: initial boundary layer thickness.

With this correlation and the two-layer (outer and inner mixing zones) model for the velocity profile in the shear layer, an integral procedure [21] which does not need any specification of the shear stress distributions is readily applied to calculate the profiles.

The pre-asymptotic region of the free shear layer is divided into an upstream segment and a downstream segment

(Figure 2-21). The profile in the shear layer in the downstream segment is an error function profile,

$$u_{erf} = \frac{u_e}{2} (1 + \text{erf} \frac{\sigma z}{x}) .$$

In the upstream segment, the shear layer is partly a truncated error function profile for the inner mixing zone and partly a power law profile for the outer mixing zone, the free-stream edge of which does not appreciably change in height above the separation point at any x-location. The reason for this is that the initial boundary layer has a very slow growth relative to the rate of spreading of the mixing layer. Thus $\delta_0 \approx$ constant for all x stations. Since the whole initial boundary layer cannot be affected immediately by the abrupt removal of the wall, it is physically realistic to subdivide the shear layer as mentioned above.

Referring to Figures 2-22 and 2-23, an empirical correlation curve specifies the slope of the velocity profile in the pre-asymptotic region at the point, Δz, where $u/u_e = 0.5$. Therefore,

$$\frac{du}{dz} (u/u_e = 0.5) = \frac{1}{n} \frac{u_e}{\delta_0^{1/n}} (\Delta z)^{\frac{1-n}{n}} . \qquad (2.3)$$

The left-hand side of this equation is known; and for a given x, n is known. Hence Equation (2.3) will yield Δz.

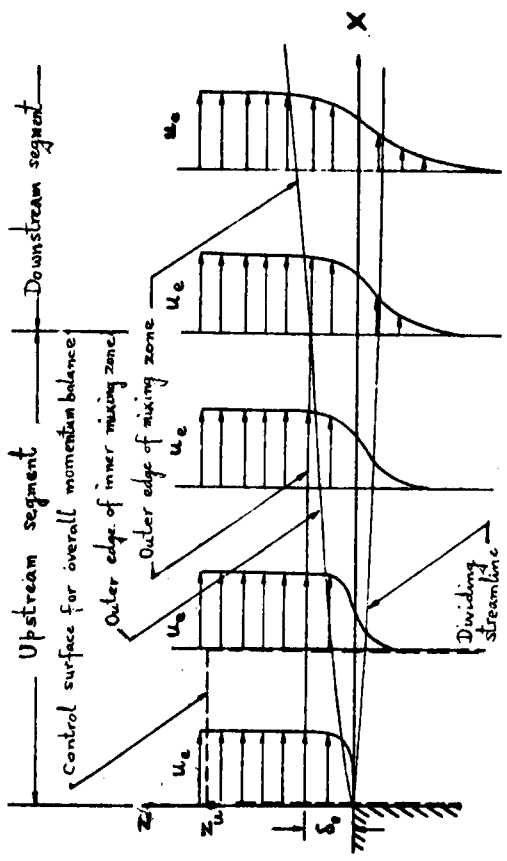


Figure 2-21. Flow model for pre-asymptotic region [21].

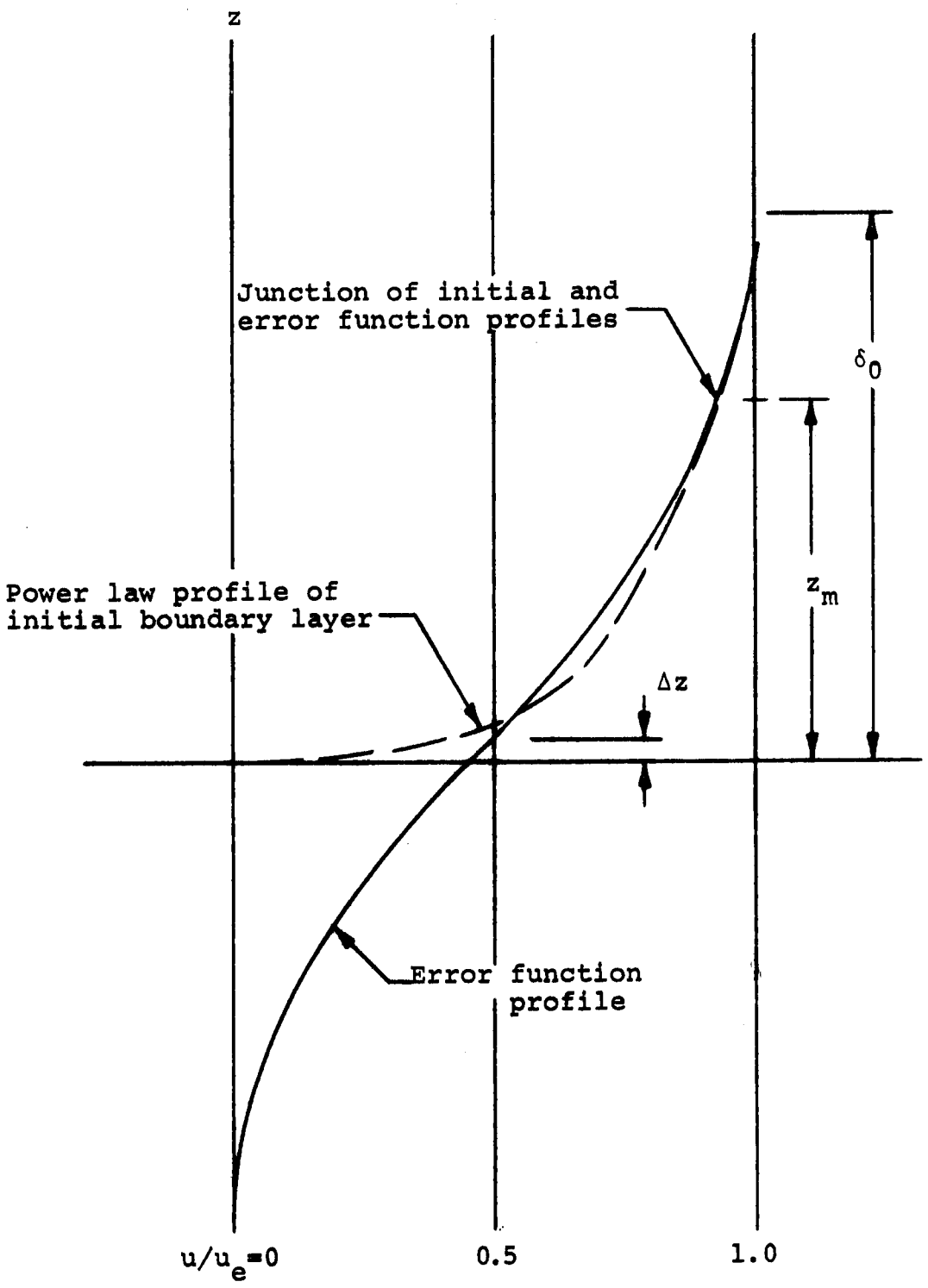


Figure 2-22. Pre-asymptotic velocity profile description [21].

Sym.	M_e	Investigator
○	~0	Charwat and Der [1]
□	~0	Chapman and Korst [2]
▽	~0	Kistler and Tan [3]
△	2.1	Hill [4]
◭	2.5	Hill [4]
▯	3.03	Sirieix and Solignac [5]
◔	3.99	Rhudy and Magnan [6]
◑	8.00	Rhudy and Magnan [6]

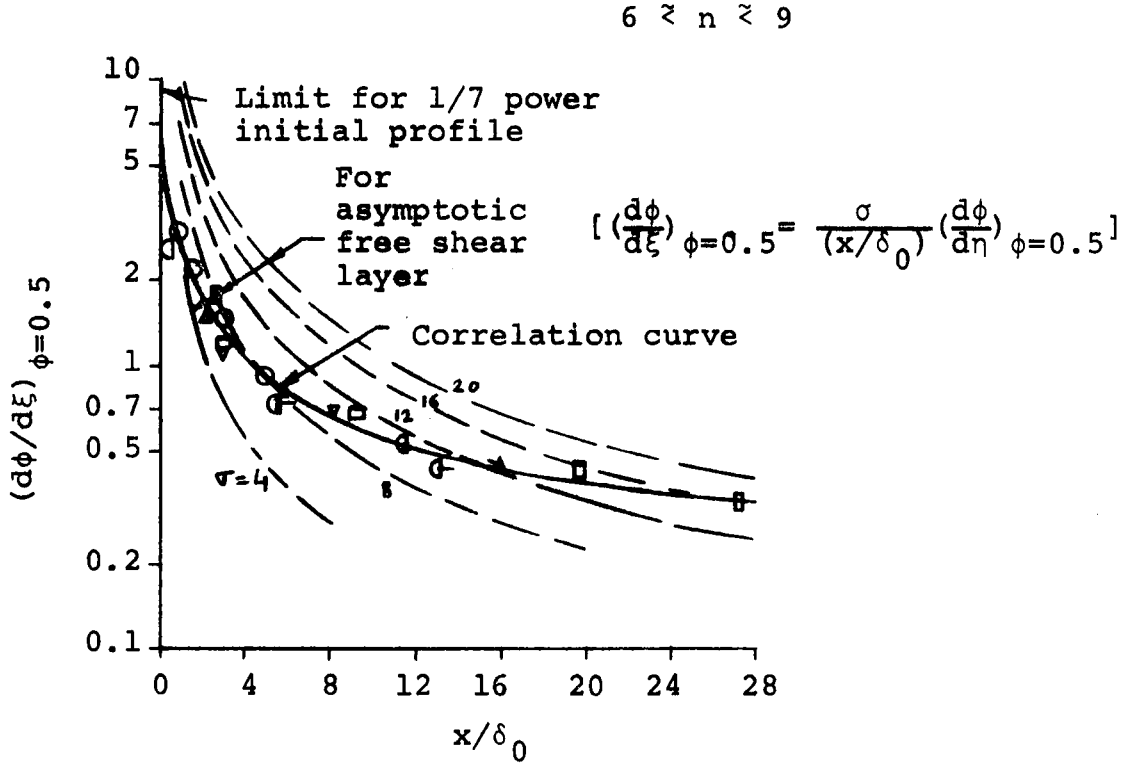


Figure 2-23. Variation of velocity profile slope at the half-free-stream velocity point with distance from separation [21].

Also,

$$\frac{du_{erf}}{dz}(\Delta z) = \frac{u_e}{\sqrt{\pi}} \frac{\sigma}{x} e^{-\left(\frac{\sigma \Delta z}{x}\right)^2} = \frac{du}{dz}(u/u_e = 0.5) \ . \quad (2.4)$$

For a given x, σ can be iteratively calculated from Equation (2.4). Therefore, the error function profile is known.

Conservation of momentum equation yields

$$\int_0^{z_m} u_e^2 (z/\delta_0)^{2/n_0} \, dz = \int_{-\infty}^{z_m} \frac{u_e^2}{4} \left(1 + \text{erf } \frac{\sigma z}{x}\right)^2 dz \ , \quad (2.5)$$

where n_0 (the value at separation) has been taken as 7 [21].

The preceding equation can be solved for z_m iteratively. Hence the velocity profile is completely known. Comparison of experimental data with the solutions is shown in Figure 2-24.

Far downstream from the asymptotic region, which is not a similarity region, no correlation is available; and hence σ has to be specified. From the theoretical estimates of earlier authors [21] σ in this region is approximated by the relations, $\sigma = 12 + 0.8 \, M_e$, M_e being the free-stream Mach number. Hence the transition between the asymptotic and the pre-asymptotic regions occurs at the point where the values of σ obtained from the two criteria are equal.

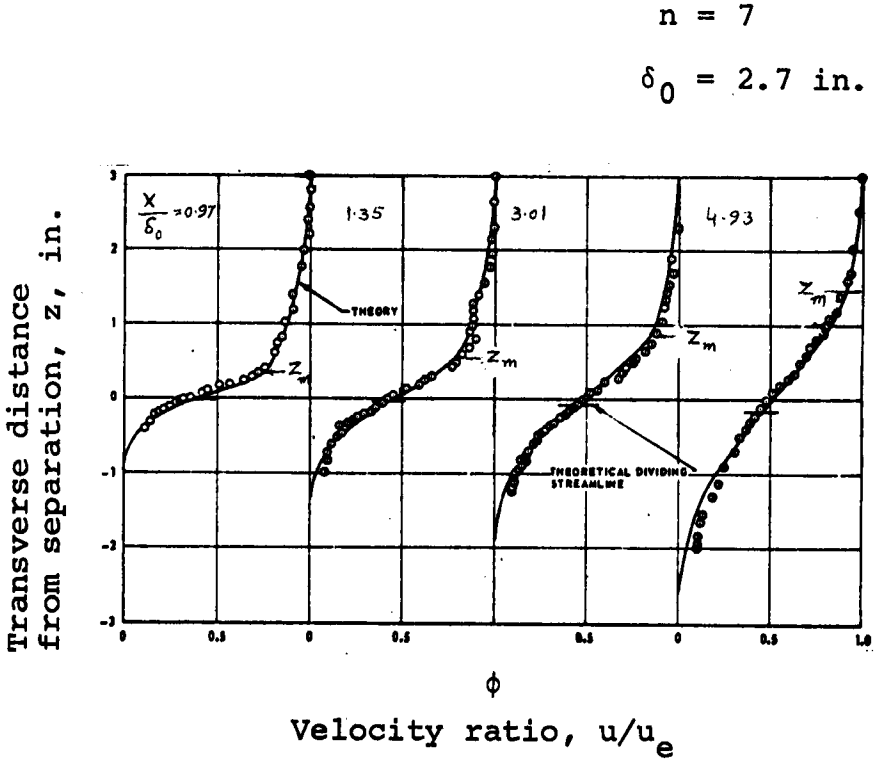


Figure 2-24. Comparison of theory with incompressible measurements of Charwat and Der [21].

Korst and Chow [19] have compared various analytical and experimental constant-pressure free shear layer similarity profiles by the use of spread rate parameters. It was found that in addition to the flow conditions, σ also depends on the analytical model, the way matching is done with the experimental data, and the viscosity model of turbulence employed. Although matching along the dividing streamline could be done, matching at the half-free-stream-velocity point, $u/u_e = 0.5$, was observed to be more realistic, as shown by Figures 2-25 and 2-26. Various profiles agree very closely at this point.

The initial conditions like the initial boundary layer thickness, the initial velocity profile, and the initial distribution of turbulence intensity influence the flow downstream in the free shear layer. As long as the change in the pressure gradient is small, the turbulent flow equations can be laminarized to some accuracy through the use of an eddy transport coefficient concept. Turbulence shear stress, in analogy to laminar shear stress, is written as

$$\tau = \rho\varepsilon \frac{\partial u}{\partial z} ,$$

where ε is the eddy viscosity. Various eddy viscosity models have been examined [20]. These viscosity models as applicable to incompressible flow are as follows:

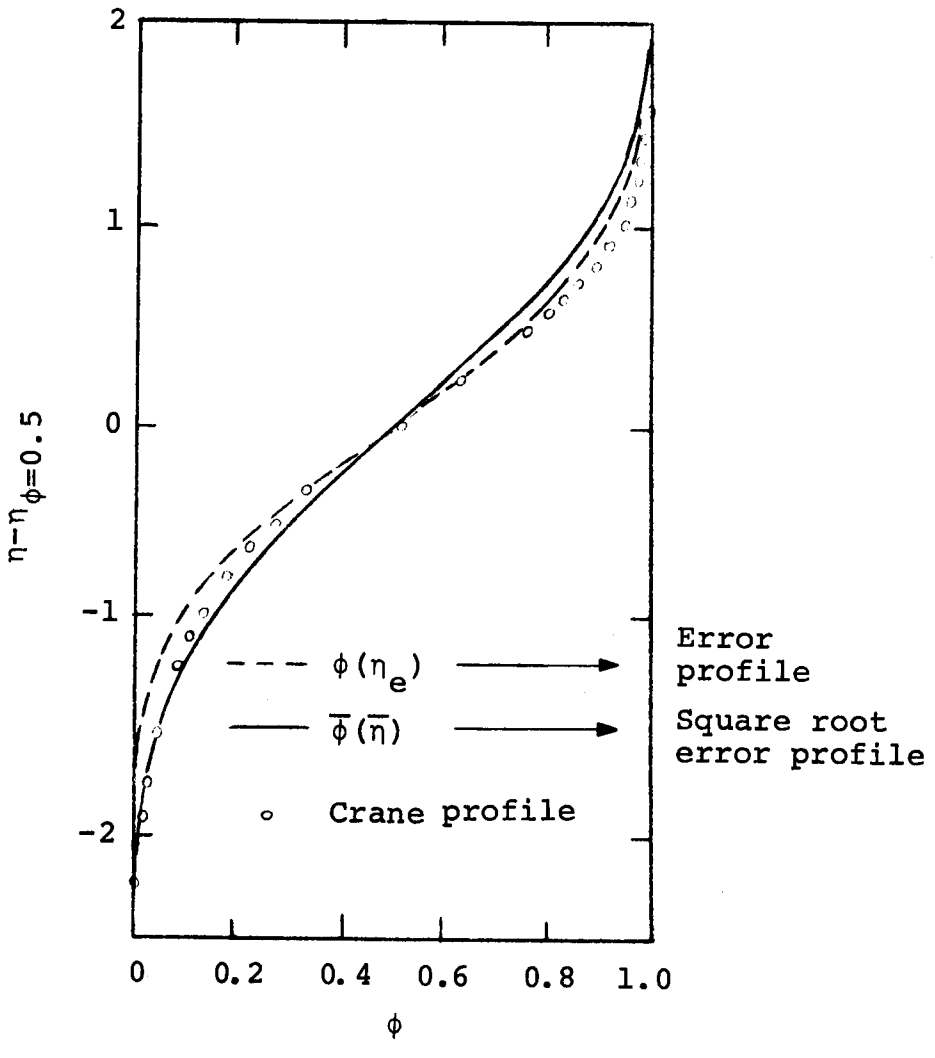


Figure 2-25. Comparison of different velocity profiles [19].

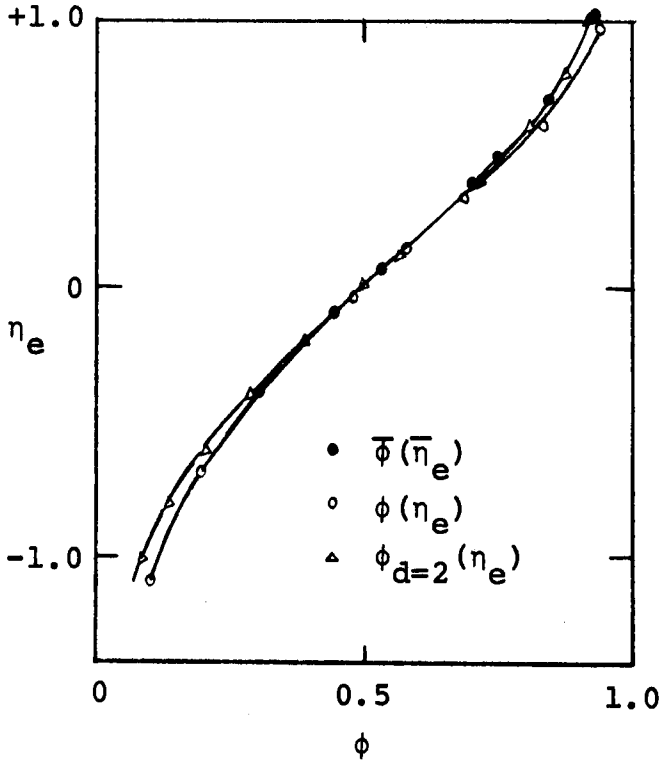


Figure 2-26. Illustration of the matching of various profiles with the common scale as the transverse coordinate of the error function profile [19].

$$\varepsilon = k_1 \theta u \ , \tag{2.6}$$

$$\varepsilon = k_2 (x + x_0) u_e \ , \tag{2.7}$$

$$\varepsilon = k_3 \ u_e^2 / (\frac{\partial u}{\partial z})_D \ , \tag{2.8}$$

$$\varepsilon = k_4 (x + x_0)^2 \ \left| \frac{\partial u}{\partial z} \right| \ , \tag{2.9}$$

where k_1 , k_2 , k_3 , and k_4 are empirical constants. The constant x_0 is the shift of the virtual origin due to the presence of an initial boundary layer. It accounts for the initial thickness. Subscript D refers to the dividing streamline, and e indicates the outer edge of the mixing layer (Figure 2-27).

In Equation (2.9) Prandtl's mixing length, expressed by $\sqrt{k_4}(x + x_0)$, is assumed proportional to the streamwise distance, x. Equations (2.6) and (2.7) are similar to Prandtl's simplified hypothesis [22] in which ε is assumed proportional to the width of the mixing layer. Nash [24] used Equation (2.8) in his study of the pre-asymptotic shear layer.

At the separation point a singularity exists, and there is a small neighborhood where a discontinuity in shear stress occurs. This neighborhood for flat plate has been found to be $O(LR^{-3/4})$, where L is the length of the plate and R is the Reynolds number based on L. Neglecting this extremely small region, laminarized boundary layer equations

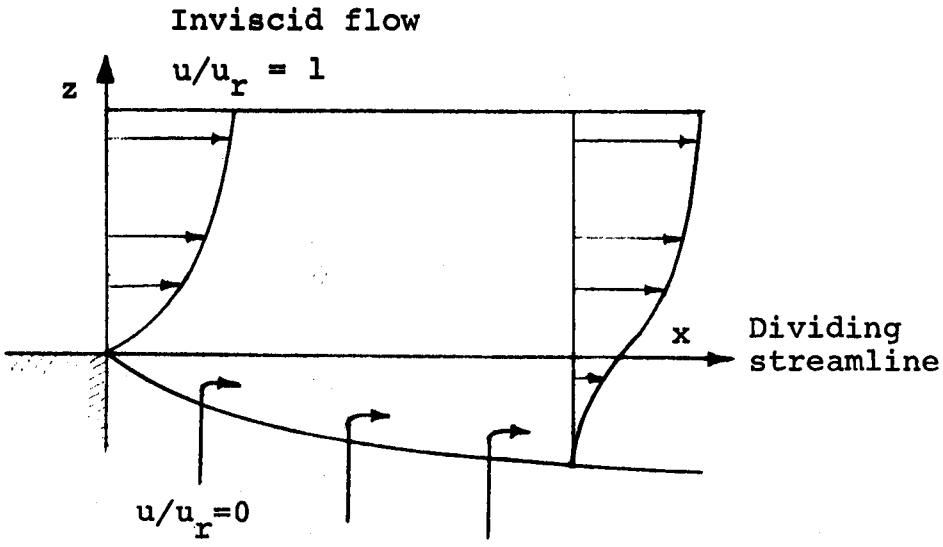


Figure 2-27. Free shear layer model [20].

describe sufficiently accurately the similar and nonsimilar flow regions in a free shear layer. The effect of the sharp turn of the attached boundary layer flow on the initial velocity profile is neglected. Therefore, the attached boundary layer profiles are the initial conditions for the separated shear layer.

Values of the empirical constants evaluated after comparing the experimental data with the calculated velocity profiles [20] were found to be as follows: $k_1 = 0.6$; $k_2 = 0.002$; $k_3 = 0.015$; $k_4 = 0.0575$; $x_0 = 30\ \theta_0$, where θ_0 is the momentum thickness at the shifted origin. The similarity parameter, σ, was taken as 9.42.

The model as described in Equation (2.9) does not give results in agreement with the other three. This is because it yields a different viscosity distribution. Viscosity increases from zero to a maximum inside the shear layer and then decreases to a value of zero at the upper edge of the mixing layer. But in the other three models the viscosity is constant across the layer. For the sake of simplicity these three models are well suited for calculating the mean quantities in turbulent free shear layers. However, although the empirically determined values of the k's give good correlation in one region, they may fail in other regions of the same flow field. Hence they are not universal constants for the whole flow region.

In the case of mixing in a free-jet boundary, streamlines have a curvature which becomes important and should be taken into account. Uchida and Watanabe [34] defined streamline coordinates in a curved flow field by α and β and their extension parameters by $h_\alpha = \frac{\partial s}{\partial \alpha}$ and $h_\beta = \frac{\partial n}{\partial \beta}$, where s and n represent arc lengths along and normal to the streamline, respectively (Figure 2-28).

h_α and h_β satisfy Gauss' orthogonality equation,

$$\frac{\partial}{\partial \alpha}\left(\frac{1}{h_\alpha}\frac{\partial h_\beta}{\partial \alpha}\right) + \frac{\partial}{\partial \beta}\left(\frac{1}{h_\beta}\frac{\partial h_\alpha}{\partial \beta}\right) = 0 ,$$

with β = constant chosen as streamlines;

$$u = \frac{1}{h_\beta}\frac{\partial \psi}{\partial \beta} = \frac{1}{h_\beta} ,$$

$$v = \frac{1}{h_\alpha}\frac{\partial \psi}{\partial \alpha} = 0 ,$$

$$R = \frac{u_s \ell_s}{\nu} .$$

The concentration of the mass flow in the mixing zone expressed by β is lower than that expressed by ψ in the Cartesian coordinates, and hence

$$\frac{\partial u}{\partial \beta} > \frac{\partial u}{\partial z} .$$

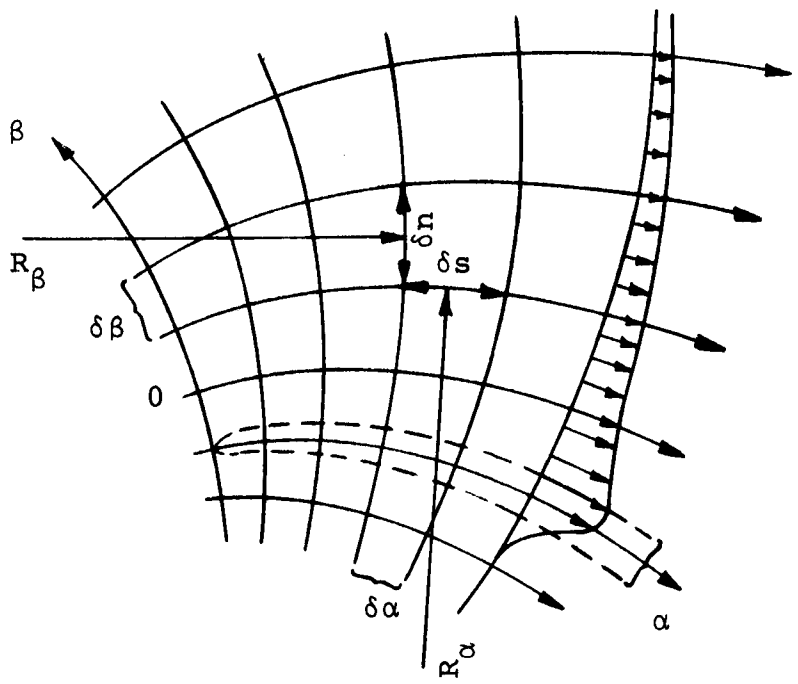


Figure 2-28. Streamline coordinates system [34].

Applying boundary layer approximations to the Navier-Stokes equations in the streamline coordinates, two important facts become apparent [34]. Firstly, the nondimensional pressure gradient, $\frac{\partial p}{\partial \beta}$, counterbalances the centrifugal force; and secondly, the effect of curvature becomes important when it is of the order of $R^{1/2}$. In making the boundary layer approximations, orders of magnitude for various quantities are assumed to be

$$O(\beta) = R^{-1/2}$$

$$O(h_\alpha \ , \ h_\beta \ , \ u \ , \ p \ , \ \alpha) = 1 \ .$$

At $\beta \to \infty$, the solution is matched with the outer flow of velocity, u_e. Defining the variable [35],

$$\lambda = \frac{h_\alpha}{h_\beta} = u_e \left(\frac{1}{h_\alpha}\right) \ ,$$

$1/h_\alpha$ becomes equal to u_e on the outer boundary where $\lambda = 1$. Thus the boundary conditions can be expressed as

$$\text{at } \beta \to +\infty \ ; \ \lambda = 1 \text{ and } \frac{\partial \lambda}{\partial \beta} = 0 \ ,$$

$$\text{at } \beta \to -\infty \ ; \ \lambda = 0 \ .$$

In deriving similar solutions, a similarity variable is defined as

$$\eta = \sqrt{R/\alpha\beta} \ ,$$

which takes into account the fact that the width of the laminar mixing zone increases as $\alpha^{1/2}$ corresponding to $x^{1/2}$ in the usual case.

Assuming no pressure gradient along the zero streamline for incompressible laminar mixing in free-jet boundary, the authors theoretically generate shear stress along $\psi = 0$ as a function of the curvature parameter, C, along $\psi = 0$ (Figure 2-29), where

$$C = \left(\frac{\alpha}{R}\right)^{1/2} \frac{1}{h_\alpha h_\beta} \frac{\partial h_\alpha}{\partial \beta} H \ ;$$

H is a function of integration.

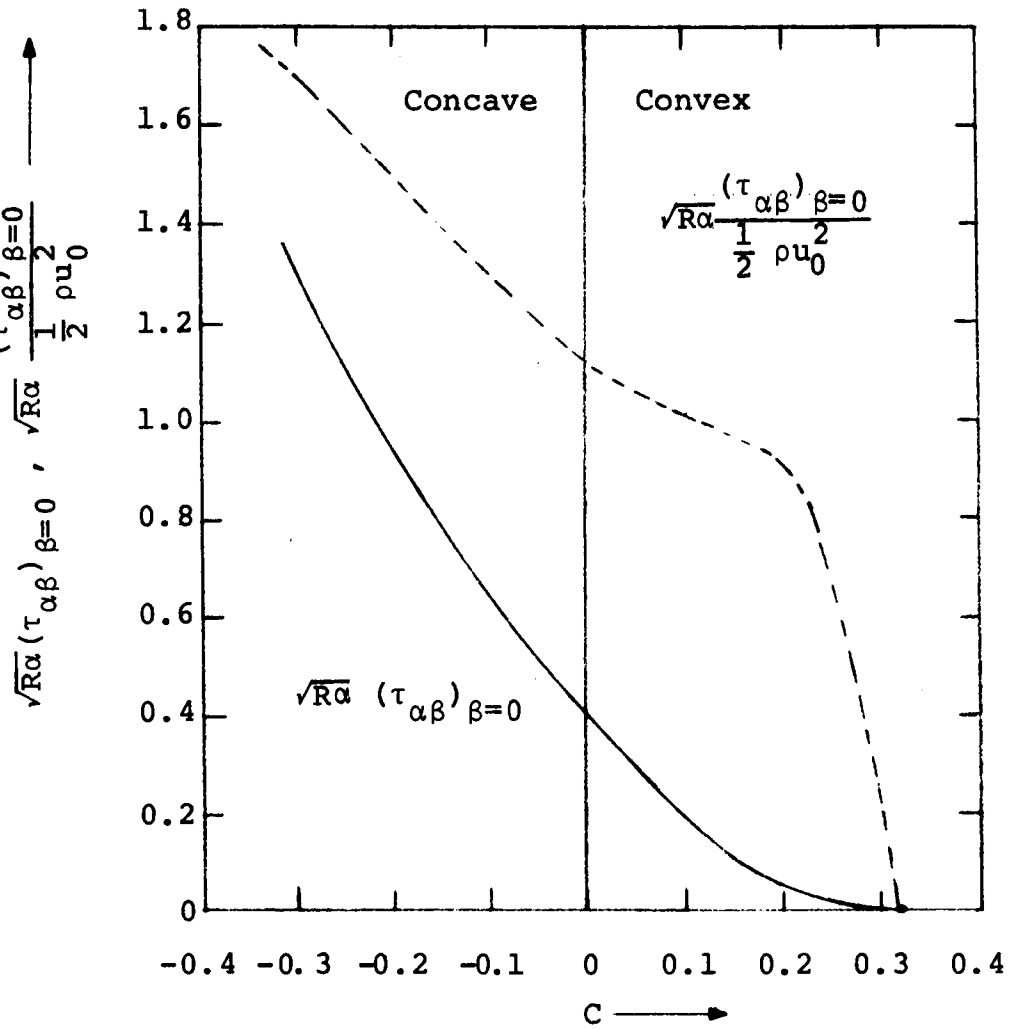


Figure 2-29. Shearing stress along zero streamline [34].

CHAPTER III

SOLUTION OF GENERAL NAVIER-STOKES EQUATIONS AS APPLICABLE TO ATMOSPHERIC FLOW

Governing Equations for the Turbulent Atmospheric Flow

Equations of motion for a steady, two-dimensional, incompressible Newtonian flow in the Cartesian coordinates, x and z (Figure 3-1), are

$$\frac{\partial u}{\partial x} + \frac{\partial v}{\partial z} = 0 \ , \tag{3.1}$$

$$u\frac{\partial u}{\partial x} + v\frac{\partial u}{\partial z} = -\frac{1}{\rho}\frac{\partial p}{\partial x} + \frac{1}{\rho}\frac{\partial}{\partial x}[\mu_{eff}(2\frac{\partial u}{\partial x})] + \frac{\partial}{\partial z}[\mu_{eff}(\frac{\partial u}{\partial z} + \frac{\partial v}{\partial x})] \ , \tag{3.2}$$

$$u\frac{\partial v}{\partial x} + v\frac{\partial v}{\partial z} = -\frac{1}{\rho}\frac{\partial p}{\partial z} + \frac{1}{\rho}\frac{\partial}{\partial z}[\mu_{eff}(2\frac{\partial v}{\partial z})] + \frac{\partial}{\partial x}[\mu_{eff}(\frac{\partial u}{\partial z} + \frac{\partial v}{\partial x})] \ , \tag{3.3}$$

where u and v are the ensemble averaged components of velocity along the x and z directions.

In this study these equations are assumed to govern the neutral atmospheric boundary layer flow. The Coriolis forces induced by the rotation of the earth [36]

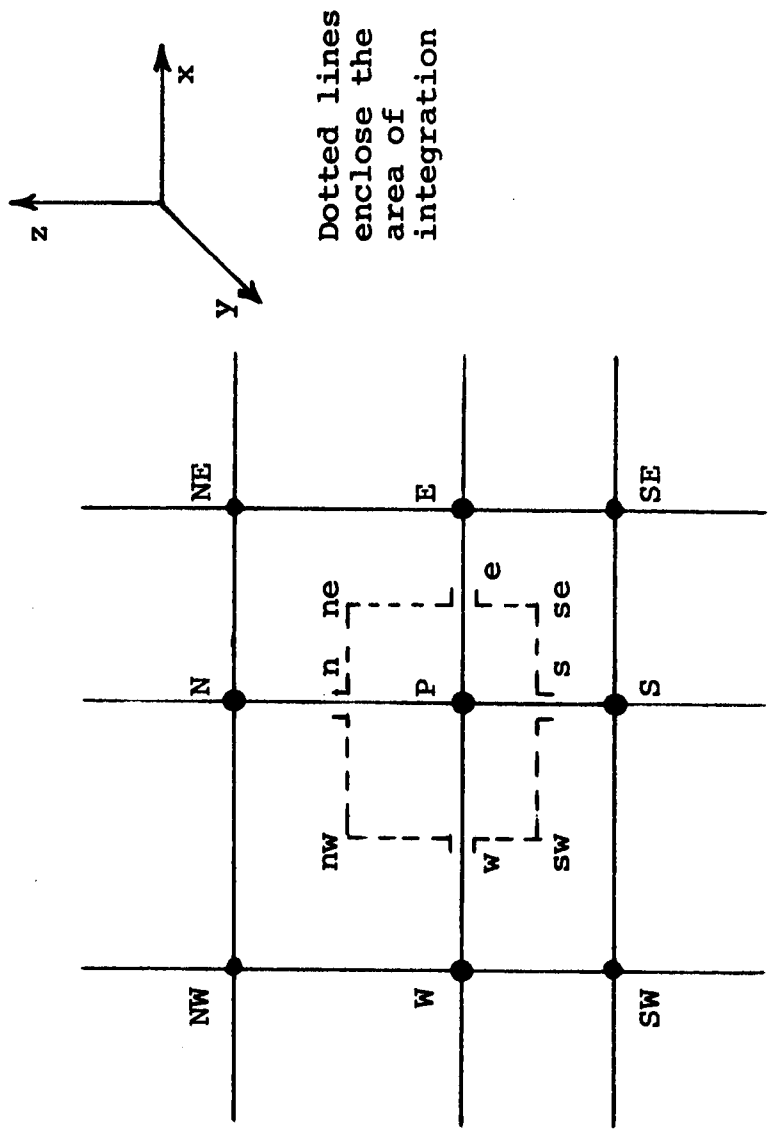


Figure 3-1. Portion of the finite-difference grid.

are considered negligible in the lower regions of the atmosphere to which the present problem is confined.

Boundary Conditions for the Atmospheric Shear Flow

The thickness of the atmospheric boundary layer is of the order of 1,000 meters. Thus the outer boundary condition for the problem under consideration is specified from within this shear layer. At the ground no-slip condition must be satisfied. In an equilibrium turbulent boundary layer the logarithmic velocity profile is given by [36]

$$u = \frac{u^*}{\kappa} \ln \frac{z+z_0}{z_0} . \tag{3.4}$$

The introduction of the surface roughness parameter, z_0, ensures that the mixing length does not vanish at the surface; and hence the turbulence is not zero at the surface ($z = 0$). The friction velocity, u^*, is taken to be constant from the assumption that the boundary layer is a constant stress layer ($\tau_{xz} = \tau_w$).

Eddy Viscosity Model

For a laminar incompressible flow molecular viscosity, μ, can be assumed constant; but in a turbulent flow the effective viscosity, μ_{eff}, comprised of turbulent and laminar parts, is given by

$$\mu_{eff} = \mu + \mu_t , \tag{3.5}$$

where μ_t , also called the eddy viscosity, is a function of the velocity gradients. From Prandtl's mixing-length hypothesis,

$$\mu_t = \rho \ell^2 \left| \frac{\partial u}{\partial z} \right| , \tag{3.6}$$

with the mixing length,

$$\ell = \kappa (z + z_0) \ . \tag{3.7}$$

Equation (3.7) is valid in the immediate vicinity of the wall. Away from the wall the mixing length distribution depends on the flow situation. Equation (3.6), applicable to boundary layer type of flow, gives a zero viscosity for $\frac{\partial u}{\partial z} = 0$ which is not necessarily true for recirculating flows where the velocity gradients, $\frac{\partial u}{\partial z}$ and $\frac{\partial v}{\partial x}$, may be comparable in magnitude. Hence the eddy viscosity model used in the present study is taken as

$$\mu_t = \rho \ell^2 \{ (\frac{\partial u}{\partial z})^2 + (\frac{\partial v}{\partial x})^2 \}^{1/2} \ . \tag{3.8}$$

Essentially, the turbulent flow has been treated as one with turbulent viscosity as its transport property which is a function of the location of the flow region. For recirculating flows, however, where the relations between stresses and velocity gradients are complicated and not yet known [37], the eddy viscosity model is unsatisfactory. Therefore,

one is lead to a more detailed model of turbulence developed by Prandtl and Kolmogorov.

Prandtl-Kolmogorov Model of Turbulence

According to the Prandtl-Kolmogorov model, hereafter referred to as the TKL model, the turbulence kinetic energy, k, and turbulence length scale, ℓ, characterize the state of local turbulence. This model provides a better formula for determining the turbulent viscosity since for recirculating flows where the mean velocity gradient vanishes, the turbulence energy is not necessarily zero.

Algebraic equations for the transport properties. The TKL model relates k and ℓ to the effective viscosity by the relationship,

$$\mu_{eff} = C_{\mu} \rho k^{1/2} \ell , \tag{3.9}$$

where k and ℓ are the local values, and C_{μ} is a function of turbulence Reynolds number which is defined as

$$R_t = \frac{\mu_t}{\mu} , \tag{3.10}$$

where the Prandtl-Kolmogorov formula for turbulent viscosity [37] is given by

$$\mu_t = \rho k^{1/2} \ell , \tag{3.11}$$

it can be argued that when R_t is small, turbulence is

negligible and the function, C_μ , tends to $1/R_t$. On the other hand, when R_t is large, it takes on a constant asymptotic value, C_{μ_∞}. Researchers have used different asymptotic values for C_μ for different flow situations, but no "universality" in its value has been found so far. The knowledge of the behavior of C_μ as a function of R_t in its intermediate range is also not satisfactory [38].

From Equations (3.5), (3.9), (3.10), and (3.11), the following relation emerges:

$$C_\mu = 1 + 1/R_t \ , \tag{3.12}$$

which implies that $C_{\mu_\infty} = 1$. This value has been used in different flow situations [38], but in recirculating flows it is different from 1. Further discussion on C_{μ_∞} will appear in the sections on selection of constants and their parametric study. In general,

$$C_\mu = C_{\mu_\infty} + 1/R_t \ . \tag{3.12a}$$

Equations to be Solved

Differential equations for the vorticity, ω, and the stream function, ψ, are obtained from Equations (3.1), (3.2), and (3.3) by making use of the following transformations.

Define a two-dimensional vorticity about the y-axis,

$$\omega = \frac{\partial v}{\partial x} - \frac{\partial u}{\partial z} , \tag{3.13}$$

and a stream function, ψ, such that

$$u = \frac{1}{\rho} \frac{\partial \psi}{\partial z} , \tag{3.14}$$

$$v = - \frac{1}{\rho} \frac{\partial \psi}{\partial x} . \tag{3.15}$$

Introducing ψ into Equation (3.13), eliminating pressure from Equations (3.2) and (3.3), and introducing ω and ψ into the resultant equation gives the Poisson equation for the stream function and the transport equation for vorticity, respectively. Both of these equations can be expressed in the following general form of the elliptic equation [38],

$$\left[a\left\{\frac{\partial}{\partial x}\left(\phi\frac{\partial \psi}{\partial z}\right) - \frac{\partial}{\partial z}\left(\phi\frac{\partial \psi}{\partial x}\right)\right\}\right]$$

$$- \left[\frac{\partial}{\partial x}\left\{b\frac{\partial}{\partial x}(c\phi)\right\} + \frac{\partial}{\partial z}\left\{b\frac{\partial}{\partial z}(c\phi)\right\}\right] + d = 0 , \tag{3.16}$$

where the coefficient functions, a, b, c, and d, and the dependent variable, ϕ, are given in Tables 3-1 and 3-2. In Equation (3.16) the terms in the first pair of brackets are

TABLE 3-1

COEFFICIENT FUNCTIONS OF EQUATION (3.16)

ϕ	a	b	c	d
ψ	0	$1/\rho$	1	$-\omega$
ω	1	1	μ_{eff}	$-S_{\omega}$
k	1	$\Gamma_{k,eff} = \frac{\mu_{eff}}{\sigma_{k,eff}}$	1	$-S_k$
ℓ	1	$\Gamma_{\ell,eff}$	1	$-S_{\ell}$

TABLE 3-2

EXPRESSIONS FOR THE SOURCE TERM, -d

ϕ	S_ϕ
ψ	ω
ω	$2\left[-\frac{\partial u}{\partial x}\frac{\partial^2 \mu_{eff}}{\partial x\,\partial z} - \frac{\partial v}{\partial x}\frac{\partial^2 \mu_{eff}}{\partial z^2} + \frac{\partial u}{\partial z}\frac{\partial^2 \mu_{eff}}{\partial x^2} + \frac{\partial v}{\partial x}\frac{\partial^2 \mu_{eff}}{\partial z\,\partial x}\right]$
k	$\underbrace{\mu_t\left[2\left\{\left(\frac{\partial u}{\partial x}\right)^2 + \left(\frac{\partial v}{\partial z}\right)^2\right\} + \left\{\frac{\partial u}{\partial z} + \frac{\partial v}{\partial x}\right\}^2\right]}_{W_{skt}} - \frac{\rho k^{3/2} C_d}{\ell}$
ℓ	$\rho k^{1/2} C_s - \frac{\ell}{k}\underbrace{\mu_t\left[2\left\{\left(\frac{\partial u}{\partial x}\right)^2 + \left(\frac{\partial v}{\partial z}\right)^2\right\} + \left\{\frac{\partial u}{\partial z} + \frac{\partial v}{\partial x}\right\}^2\right]}_{W_{skt}} C_b$

the convection terms, those in the second one are the diffusion terms, and the last one is the source term.

Gosman, et al. [38], derived a differential equation for k, and Rotta [39] proposed a differential equation for ℓ, both of which can be expressed in the form of Equation (3.16).

Referring to Tables 3-1 and 3-2, the term in brackets multiplying μ_t in the source term for the k-equation is the production term; the second term represents energy dissipation. The term containing C_s in the ℓ-equation represents the rate of increase or "stretching" of the length scale, and the second one represents the decrease or "breaking" of the length scale. The coefficients, C_d and C_s , are believed to behave with R_t like C_μ given in Equation (3.12a) [38].

Solutions for laminar flow were determined at different Reynolds numbers solving the two partial differential equations (pde) for ω and ψ. Turbulent flows were solved using the eddy viscosity model introduced into these equations for intermediate values of Reynolds number. For higher Reynolds-number turbulent flow, the TKL model was employed which introduces the two additional partial differential equations for k and ℓ in the analysis.

Derivation of the Finite-Difference Equation

The finite-difference equation (fde) has been derived by integrating the general pde given by Equation

(3.16) over a finite area, assuming that the distribution of the variables between the nodes of the grid is known.

Integration of Equation (3.16) over the rectangular domain (sides of the rectangle lie midway between the neighboring grid lines) shown by dotted lines in Figure 3-1, page 65, will give

$$a \int_{x_w}^{x_e} \int_{z_s}^{z_n} \{\frac{\partial}{\partial x}(\phi\frac{\partial \psi}{\partial z}) - \frac{\partial}{\partial z}(\phi\frac{\partial \psi}{\partial x})\}\, dx\, dz$$

$$- \int_{x_w}^{x_e} \int_{z_s}^{z_n} [\frac{\partial}{\partial x}\{b\frac{\partial}{\partial x}(c\phi) + \frac{\partial}{\partial z}\{b\frac{\partial}{\partial z}(c\phi)\}]dx\, dz$$

$$+ \int_{x_w}^{x_e} \int_{z_s}^{z_n} d\, dx\, dz = 0 \ .$$

To illustrate the principles involved in integrating the convection terms, one of the four integrals, namely,

$$a \int_{s}^{n} \phi_e (\frac{\partial \psi}{\partial z})_e \, dz \ ,$$

is integrated as follows:

Assuming that ϕ and ψ are well-behaved functions and that an average value of ϕ_e exists, which can be given by

$$\overline{\phi}_e = \frac{\int_{z_s}^{z_n} \phi_e \left(\frac{\partial \psi}{\partial z}\right)_e dz}{\int_{z_s}^{z_n} \left(\frac{\partial \psi}{\partial z}\right)_e dz} ,$$

the integral takes the finite difference form

$$a\overline{\phi}_e(\psi_{ne} - \psi_{se}) .$$

Assuming that ϕ within each rectangle in Figure 3-1, page 65, has a constant value equivalent to that at the centrally enclosed node, P, and that the $\overline{\phi}_e$ takes on the ϕ-value possessed by the fluid upstream of the e-face of the rectangle, the upwind differencing effect is introduced into the integral by the following finite difference form:

$$a[\phi_E\{\frac{(\psi_{ne}-\psi_{se})-|\psi_{ne}-\psi_{se}|}{2}\} + \phi_P\{\frac{(\psi_{ne}-\psi_{se})+|\psi_{ne}-\psi_{se}|}{2}\}] .$$

If the flow direction is from P to E, then $\psi_{ne} - \psi_{se}$ is positive and hence

$$\overline{\phi}_e = \phi_P .$$

If the flow direction is from E to P, then

$$\overline{\phi}_e = \phi_E .$$

Also, assuming that the ψ-value at a particular corner of the rectangle is equal to the average of the four neighboring node values, ψ_{ne} , for example, can be given by

$$\psi_{ne} \approx \frac{\psi_{NE} + \psi_N + \psi_P + \psi_E}{4} .$$

The remaining convection terms are integrated similarly.

Considering the first term in the set of four diffusion terms, namely,

$$\int_{z_s}^{z_n} b_e \{\frac{\partial}{\partial x}(c\phi)\}_e \, dz ,$$

it is assumed that b and $(c\phi)$ can be approximated as varying linearly with x so that

$$b_e \approx \frac{b_E + b_P}{2}$$

and

$$\frac{\partial}{\partial x}(c\phi) \approx \frac{c_E\phi_E - c_P\phi_P}{x_E - x_P} .$$

Thus the finite difference form of the first diffusion term is

$$\frac{b_E + b_P}{2} \frac{c_E\phi_E - c_P\phi_P}{x_E - x_P}(z_n - z_s) ,$$

with the other diffusion terms having similar expressions.

Finally, the last term,

$$\int_{x_w}^{x_e} \int_{z_s}^{z_n} d \, dx \, dz \ ,$$

is integrated by assuming that the value of d is constant over the area of integration and is equal to that at the centrally enclosed node, P; thus the source term becomes

$$d_P(x_e - x_w)(z_n - z_s) \ .$$

On rearrangement and simplification the following fde is obtained from integration of Equation (3.16) [38]:

$$A_E(\phi_P - \phi_E) + A_W(\phi_P - \phi_W) + A_N(\phi_P - \phi_N) + A_S(\phi_P - \phi_S)$$

$$- B_E(c_E\phi_E - c_P\phi_P) - B_W(c_W\phi_W - c_P\phi_P) - B_W(c_N\phi_N - c_P\phi_P)$$

$$- B_S(c_S\phi_S - c_P\phi_P) + d_PV_P = 0 \ , \qquad (3.17)$$

where the A's, the coefficients in the convective terms, are given by

$$A_E = \frac{a_P}{8}[(\psi_{SE}+\psi_S-\psi_{NE}-\psi_N)+\left|\psi_{SE}+\psi_S-\psi_{NE}-\psi_N\right|] \ ,$$

$$A_W = \frac{a_P}{8}[(\psi_{NW}+\psi_N-\psi_{SW}-\psi_S)+\left|\psi_{NW}+\psi_N-\psi_{SW}-\psi_S\right|] \ ,$$

$$A_N = \frac{a_P}{8}[(\psi_{NE}+\psi_E-\psi_{NW}-\psi_W)+\left|\psi_{NE}+\psi_E-\psi_{NW}-\psi_W\right|] ,$$

$$A_S = \frac{a_P}{8}[(\psi_{SW}+\psi_W-\psi_{SE}-\psi_E)+\left|\psi_{SW}+\psi_W-\psi_{SE}-\psi_E\right|] , \quad (3.17a)$$

and the B's, the coefficients in the diffusion terms, are given by

$$B_E = \frac{b_E+b_P}{4}\frac{z_N-z_S}{x_E-x_P} ,$$

$$B_W = \frac{b_W+b_P}{4}\frac{z_N-s_S}{x_P-x_W} ,$$

$$B_N = \frac{b_N+b_P}{4}\frac{x_E-x_W}{z_N-z_P} ,$$

$$B_S = \frac{b_S+b_P}{4}\frac{x_E-x_W}{z_P-z_S} , \quad (3.17b)$$

and

$$V_P = (\frac{x_E-x_W}{2})(\frac{z_N-z_S}{2}) . \quad (3.17c)$$

The first order derivatives, for example, $\frac{\partial\phi}{\partial z}$ of the dependent variable, ϕ, are approximated as follows:

$$\frac{\partial\phi}{\partial z} = \frac{(\phi_N-\phi_P)\frac{z_P-z_S}{z_N-z_P} + (\phi_P-\phi_S)\frac{z_N-z_S}{z_P-z_S}}{z_N - z_S} . \quad (3.17d)$$

It may be noted that in deriving the coefficients in the convective terms, use was made of "upwind

differencing" for first order terms so that the A's are always positive. This implies that the transportive property is advected in the direction of velocity which is realistic. The stability of the solution procedure improves considerably using upwind differencing. The coefficients in the diffusion terms, the B's, are dependent on the grid spacing and are also all positive. One of the assumptions made in reducing the diffusion terms to their finite difference form is that b and ($c\phi$) vary linearly with x over the domain of integration (Figure 3-1, page 65).

Complete Successive Substitution Formula

Equation (3.17) can be written as

$$\phi_P = C_E\phi_E + C_W\phi_W + C_N\phi_N + C_S\phi_S + D \ , \qquad (3.18)$$

where

$$C_E = (A_E + B_E c_E)/\Sigma \ AB \ ,$$

$$C_W = (A_W + B_W c_W)/\Sigma \ AB \ ,$$

$$C_N = (A_N + B_N c_N)/\Sigma \ AB \ ,$$

$$C_S = (A_S + B_S c_S)/\Sigma \ AB \ ,$$

$$D = - d_P V_P/\Sigma \ AB \ ,$$

and

$$\Sigma \ AB = A_E + A_W + A_N + A_S + c_P(B_E + B_W + B_N + B_S) \ ,$$

where the C's are all positive.

This substitution formula can be applied at every interior node in the flow field. The simultaneous nonlinear equations for ω, ψ, k, and ℓ given by the general equation (Equation (3.18)) are solved by a Gauss-Seidel iterative procedure.

Equation (3.18) for k can be written as

$$k_P = C_E k_E + C_W k_W + C_N k_N + C_S k_S + S_{k,P} V_P / \Sigma\ AB \ ,$$

where the source term, $S_{k,P}$, is given in Table 3-2, page 72. This formula has been modified [38] by rearrangement to give (refer to Table 3-2)

$$k_P = \frac{C_E k_E + C_W k_W + C_N k_N + C_S k_S + W_{skt,P} V_P / \Sigma\ AB}{1 + \frac{V_P}{\Sigma AB} \left(C_d \rho k^{1/2} / \ell\right)_P} \ . \qquad (3.18a)$$

For ℓ, Equation (3.18) becomes

$$\ell_P = C_E \ell_E + C_W \ell_W + C_N \ell_N + C_S \ell_S + \left(\rho k^{1/2} C_s - \frac{\ell}{k} W_{skt} C_b\right)_P \frac{V_P}{\Sigma AB} \ ,$$

which can be rearranged to yield

$$\ell_P = \frac{C_E \ell_E + C_W \ell_W + C_N \ell_N + C_S \ell_S + V_P \left(\rho k^{1/2} C_s\right)_P / \Sigma\ AB}{1 + \frac{V_P}{\Sigma AB} \left(W_{skt} C_b / k\right)_P} \ . \qquad (3.18b)$$

The advantages in using Equations (3.18a), (3.18b), and the implicit substitution formula for ω (Equation (3.31)), which is given in the section on boundary conditions, will be discussed in the section on convergence of the solution procedure.

Setting Up and Discussion of the Boundary Conditions

Referring to Figure 3-2 and considering the flow field enclosed in a control volume 1-2-3-4-5-6-1 with a unit depth perpendicular to the plane of the paper, flow enters at 1-6, the inlet, and passes over the back-step 1-2-3 and leaves at 4-5, the outlet. The lower boundary 1-2-3-4 comprises the top face of the step 1-2, the base 2-3, and the ground 3-4. Surface 5-6 is referred to as the upper boundary. The Cartesian coordinate system is shown in Figure 3-2 with the origin at station 3.

The boundary conditions (b.c.) prescribed on ϕ are either of flux-type or of normal-gradient-type, except at the inlet and the outlet where the ϕ values prescribed are also related to the values of the horizontal component of velocity for all locations on the boundary. The normal-gradient-type boundary conditions retard the rate of convergence in comparison with the flux-type boundary conditions.

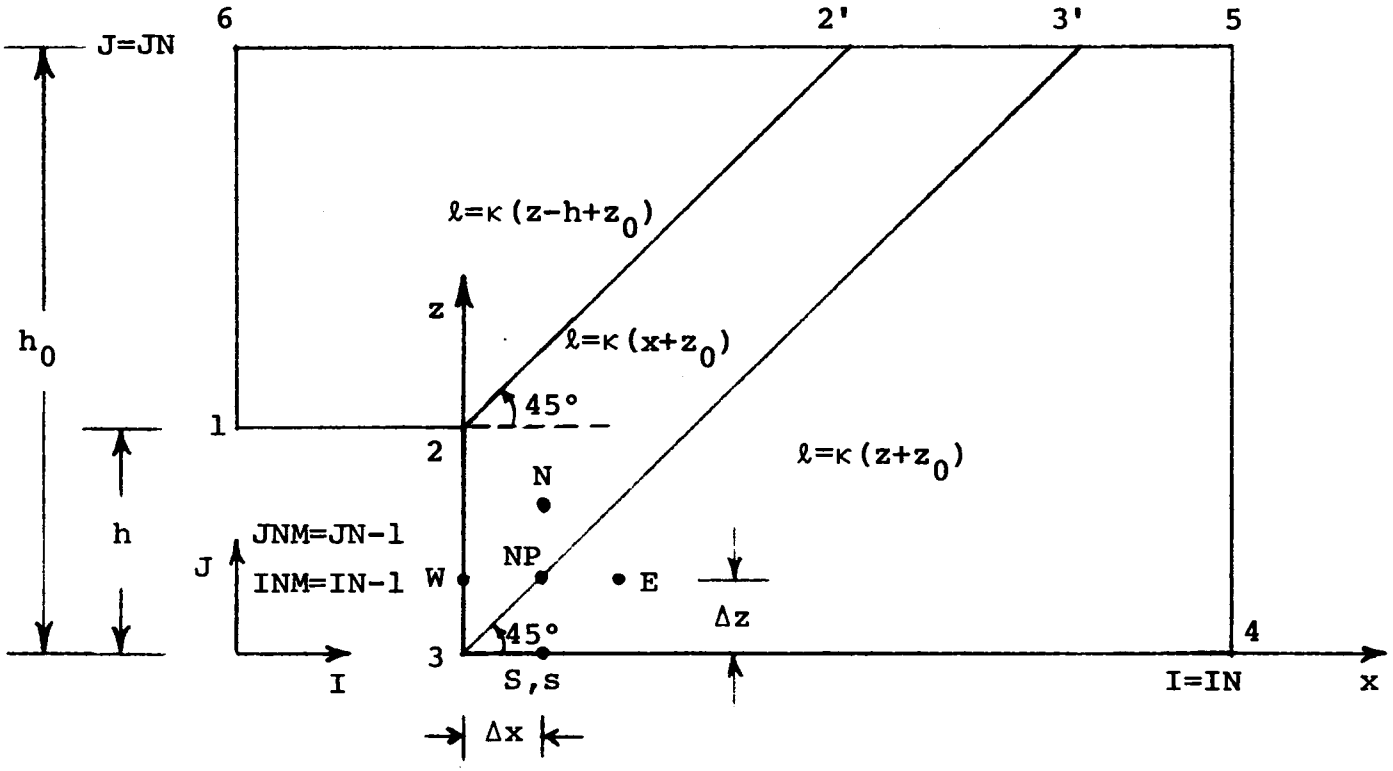


Figure 3-2. Distribution of the mixing length in the flow field enclosed by the control volume 1-2-3-4-5-6-1.

Algebraic equations for and substitution formulae derived from the boundary conditions. At the inlet and outlet, logarithmic velocity profile (Equation (3.4)) typical to an equilibrium atmospheric boundary layer is prescribed with different shear stress velocities. At the outlet, the reference velocity, u_r , is prescribed at the right-hand corner of the upper boundary so that u_0^* is given by

$$u_0^* = \frac{\kappa u_r}{\ell n \frac{h+z_0}{z_0}} . \tag{3.19}$$

Considering the upper boundary to be in the undisturbed flow and applying the continuity equation,

$$\int_h^{h_0} \frac{u_i^*}{\kappa} \ell n \frac{z+z_0}{z_0} \, dz = \int_0^{h_0} \frac{u_0^*}{\kappa} \ell n \frac{z+z_0}{z_0} \, dz ,$$

so that the friction velocity at the outlet becomes

$$u_i^* = \frac{u_0^* [\frac{h_0+z_0}{z_0}(\ell n \frac{h_0+z_0}{z_0} - 1) + 1]}{[\frac{h_0-h+z_0}{z_0}(\ell n \frac{h_0-h+z_0}{z_0} - 1) + 1]} . \tag{3.20}$$

Equations (3.19) and (3.20) imply that ψ is constant along 5-6.

Boundary conditions for the stream function. The description of the boundary conditions on ψ that were used in the numerical solution of the problem is as follows:

The boundary conditions on different boundaries are:

Inlet

$$\psi = \int_h^z \frac{\partial \psi}{\partial z}\, dz = \frac{\rho u_i^* z_0}{\kappa}\left[\frac{z-h+z_0}{z_0}\left(\ell n\, \frac{z-h+z_0}{z_0} - 1\right) + 1\right] . \qquad (3.21)$$

Outlet

$$\psi = \int_0^z \frac{\partial \psi}{\partial z}\, dz = \frac{\rho u_0^* z_0}{\kappa}\left[\frac{z+z_0}{z_0}\left(\ell n\, \frac{z+z_0}{z_0} - 1\right) + 1\right] . \qquad (3.22)$$

Lower Boundary

$$\psi = 0 \text{ (no-slip condition)} .$$

Upper Boundary

$$\psi = \psi_6 = \text{constant} .$$

Unless the outlet is sufficiently far downstream, fixing ψ there through the logarithmic velocity profile may cause the solution to be rather unrealistic. In the present problem the outlet has been taken far enough downstream that the logarithmic velocity profile is a reasonable approximation to the real flow situation. In order that the outlet

b.c. could exactly represent the true physical situation which theoretically occurs at infinity, use would have to be made of a transformation like $\eta = \frac{x}{x+1}$ which maps the semi-infinite axis, $0 \leq x < \infty$, into $0 \leq \eta < 1$ [40]. As the asymptotic behavior of the outlet velocity profile is that of the logarithmic velocity profile, this transformation could hold promise; but care would have to be taken in choosing the proper grid distribution, especially in the recirculation region. Using this mapping also introduces some more gradient terms in the source term of Equation (3.16), which can influence the behavior of the iterative process as far as convergence is concerned.

Roache and Mueller [41] used a floating b.c. on ψ at the outlet:

$$\frac{\partial^2 \psi}{\partial x^2} = 0$$

with (3.23)

$$\frac{\partial \omega}{\partial x} = 0 \ ,$$

which amounts to extrapolating ψ linearly as

$$\psi_{IN} = 2\psi_{INM} - \psi_{INM-1} \ .$$

The preceding relation is valid for a uniform grid near the outlet in the x-direction. The authors [41] report that Equation (3.23) failed for low Reynolds numbers as it gives

an abrupt variation of ω near the outlet. However, for high Reynolds numbers it gives good results. To use these boundary conditions at the outlet, u_r is taken as the reference velocity at the inlet at the upper boundary so that

$$u_i^* = \frac{\kappa u_r}{\ell n \frac{h_0 - h + z_0}{z_0}} \, . \tag{3.24}$$

This specifies the inflow b.c. on ψ given by Equation (3.21). The b.c. for the outlet given by Equation (3.23) along with Equations (3.24) and (3.21) have also been investigated for the problem under consideration. Further discussion of these boundary conditions appears in the section on discussion of results.

Boundary conditions for the vorticity. The vorticity boundary conditions as prescribed on the various boundaries are given below.

Inlet

At the inlet the following equation for ω was used with Equation (3.21) for ψ with either of the equations, Equation (3.20) or Equation (3.24):

$$\omega = \frac{\partial v}{\partial x} - \frac{\partial u}{\partial z} \, ,$$

or

$$\omega = -2\left[\frac{\frac{\psi_3-\psi_2}{x_3-x_2} - \frac{\psi_2-\psi_1}{x_2-x_1}}{\rho(x_3-x_1)}\right] - \frac{u_i^*}{\kappa(z+z_0)} \quad . \tag{3.25}$$

The expression for $\frac{\partial v}{\partial x}$ in the above equation follows from the second order Taylor expansion neglecting $\frac{\partial^3 \psi}{\partial x^3}$ and higher order terms, whence

$$\frac{\partial^2 v}{\partial x^2} = 0 \quad . \tag{3.26}$$

Equation (3.25) allows $\frac{\partial v}{\partial x}$ to develop as a part of the solution. The flow is thus not completely specified at the inlet lest the elliptic nature of the problem be restricted [42].

Outlet

With the b.c. on ψ given by Equation (3.22), the following b.c. on ω was employed:

$$\omega = -2\left[\frac{\frac{\psi_{IN}-\psi_{INM}}{x_{IN}-x_{INM}} - \frac{\psi_{INM}-\psi_{INM-1}}{x_{INM}-x_{INM-1}}}{\rho(x_{IN}-x_{INM-1})}\right] - \frac{u_0^*}{\kappa(z+z_0)} \quad . \tag{3.27}$$

Upper Boundary

$$\omega = \frac{\partial v}{\partial x} - \frac{\partial u}{\partial z} \quad .$$

As $\frac{\partial^2 \psi}{\partial x^2}$ at the upper boundary is zero, it follows that

$$\omega = -\frac{\partial u}{\partial z} \quad .$$

Extrapolating u linearly to the upper boundary requires

$$\frac{\partial^2 u}{\partial z^2} = 0 \ , \ \text{i.e.,} \ \frac{\partial \omega}{\partial z} = 0 \ ,$$

which gives the relation,

$$\omega_{IN} = \omega_{INM} \ , \tag{3.28}$$

as used by Roache and Mueller [41].

Lower Boundary

Using the no-slip condition, the continuity equation, and the fact that v = 0 along the lower boundary, and by retaining the third order terms in the Taylor expansion for ψ_{NP} (see Figure 3-2, page 82), Woods [43] arrived at the second order form for vorticity at the solid wall,

$$\omega_s = - \left[\frac{3\psi_{NP}}{\rho(\Delta z)^2} + \frac{\omega_{NP}}{2}\right] + 0(\Delta z^2) \ , \tag{3.29}$$

which assumes that ω varies linearly with the normal distance from the wall. Gosman, et al. [38], have achieved more accurate predictions with Equation (3.29) than with the first order explicit form,

$$\omega_s = - \frac{2\psi_{NP}}{\rho(\Delta n)^2} + 0(\Delta n) \ , \tag{3.30}$$

where n is the normal distance from the wall, and ω_s is the value of vorticity at the solid wall. These two forms are valid for a uniform grid near the wall. Referring to Figure 3-2, page 82, Equation (3.29) can be used implicitly in the substitution formula (Equation (3.18)); and the modified substitution formula for vorticity for the corner node NP, for example, can be written as

$$\omega_{NP} = \frac{C_E\omega_E + C_N\omega_N - \frac{3}{\rho}\left[\frac{C_W\psi_{NP}}{(\Delta x)^2} + \frac{C_S\psi_{NP}}{(\Delta z)^2}\right] + D}{1 + \frac{C_W+C_S}{2}} . \qquad (3.31)$$

If the explicit boundary condition given by Equation (3.30) is used, the appropriate boundary condition at the sharp corner 2 is not well defined, and a number of formulae have been proposed [22]. Two of these are

1. $\omega_2 = 0$.
2. Discontinuous values of vorticity, $-2\psi_{NP}/\rho(\Delta z)^2$ and $-2\psi_{NP}/\rho(\Delta x)^2$ are used, depending on whether the vorticity at the node immediately above 2 or at the one immediately downstream of 2 is being calculated, respectively.

With the implicit scheme (Equation (3.20)), it is unnecessary to specify any b.c. at 2 because the discontinuous nature of vorticity at 2 has already entered the substitution formula (Equation (3.31)). Comparisons of

these explicit and implicit forms were made in the beginning. No appreciable difference was observed although the latter seemed to yield more realistic results.

Boundary conditions for the turbulence kinetic energy. Deriving boundary conditions on k necessitates finding a simple expression for it. Differentiating Equation (3.4) with respect to z will give

$$\frac{\partial u}{\partial z} = \frac{u^*}{\kappa(z+z_0)} \quad . \tag{3.32}$$

Referring to Figure 3-2, page 82, the wall velocity gradient near the ground and the top face of the step will be $\frac{\partial u}{\partial z}$ and that near the base will be $\frac{\partial v}{\partial x}$. Restricting attention for a moment to the regions where $\frac{\partial u}{\partial z} >> \frac{\partial v}{\partial x}$, Equation (3.6) and an expression originally suggested by Boussinesq in analogy to the expression for laminar shear stress, namely,

$$\tau_t = \mu_t \frac{\partial u}{\partial z} \quad ,$$

give the following relation:

$$\tau_{zx_t} = \rho \ell^2 \left|\frac{\partial u}{\partial z}\right| \frac{\partial u}{\partial z} \quad . \tag{3.33}$$

Also,

$$\tau_{eff} = \tau_t + \tau \quad .$$

Using Equation (3.32), laminar shear stress will be given by

$$\tau = \rho\nu \frac{u^*}{\kappa(z+z_0)} .$$

Therefore,

$$\tau_{eff} = \frac{\rho u^*}{\kappa(z+z_0)} \left[\frac{\ell^2 |u^*|}{\kappa(z+z_0)} + \nu\right] . \qquad (3.33a)$$

By definition,

$$\tau_w = \rho u^{*2} .$$

Assuming that the magnitude of the shear stress is constant near the walls and throughout the undisturbed layer,

$$\left|\tau_{eff}\right| = \left|\tau_{eff_w}\right| = \rho u^{*2} . \qquad (3.33b)$$

Equating Equations (3.33a) and (3.33b) gives

$$\ell = \left[\kappa(z+z_0)\left\{\kappa(z+z_0) - \frac{\nu}{u^*}\right\}\right]^{1/2} .$$

Since $\kappa(z+z_0) >> \frac{\nu}{u^*}$, it follows

$$\ell \approx \kappa(z+z_0) . \qquad (3.34)$$

Also,

$$\tau_{eff} = \rho\nu_{eff} \frac{\partial u}{\partial z} . \qquad (3.35)$$

From Equation (3.9),

$$\nu_{eff} = C_\mu k^{1/2} \ell \ .$$

Using Equations (3.32) and (3.34), Equation (3.35) becomes

$$\tau_{eff} = \rho C_\mu k^{1/2} u^* \ . \qquad (3.35a)$$

Equating Equations (3.33b) and (3.35a),

$$k = (u^*/C_\mu)^2 \ . \qquad (3.36)$$

Near the base, $\frac{\partial v}{\partial x} >> \frac{\partial u}{\partial z}$; it is assumed that the velocity variation in v with x is also governed by the logarithmic velocity profile,

$$v = \frac{v^*}{\kappa} \ln \frac{x+z_0}{z_0} \ , \qquad (3.37)$$

so that

$$\frac{\partial v}{\partial x} = \frac{v^*}{\kappa (x+z_0)} \ . \qquad (3.38)$$

Writing the analog of Equation (3.33),

$$\tau_{xz_t} = \rho \ell^2 \left|\frac{\partial v}{\partial x}\right| \frac{\partial v}{\partial x} \ ,$$

and following the same reasoning as before, it can be seen that near the base

$$\ell \approx \kappa(x+z_0) \ , \tag{3.39}$$

and

$$k = \left(\frac{v^*}{C_\mu}\right)^2 \ . \tag{3.40}$$

Equations (3.10), (3.11), (3.12a), (3.34), and (3.36) give

$$k = \left[\left\{u^* - \frac{\mu}{\rho\kappa(z+z_0)}\right\} \frac{1}{C_{\mu_\infty}}\right]^2 \ . \tag{3.41}$$

Similarly, Equations (3.10), (3.11), (3.12a), (3.39), and (3.40) yield

$$k = \left[\left\{v^* - \frac{\mu}{\rho\kappa(x+z_0)}\right\} \frac{1}{C_{\mu_\infty}}\right]^2 \ . \tag{3.42}$$

For the inlet and outlet, $\frac{\partial u}{\partial z} >> \frac{\partial v}{\partial x}$; therefore, at the inlet,

$$k = \left[\left\{u_i^* - \frac{\mu}{\rho(z+z_0)}\right\} \frac{1}{C_{\mu_\infty}}\right]^2 \ , \tag{3.43}$$

and at the outlet,

$$k = \left[\left\{u_0^* - \frac{\mu}{\rho(z+z_0)}\right\} \frac{1}{C_{\mu_\infty}}\right]^2 \ . \tag{3.44}$$

With these boundary conditions, k is fixed at the inlet and the outlet. But, corresponding to Equation (3.23), a floating b.c.,

$$\frac{\partial^2 k}{\partial x^2} = 0 \ ,$$

was used at the outlet, which gives

$$k_{IN} = 2k_{INM} - k_{INM-1} \ . \qquad (3.44a)$$

At the upper boundary the b.c. is $\frac{\partial k}{\partial z} = 0$, which in finite difference form is

$$k_{JN} = k_{JNM} \ . \qquad (3.45)$$

At the lower boundary the b.c. on k can be derived as follows. From Equations (3.32) and (3.38), respectively,

$$u^* = \frac{\kappa(z+z_0)}{\rho} \frac{\partial^2 \psi}{\partial z^2}$$

and

$$v^* = - \frac{\kappa(x+z_0)}{\rho} \frac{\partial^2 \psi}{\partial x^2} \ ,$$

where the following expressions for

$$\frac{\partial^2 \psi}{\partial z^2}$$

and

$$\frac{\partial^2 \psi}{\partial x^2}$$

at the respective walls, obtained by using Taylor series in which third and higher order terms are neglected, are $2\psi_{NP}/(\Delta z)^2$ and $2\psi_{NP}/(\Delta x)^2$, respectively (see Figure 3-2, page 82). Therefore, the preceding two equations at the respective walls become

$$u^* = \frac{2\kappa z_0 \psi_{NP}}{\rho (\Delta z)^2} \tag{3.46}$$

and

$$v^* = - \frac{2\kappa z_0 \psi_{NP}}{\rho (\Delta x)^2} \, . \tag{3.47}$$

Referring to the corner node NP (Figure 3-2), Equations (3.41) and (3.46) give

$$k_S = \left[\frac{1}{\rho C_{\mu_\infty}} \left\{ \frac{2\kappa z_0 \psi_{NP}}{(\Delta z)^2} - \frac{\mu}{\kappa z_0} \right\}\right]^2 \, . \tag{3.48}$$

Similarly,

$$k_W = \left[\frac{1}{\rho C_{\mu_\infty}} \left\{ - \frac{2\kappa z_0 \psi_{NP}}{(\Delta x)^2} - \frac{\mu}{\kappa z_0} \right\}\right]^2 \, . \tag{3.49}$$

At the sharp corner 2, discontinuous values of k,

$$\left[\frac{1}{\rho C_{\mu_\infty}}\left\{\frac{2\kappa(h+z_0)\psi_{NP}}{(\Delta z)^2} - \frac{\mu}{\kappa(h+z_0)}\right\}\right] ,$$

and the one given by Equation (3.49) are used depending on whether the turbulence kinetic energy, k, at the node immediately above 2 or at the one immediately downstream of 2 is being calculated, respectively.

Boundary conditions on ℓ. Referring to Figure 3-2, page 82, the distribution of the mixing length is shown which is based on the normal distance from the nearest wall. The lines 22' and 33' are inclined at 45° from the positive x-axis. This distribution fixes the mixing length (1) on all the boundaries for the TKL model and (2) everywhere for the eddy viscosity model.

Numerical Solution of the Finite Difference Equation

The nonlinear system of simultaneous algebraic equations given by Equation (3.18) has been solved by the Gauss-Seidel successive substitution technique. The numerical scheme and the computer code developed by Gosman, et al. [38], has been modified for the back-step problem. Successive over-relaxation or under-relaxation on the dependent variable, ϕ, in Equation (3.18) can be readily employed. Both relaxation techniques were used and are discussed later in this chapter.

Equation (3.18) is solved for the vorticity, stream function, turbulence kinetic energy, and the turbulence length scale in that order. Referring to Figure 3-3, the whole flow field is swept row by row in the direction 5 to 4 from the upper boundary to lower boundary, updating ϕ values at the interior nodes using Equation (3.18) and at the wall nodes by the substitution formulae for the boundary conditions. One iteration cycle is complete when all the four equations have been solved and the ϕ-values at the boundary nodes have been updated. This iteration process is carried on till either of the following two convergence criteria has been satisfied:

$$\left(\frac{\phi^n - \phi^{n-1}}{\phi^n}\right)_{max} \leq 0.01 \ , \tag{3.50}$$

$$\left(\frac{\phi^n - \phi^{n-1}}{\phi^{n-1}}\right)_{max} \leq 0.00001 \ . \tag{3.51}$$

The second criterion is necessary because when the magnitude of the ϕ-value at a particular node becomes very small, the variation, $\phi^n - \phi^{n-1}$, at that node can still be larger since it depends on the values at the surrounding nodes; and thus the first criterion is difficult to satisfy even though the rest of the field has converged.

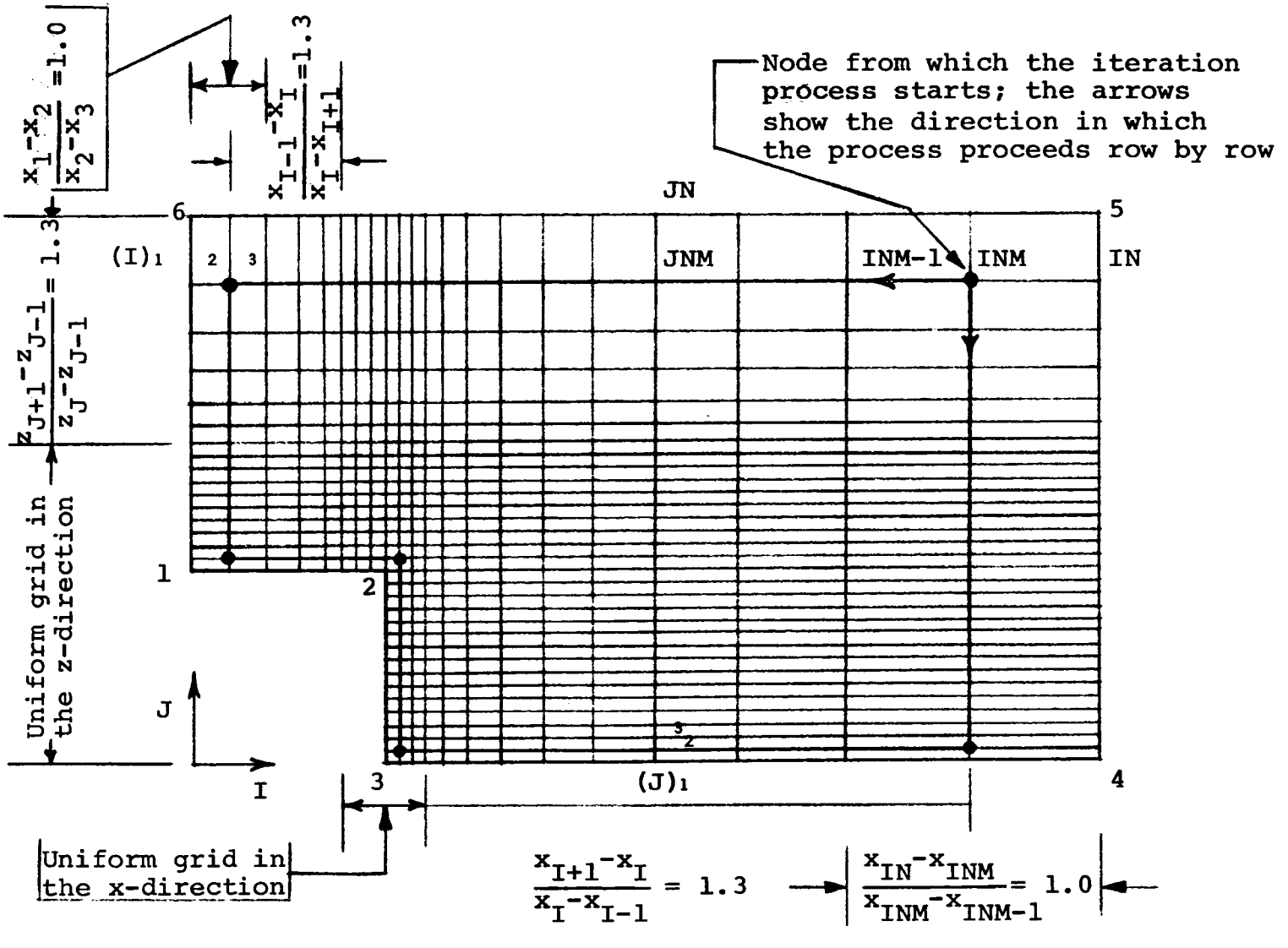


Figure 3-3. Distribution of the finite-difference grid over the entire flow field.

After the convergence is achieved, the u and v components of the velocity are calculated. The stream function and the velocity profiles are plotted as the final results.

Grid Distribution

The variable grid spacing is smaller near the walls where large gradients in ϕ are expected. Moving farther away from the walls, the ratio of the intervals between the nodes has been kept constant and equal to 1.3, that is, the grid spacing increases in geometric progression away from the walls (see Figure 3-3).

Selection of Constants

The selection of the so-called constants, C_μ, appearing in Equation (3.9), and C_d, C_s, and C_b shown in Table 3-2, page 72, is of prime concern in the current turbulence research [37, 38, 44, 45, 46, 47, 48, 49] in the two-equation modeling of turbulence such as the TKL model or the (k-kℓ) model. In the latter model, first proposed by Rotta [50], the dependent variable, kℓ, has replaced ℓ in the TKL model because it does not diffuse at a rate proportional to $\frac{\partial \ell}{\partial z}$. In some models, eddy viscosity, ν_t, is treated as a dependent variable. These models have been used to predict the turbulent flow situations different from that of the rearward-facing step considered herein, and the constants have been evaluated by comparing the predictions

of the models with the experimental data available for various flow situations. For instance, Ng and Spalding [44] predict boundary layer flows near walls from the (k-kℓ) model by using the experimental results for homogeneous shear flows in local equilibrium. A value for C_d equal to 0.1 was obtained thus. The turbulent Prandtl number, σ_k, was taken as unity. Using the (k-kℓ) model, Rodi and Spalding [47] obtained $C_d = 0.09$ for free shear flows while σ_k was taken as 2.0. Launder, et al. [48], used the turbulence kinetic energy dissipation rate, $\varepsilon = k^{3/2}/\ell$, as the dependent variable instead of ℓ. In the (k-ε) model, $C_\mu = 0.09$ and $\sigma_k = 1.0$ were found to produce satisfactory results for various turbulent flows [48]. To treat low Reynolds number flows, Jones and Launder [49] used $C_\mu = 0.09 \times \exp[-2.5/(1+R_t/50)]$ and $\sigma_k = 1.0$.

A three-equation model [48] was used where the third dependent variable considered was the turbulent shear stress, $\rho\overline{u'v'}$. In this model, which was also used to predict two-dimensional axisymmetric jets and wakes, C_μ was taken as 0.09. Wolfshtein [45] used $C_\mu = 0.22$, $C_d = 0.416$, and $\sigma_k = 1.53$ for the Couette flow case.

The incompressible, two-dimensional wake flow is one of the most difficult to predict properly [46]. Apparently, the main difficulty is in predicting the asymptotic rate of decay of the wake, which is a weak-shear problem. Due to the paucity of knowledge regarding these

"constants" for recirculating flows, resort has been taken to the previous information and the computational experiments which are conducted in this study to furnish a reasonable set of constants for the TKL model. Unfortunately, however, these constants are not only different for different flow situations, but vary from one region to the other in the same flow situation as a function of R_t when R_t is small. As R_t becomes very large, $\sigma_{k,eff}$ and $\sigma_{\ell,eff}$ take on constant asymptotic values, provided the hypothesis that k and ℓ are adequate to characterize the state of turbulence is valid. However, the σ's are normally, as in this study also, taken as unity [38]. The following relations define the various constants used for the present investigation.

$$C_b = C_{b_\infty} + 1/R_t \ , \tag{3.52}$$

where

$$C_{b_\infty} = 1.0 \ ,$$

$$C_d = C_{d_\infty} + 1/R_t \ , \tag{3.53}$$

where

$$C_{d_\infty} = 1.0 \ .$$

$$C_s = C_{s_\infty} + 1/R_t \ , \tag{3.54}$$

where

$$C_{s_\infty} = 0.35 \ .$$

Corresponding to Equation (3.12a),

$$C_{\mu_\infty} = 0.1 \ .$$

The above set of constants seems to be a reasonably good selection to begin with. Further discussion on these constants will appear in the parametric study reported later in this study. Efforts to establish some kind of a universal set of constants for recirculating flows are still being carried on.

Discussion on Convergence, Accuracy, and Economy of the Solution Procedure

Convergence. It has been experienced [38] that if a nonuniform grid spacing is used near the walls, both the vorticity b.c. (Equations (3.29) and (3.30)), when used explicitly for updating the vorticity at the wall, may cause divergence due to the coupling of the vorticity and the stream function equations through the vorticity b.c. Gosman, et al. [38], suggested as remedial measures (1) to hold the ratio of the intervals between the nodes (Figure 3-3, page 98) less than 1.5 especially near the wall, where

this ratio should be as close to unity as possible and (2) to use the modified substitution formula for ω (Equation (3.31)).

In calculations carried out in this investigation, convergence seemed to be impaired when a coarse grid with the ratio of the intervals between the nodes was 2 and above, especially in the z-direction.

The coefficients, C's and D, in Equation (3.18) vary from one iteration to the next, and hence this is a nonlinear algebraic equation. However, from experience, Gosman, et al., point out that the convergence criteria for a linear set of algebraic equations to converge are often sufficient for equations such as Equation (3.18) also. As there is no such criteria for the nonlinear equations, the convergence of the solution procedure can be based on the following three criteria for a linear system of algebraic equations:

1. $\sum |C|_P \leq 1$, on every grid node.
2. $\sum |C|_P < 1$, on at least one node.
3. The variation in the C's and D from one iteration to the next is small.

The third criterion restricts the nonlinearity of the coefficients to an extent that they could be treated as linear in the whole iteration procedure, thus making the first two criteria meaningful.

It can be seen that $\sum|C|_P = 1$ on every node in the field if c = 1 (Table 3-1, page 65), which is true for all but the vorticity equation where $c = \mu_{eff}$. For low Reynolds number R, the value of μ_{eff} at the node P is close to those at the surrounding nodes because the gradients are small (refer to the section on discussion of results), and hence $\sum|C|_P$ is close to unity. But for higher R when the gradients in velocity are large, especially in the recirculating region, this criterion fails to be satisfied for the vorticity equation when using the eddy viscosity model (Equation (3.8)) because of the large variations in μ_{eff} between the neighboring nodes. That is why in the computation at high R, using the eddy viscosity model to describe turbulence, divergence was encountered. The remedy for this lies in under-relaxing the variable, ω, or the C's and D coefficients in the vorticity equation. (Further discussion on this will appear later.) To carry on the computation at higher R, the TKL model was used for which no such difficulty was encountered.

If the central-difference schemes for the first order convective terms were used instead of the upwind differencing, the A_E coefficient could become negative [38]; and this could cause C_E to become negative, especially at high R when the stream function values are correspondingly large and hence $|A_E| > cB_E$. Owing to this fact, the

central-difference schemes fail to achieve convergence at high R due to their inability to satisfy the first convergence criterion.

Comparing a flux-type b.c., ϕ = constant, with Equation (3.18), it can be seen that $\sum|C| = 0$; hence the second criterion is satisfied for all but the ω equation, in which case no flux-type b.c. is used anywhere on the boundaries except for the case when a zero vorticity is used at the sharp corner 2, corresponding to the b.c. given by Equation (3.30). However, a comparison of the solution corresponding to the b.c. given by Equation (3.29) to the solutions corresponding to the discontinuous b.c. and zero b.c. given by Equation (3.30) showed no marked change in the rate of convergence. This indicates that either the second criterion is satisfied somewhere at an interior node in the field or else the criterion for Equation (3.18) is generally sufficient and not necessary for convergence; otherwise, divergence should have been encountered.

The third criterion can be satisfied by under-relaxing the dependent variable, ϕ. As a better alternative, the C's and D coefficients should be under-relaxed as they are functions of quantities like μ_{eff} as well as ϕ. In the present computations with the eddy viscosity model incorporated at high values of R, large variations in the source term for the stream function equation (Table 3-2, page 72) were found to occur, and hence the third criterion

was not satisfied. This was detected from the solutions which diverged. Although the strong variations in the source term were first seen as the cause for divergence, it is interesting to note that the failure to satisfy the first and the third criterion is really coupled through the strong velocity gradients and hence through strong variations in μ_{eff}.

The source terms in the k and ℓ equations were under-relaxed in the sense of reducing the iteration-to-iteration variations by recasting Equation (3.18) into Equations (3.18a) and (3.18b), respectively.

In the original form of Equation (3.18) for k, the 3/2 power of k_p induces large variations in the source term and could cause divergence. In the present computations, using Equation (3.18) for ℓ, it was observed that ℓ became negative early in the iteration process due to the comparatively large magnitude of the term,

$$V_P(\ell W_{skt} C_b)_P / k_P^{\Sigma} AB ,$$

which in turn made k negative in Equation (3.18a). To stop ℓ and k from becoming negative, Equation (3.18) for ℓ was rearranged to give Equation (3.18b). Also, in Equations (3.18a) and (3.18b) the denominator is always greater than unity, and hence the first and second criteria are unconditionally satisfied. The third criterion is satisfied as the source term variations are small for the ℓ and k

equations. Obedience to these convergence criteria resulted in a very rapid rate of convergence of the solution for the ℓ and k equations, which testifies to the meaningfulness of the above convergence criteria.

Accuracy and economy. The accuracy and economy of the solution procedure are opposed to one another. The finer the grid size and hence the more the computing time, the better the accuracy or the lesser the truncation error. Wherever one-sided difference, that is, first-order approximation to the first order derivatives has been used, steep gradients are "smeared" especially near the walls. Therefore, it is necessary to use a very fine grid size near the walls and wherever else the gradients are expected to be large. Finer mesh size also satisfies the assumption of linear vorticity near the walls. Wolfshtein [45] found by comparing the exact and the finite-difference solutions for simple cases of Couette flow, impinging jet flow, and uniform velocity flow that a finer grid away from the walls does not make the vorticity solution any better; but the stream function in the middle of the flow field, perhaps due to the strong nonlinearity of its distribution, is sensitive to the grid size. However, by experience it was found that the stream function solution behaved better than the vorticity solution in general; and hence a reasonable distance away from the walls, coarser grids were used to cut down the computing time.

The effect of smearing is to introduce an additional "false" diffusion of ϕ into Equation (3.18), which can be assumed to be represented approximately by the magnitude of the "false exchange coefficient" by the following relation for all types of flows [45]:

$$\frac{\Gamma_{false}}{\Gamma_{eff}} \approx 0.36\ R_{eff}\ \sigma_{eff}\ \frac{\Delta n}{h}\ \sin(2\alpha)\ , \qquad (3.56)$$

where Δn is the square mesh size; α is the angle which the streamlines make with the coordinate system (the mesh lines); $R_{eff} = u_r h/\nu_{eff}$ is the local effective Reynolds number based on the step height, h; and $\sigma_{eff} = \mu_{eff}/\Gamma_{eff}$ is the effective Prandtl or Schmidt number.

As the smearing is associated with the first order derivatives in the convective terms, it becomes important when the viscosity is very small. Hence Equation (3.56) is very demonstrative of how the false diffusion effect can influence the solution in laminar flows as u_r , Δn, or α (from zero to 45°) increase. For laminar flows Equation (3.56) reduces to

$$\Gamma_{false} \approx 0.36\ \rho u_r \Delta n\ \sin(2\alpha)\ . \qquad (3.56a)$$

Defining cell Reynolds number, $R_{cell} = \rho u_r \Delta n/\mu$, Equation (3.56a) becomes

$$\Gamma_{false} \approx 0.36\ R_{cell}\ \mu\ \sin(2\alpha)\ . \qquad (3.56b)$$

Therefore, for laminar flows the importance of the two important parameters, R_{cell} and α, becomes clear. In the literature, for laminar flows the cell Reynolds number has been used as a parameter to control the accuracy (truncation error) of the method used. As α increases from 0 to 45°, the false diffusion effect increases from zero to a maximum, which shows that the curvature of the streamlines is responsible for magnifying this effect. Thus for higher values of R the remedy lies in (1) choosing the correct streamline coordinate, $\alpha = 0°$, and (2) reducing the mesh size, Δn.

From (2) it can be seen that a given accuracy, that is, the truncation error within a reasonable tolerance, can be achieved at the cost of the computing time.

For turbulent flows, however, as Γ_{eff} is usually much larger than Γ (for example, for the ω equation, $\mu_{eff} >> \mu$), and σ_{eff} is close to unity, false diffusion is not very important.

The criterion for convergence has been determined from experience by observing that the solution obtained after a definite number of iterations remains essentially the same for further iterations. It has been experienced that the number of iterations required for convergence increases with an increase in the number of grid nodes; and hence, contrary to what one might expect, the computing time increases more than proportionally to the number of grid

nodes. The number of grid nodes should therefore be kept as low as possible. It is a good practice to provide the initial conditions discreetly in order to quicken the rate of convergence. It has also been experienced that the flux-type boundary conditions are better than the gradient-type boundary conditions as the latter slacken the rate of convergence. So wherever possible the flux-type boundary conditions have been prescribed.

Discussion of Results

The results obtained in the present study correspond to two models of turbulence, the eddy viscosity model (Equation (3.8)) and the TKL model (Equation (3.9)). In the former, a parametric study of Reynolds number was carried out; and in the latter, the influence of variations in the constants defined by Equations (3.12a), (3.52), (3.53), and (3.54) was investigated. While in the eddy viscosity model the empiricism involved is that of the mixing length distribution throughout the flow field, the TKL model is dependent on the value of the constants chosen in the modeled terms. It has been noted [37] that the mixing-length theorem is not adequate to define the turbulence associated with the recirculating flows and that the two-equation turbulence model, like the TKL model, is better suited for such a flow situation. That this is true has been confirmed in this investigation.

With Reynolds number, R, as a parameter the results corresponding to the laminar solutions are discussed first. The results corresponding to the turbulent case with the eddy viscosity model introduced into the governing equations are discussed next. This is followed by a discussion of the results of the TKL model.

Laminar solution (Reynolds number as a parameter). Results for laminar flows were achieved for step-height Reynolds number, $u_r h/\nu$, equal to 6.9, 69, and 6,900 corresponding to the step height, h = 1 cm. The outlet stream function boundary condition given by Equation (3.22) and the implicit substitution formula (Equation (3.31)) for vorticity were used in these computations. Figures 3-4, 3-5, and 3-6 are the streamline plots. On comparing these figures it is seen that the recirculation bubble length becomes larger as the Reynolds number is increased, which is realistic. From Figures 3-7, 3-8, and 3-9, which show the direction of flow (indicated by arrows), it can be seen that there are two contra-rotating eddies in the cavity zone. The corner eddy is smaller than the recirculation eddy. For R = 69, the length of the corner eddy is about 2.5 step heights along the ground and the recirculation eddy is spread over a length of seven step heights. One can observe from the data of Tani, et al. [8], that for a recirculation length of seven step heights, a region of negative surface pressure gradient which corresponds to the corner eddy was

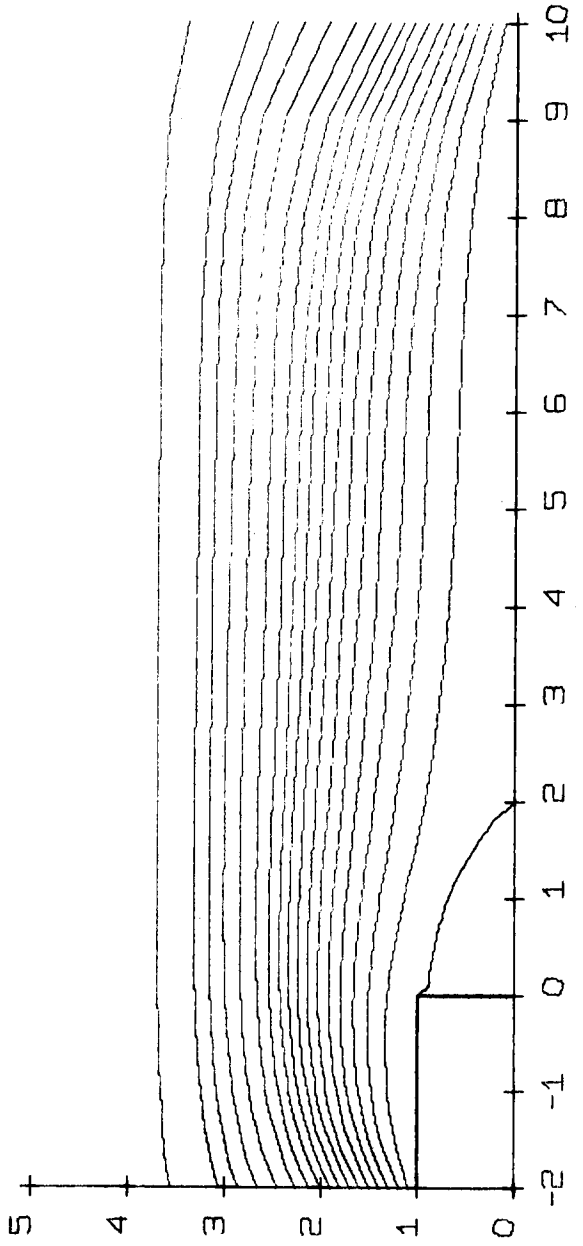


Figure 3-4. Streamlines over a back step in laminar flow (Reynolds number = 6.9).

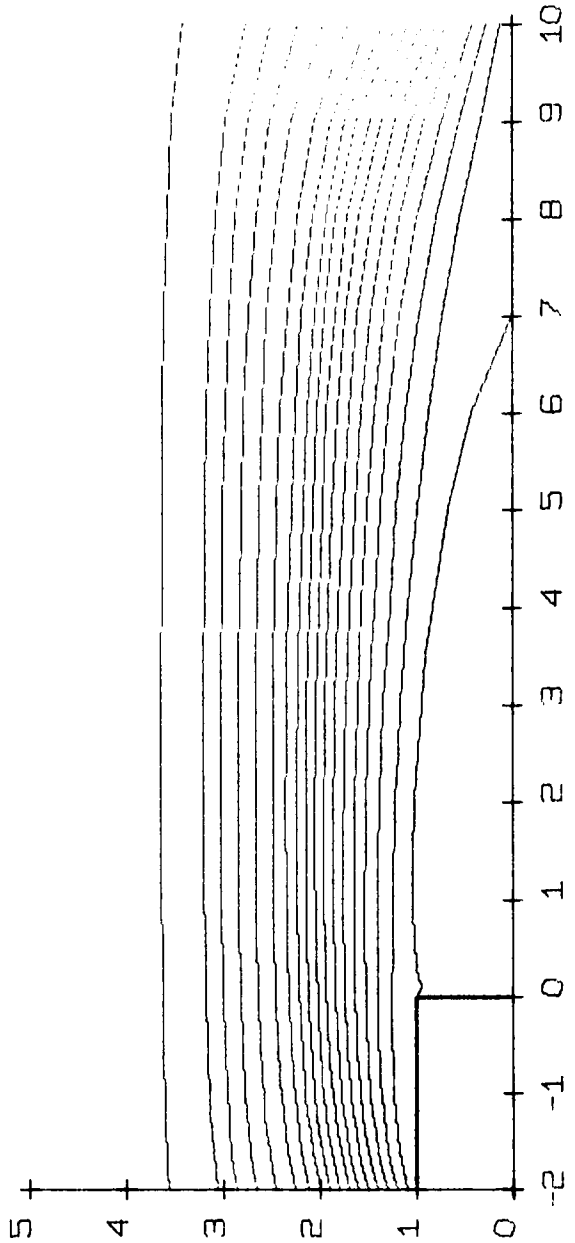


Figure 3-5. Streamlines over a back step in laminar flow (Reynolds number = 69).

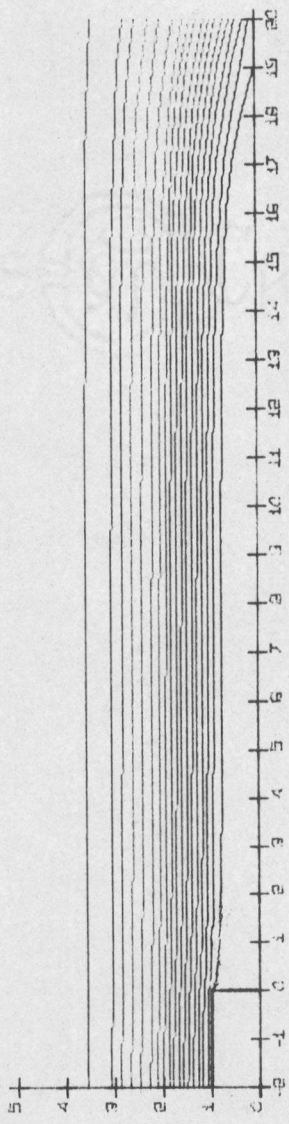


Figure 3-6. Streamlines over a back step in laminar flow (Reynolds number = 6.9×10^3).

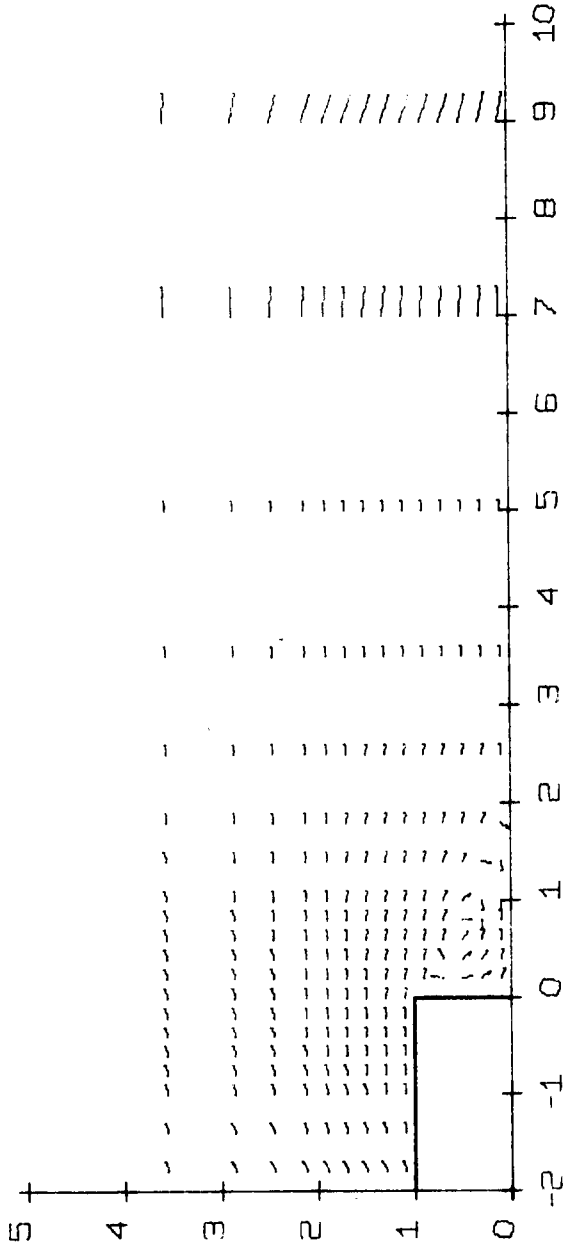


Figure 3-7. Flow direction over a back step in laminar flow (Reynolds number = 6.9).

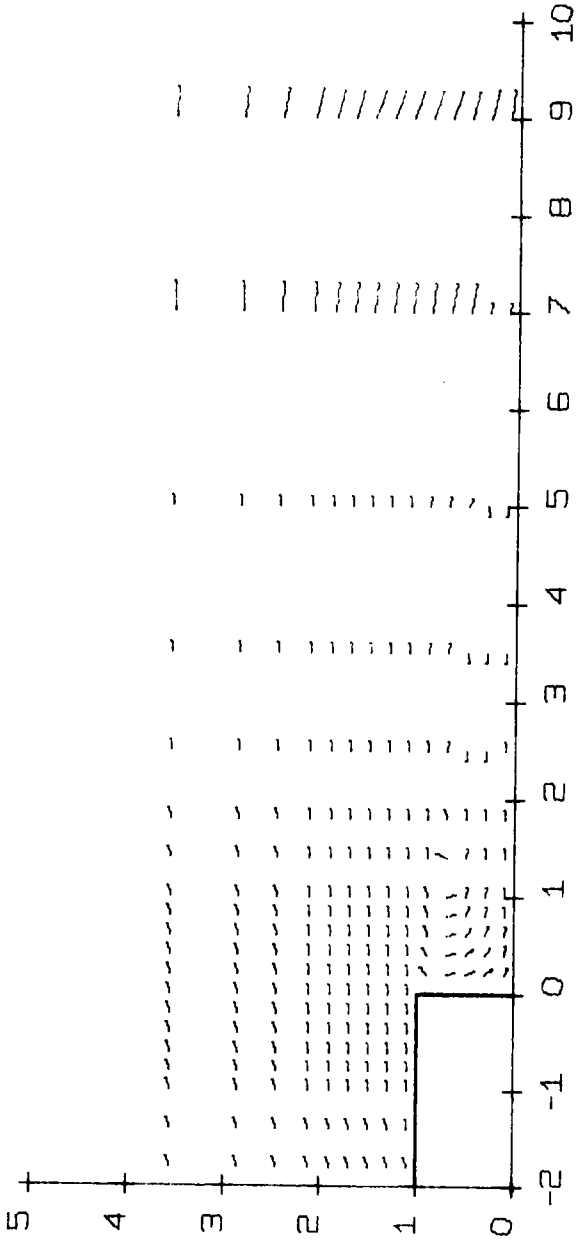


Figure 3-8. Flow direction over a back step in laminar flow (Reynolds number = 69).

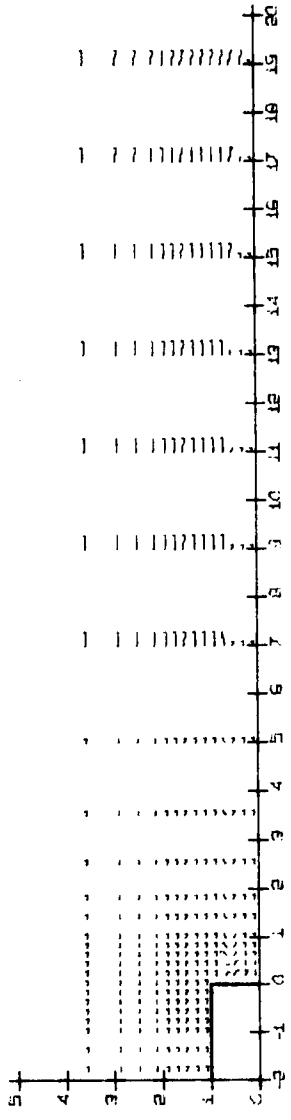


Figure 3-9. Flow direction over a back step in laminar flow (Reynolds number = 6.9×10^3).

found to be about 2.5 step heights long (see Chapter IV). Thus, although the results for such a low Reynolds number laminar flow cannot be compared with these experimental findings which correspond to a turbulent flow, one can observe that the ratio of the length scales of the two eddies is in agreement with that obtained from the experimental data, which gives one a qualitative feel of the relative size of the corner eddy with respect to that of the recirculation eddy.

Also, with the decrease in R the flow seems to separate from a lower location down the base, which is meaningful because at $R \to 0$ the flow would not separate and remain attached to the base right down to the ground. This shift of the separation point down the back side of the step has also been found computationally by Roache and Mueller [41]. As it is not known from what point the flow separates on the base, the plot of the zero streamline is started from the interior point immediately next to the base. At the inlet for R = 6.9 and 69, the upshoot in the streamlines can be attributed to the fact that the logarithmic velocity profile used is not a realistic boundary condition for such low Reynolds numbers. But for R = 6,900, the inflow b.c. is more meaningful as can be seen from Figure 3-6.

It may be pointed out that at R = 6,900 the central-difference schemes used for the first order derivatives in the x-direction will render the method

unstable as discussed earlier. Hung and Macagno [52], in spite of the use of unsteady equations which are believed to be more stable than the steady ones, could not obtain results for Reynolds numbers higher than 333 (using the three-point central-differencing formula in the analysis). With the upwind-differencing used in this study laminar solutions for R still higher than 6,900 could have been achieved. The present study, being primarily concerned with turbulent flow, was, however, at this point directed towards turbulent solutions. Toward this goal the eddy viscosity model was introduced into the governing equations.

Eddy viscosity model (Reynolds number as a parameter). For Reynolds number equal to 6.9, the eddy viscosity model yielded a "turbulent" solution which was more or less like the laminar counterpart. The reason for this can be explained as follows: The maximum velocity gradient, $\frac{\partial u}{\partial z}$, at the ground, $z = 0$, for a surface roughness, $z_0 = 0.01$ cm corresponding to the step height, $h = 1$ cm, is of the order of 2.0 (see Equation (3.57)). Intuitively it can be seen that the order of magnitude of $(\frac{\partial v}{\partial x})_{max}$ at the base should not be very much different from that of $(\frac{\partial u}{\partial z})_{max}$ at the ground. Thus it follows from Equation (3.8) that $\mu_t << \mu$, which explains why the solution remains practically unchanged with the introduction of the eddy viscosity model.

For the turbulent flow calculations the laminar solution was taken as the initial conditions which resulted in rapid convergence. Turbulent solutions obtained, beginning with the same initial conditions as used for the laminar solutions, took much longer to converge.

Next, the eddy viscosity model was introduced into the laminar solution for R = 6,900. The turbulent solution in this case diverged. The cause for divergence was traced to the following:

Considering u_r as the reference velocity at the upper right-hand corner of the control volume (point 5 in Figure 3-2, page 82), Equations (3.4) and (3.38) give

$$\frac{\partial u}{\partial z} = \frac{u_r}{(z+z_0)\,\ell n\,\frac{h_0+z_0}{z_0}} , \qquad (3.57)$$

which shows that the velocity gradient, $\frac{\partial u}{\partial z}$, will be steeper for higher values of u_r ; thus μ_t from Equation (3.8) will be large and correspondingly its variation from node to node will be large. Thus, as discussed earlier in the section on convergence of the solution procedure, divergence was encountered in the vorticity equation and eventually in the stream function equation also.

To overcome this difficulty two remedies are possible:

1. Reducing the mesh size such that the μ_{eff} variation from node to node is sufficiently small.
2. Using under-relaxation on the C's and D coefficients in the vorticity equation or on the vorticity, ω, itself.

As the criterion for selecting a proper mesh size is not known, it is easier to make use of the under-relaxation technique. Under-relaxation was tried on the ω-equation for the case of a higher Reynolds number, $R = 6.9 \times 10^6$, corresponding to the step height, h = 1 meter. The under-relaxation parameter, p = 0.01, was found suitable to use after experimenting with different values. With p = 0.01, vorticity, ω, was calculated at the end of each iteration as follows:

$$\omega = p\omega^n + \omega^{n-1} (1-p) \ .$$

The turbulent solution for $R = 6.9 \times 10^6$ was thus obtained (Figure 3-10). In this solution it was observed that although the rest of the flow field had converged according to the convergence criterion of Equation (3.50), at the point half-way down and next to the base the value of vorticity was vanishingly small, and hence the above convergence criterion was not acceptable. Instead, the convergence criterion given by Equation (3.51) was used as discussed earlier in this chapter. The solution gave a

Logarithmic velocity profile,

$$u = \frac{u^*}{\kappa} \ln \frac{z+z_0}{z_0}$$

at the outlet

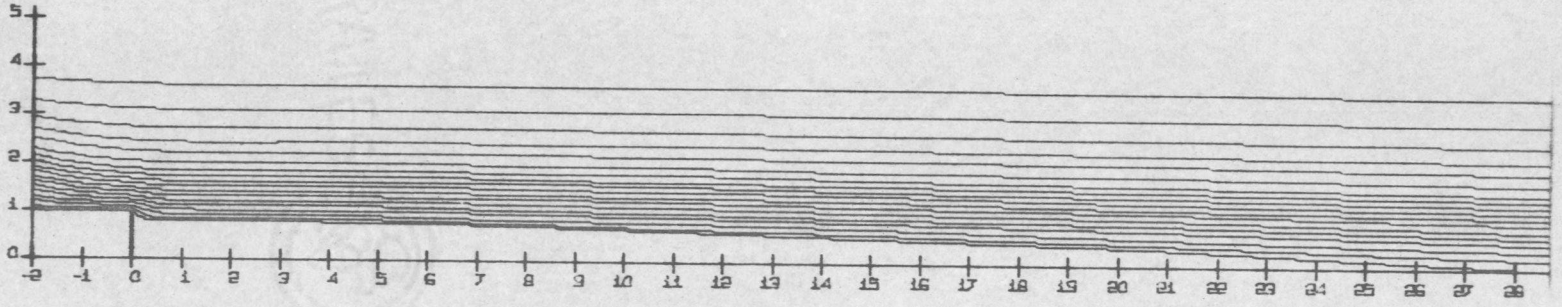


Figure 3-10. Streamlines over a back step in turbulent flow using the eddy viscosity model (Reynolds number = 6.9×10^6).

recirculation length which is too large. This is due to the eddy viscosity model being inadequate to correctly predict the turbulent recirculating flows. Thus a better model was sought.

Over-relaxation on the stream function was also used [38], but it did not seem to produce appreciable increase in convergence rate.

TKL model. In this model the values of the constants, C_{μ_∞}, C_{d_∞}, C_{s_∞}, and C_{b_∞}, as discussed earlier, must be determined by comparing the predicted results of the present model with the experimentally known results. Experimental results such as the length of the recirculation zone, the location of the dividing streamline, and the variation of turbulence intensity in the cavity zone, obtained for a back step in a wind tunnel for laboratory flows and for wind towers in atmospheric flows are the measured quantities of interest for comparison purposes.

Referring to the modified substitution formulae for k and ℓ, Equations (3.18a) and (3.18b), an increase in C_{d_∞} in the "dissipation" term reduces the turbulence kinetic energy, k, which in turn induces a decrease in the length scale, ℓ. Thus from Equation (3.9), it is observed that μ_{eff} decreases with an increase in C_{d_∞}. Similarly, an increase in C_{b_∞} appearing in the "eddy breaking" term and a decrease in C_{s_∞} in the "eddy stretching" term of the length-scale equation induce a decrease in μ_{eff}, which means the

turbulence is decreased. This can be interpreted as the tendency of the flow to behave more like a laminar flow. It has already been observed that the higher the R, the larger the bubble in laminar flow. Thus changes in C_{d_∞}, C_{s_∞}, and C_{b_∞} can be made to control the size of the recirculation bubble, and also the level of turbulence kinetic energy. The effect of C_{μ_∞}, on the other hand, is not so obvious. It would seem on a casual inspection of Equation (3.9) that an increase in C_{μ_∞} will increase μ_{eff} proportionally, but this is not the case. In the present problem the turbulent Reynolds number, $R_t >> 1$, in general, hence $C_\mu \approx C_{\mu_\infty}$. From Equations (3.43), (3.44), (3.48), and (3.49) it can be seen that on all the boundaries an increase in C_{μ_∞} results in a decrease in the value of k by the factor, $1/C_{\mu_\infty}^2$. Looking at Equation (3.18a), it is observed that k_p values at the interior nodes will not decrease as much as the k values at the boundaries because of the $k^{1/2}$ term in the denominator. From Equation (3.18b) ℓ also decreases slowly compared with the increase in C_{μ_∞}. Therefore, from Equation (3.9), although the value of μ_{eff} on the boundaries does not change with C_{μ_∞}, the value of μ_{eff} at the interior nodes will increase slowly; this has been found in the computation carried out in the present study.

Knowing approximately the influence of these constants on the solution, the next step is to vary them judiciously to achieve results in agreement with experimental data.

The boundary conditions on k at the outlet, Equations (3.44) and (3.44a), have both been investigated. The latter folating b.c. with the corresponding boundary condition for ψ at the outlet, Equation (3.23), did not seem to affect the rate of convergence over that of the former, and it yielded more parallel and horizontal streamlines; therefore, it was used for most of the results shown. The reason the gradient-type b.c. did not slacken the rate of convergence is that the outlet has been taken sufficiently far downstream so that the gradient effects are negligible. At the upper boundary a floating (gradient-type) b.c. on ℓ, $\frac{\partial \ell}{\partial z} = 0$, was tried, which worsened the rate of convergence, and hence was dropped in favor of the fixed b.c. there.

Initially, all the constants were set equal to unity. This gave an unstable solution with the stream function becoming negative over most of the flow field. Different values of the constants were tried, based on the discussion of their influence on the k and ℓ equations. Figures 3-11, 3-12, 3-13, 3-14, 3-15, and 3-16 show the stream function plots for various combinations of these constants. It can be seen that for the range of values of C_{μ_∞} chosen (0.05 to 1.0), the recirculation bubble does not change appreciably. On the other hand, the constant, C_{s_∞}, appearing in the "stretching" term for the length scale equation, has a very marked influence on the size of the bubble. For $C_{s_\infty} = 0.5$ the recirculation zone length is

Logarithmic velocity profile, $u = \frac{u^*}{\kappa} \ln \frac{z+z_0}{z_0}$,

specified at the outlet

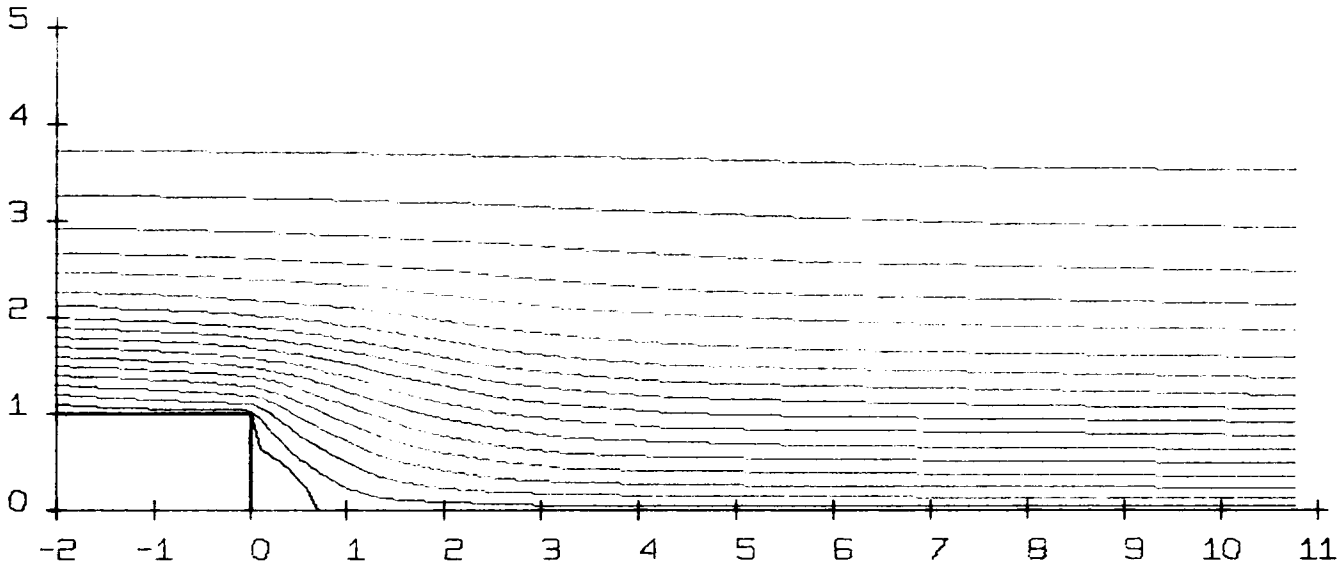


Figure 3-11. Streamlines over a back step in turbulent flow using the TKL model (Reynolds number = 6.9×10^6), $C_{\mu_\infty} = 1.0$, $C_{b_\infty} = C_{d_\infty} = 0.1$, $C_s = 1.0$.

Logarithmic velocity profile, $u = \frac{u^*}{\kappa} \ln \frac{z+z_0}{z_0}$,

specified at the outlet

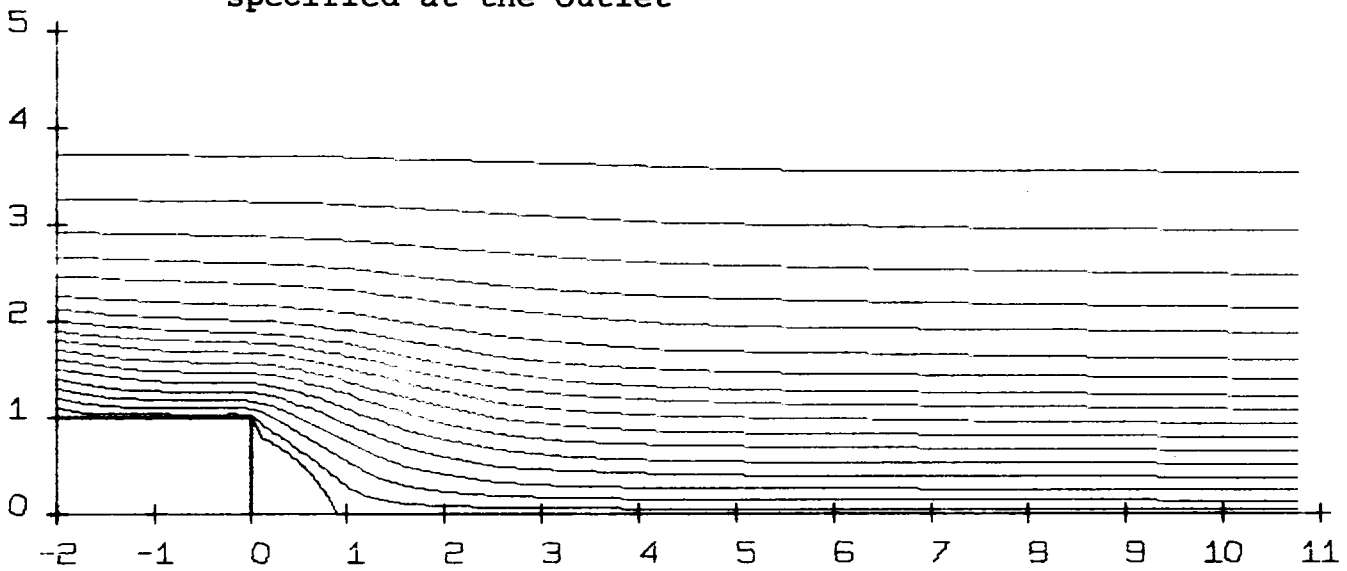


Figure 3-12. Streamlines over a back step in turbulent flow using the TKL model (Reynolds number = 6.9×10^6), $C_{b_\infty} = C_{d_\infty} = C_{\mu_\infty} = 0.1$, $C_s = 1.0$.

Logarithmic velocity profile, $u = \frac{u^*}{\kappa} \ln \frac{z+z_0}{z_0}$,

specified at the outlet

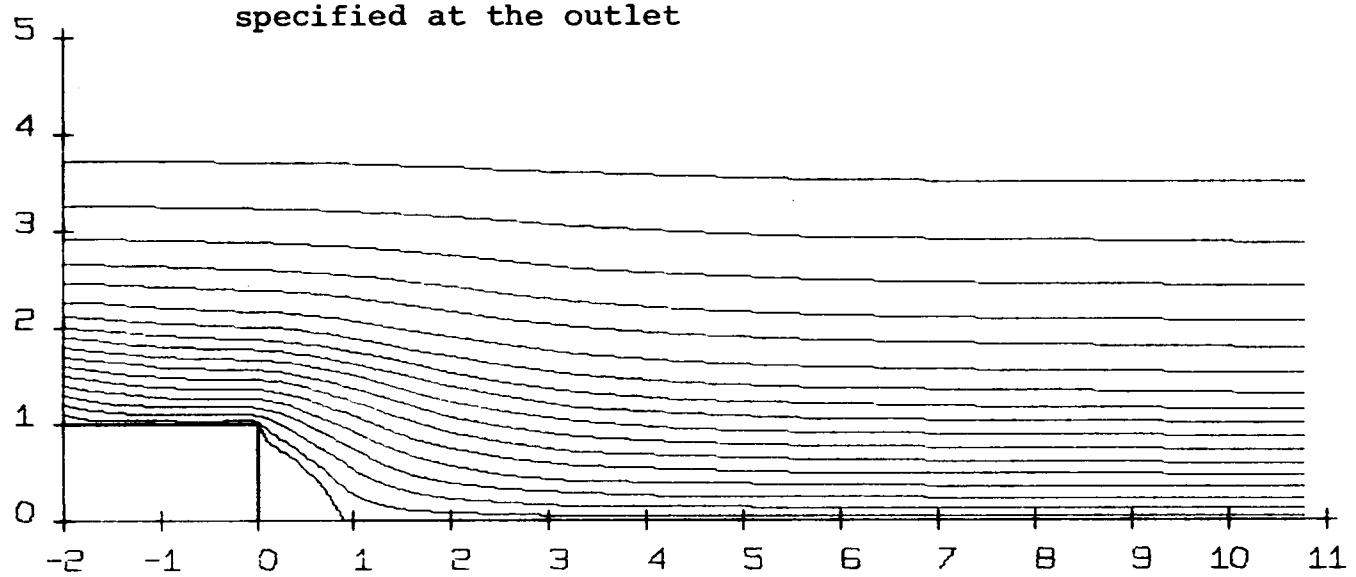


Figure 3-13. Streamlines over a back step in turbulent flow using the TKL model (Reynolds number = 6.9×10^6), $C_{\mu_\infty} = 0.08$, $C_{b_\infty} = C_{d_\infty} = 0.1$, $C_{s_\infty} = 1.0$.

Floating boundary conditions used at the outlet:

$$\frac{\partial^2 \psi}{\partial x^2} = 0 \text{ with } \frac{\partial \omega}{\partial x} = 0$$

$$\frac{\partial^2 k}{\partial x^2} = 0$$

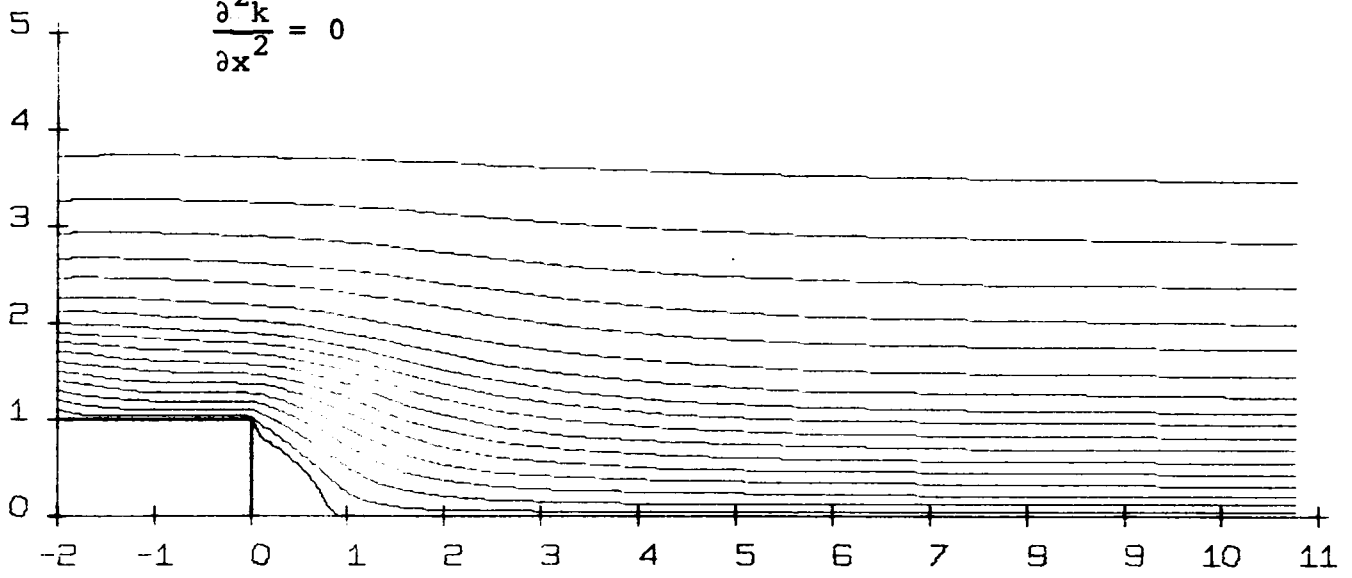


Figure 3-14. Streamlines over a back step in turbulent flow using the TKL model (Reynolds number = 6.9×10^6), $C_{\mu_\infty} = 0.05$, $C_{b_\infty} = C_{d_\infty} = 0.1$, $C_{s_\infty} = 1.0$.

Floating boundary conditions used at the outlet:

$$\frac{\partial^2 \psi}{\partial x^2} = 0 \text{ with } \frac{\partial \omega}{\partial x} = 0$$

$$\frac{\partial^2 k}{\partial x^2} = 0$$

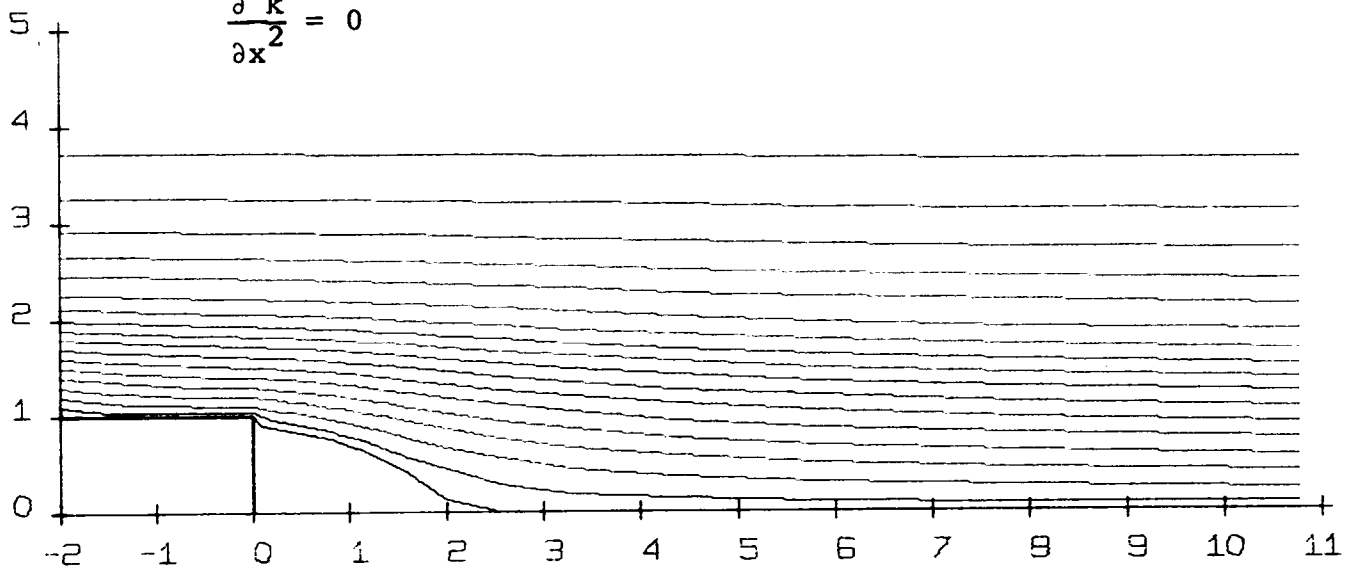


Figure 3-15. Streamlines over a back step in turbulent flow using the TKL model (Reynolds number = 6.9×10^6), $C_{\mu_\infty} = 0.1$, $C_{b_\infty} = C_{d_\infty} = 1.0$, $C_{s_\infty} = 0.5$.

Floating boundary conditions used at the outlet:

$$\frac{\partial^2 \psi}{\partial x^2} = 0 \text{ with } \frac{\partial \omega}{\partial x} = 0$$

$$\frac{\partial^2 k}{\partial x^2} = 0$$

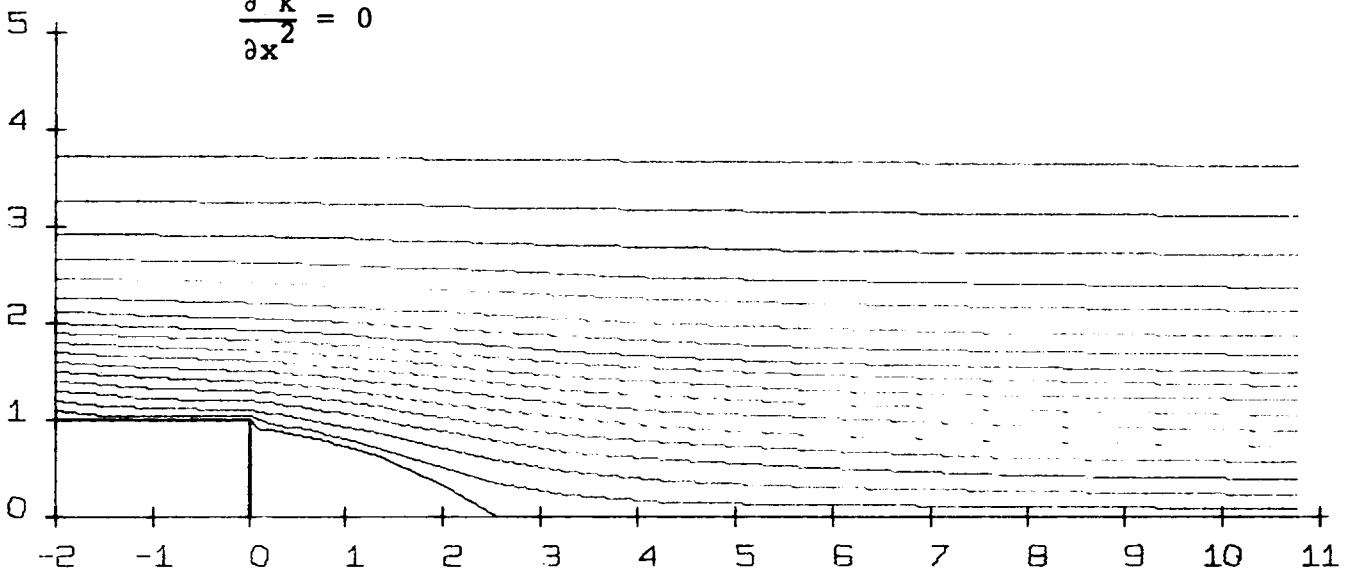


Figure 3-16. Streamlines over a back step in turbulent flow using the TKL model (Reynolds number = 6.9×10^6), $C_{\mu_\infty} = 0.1$, $C_{d_\infty} = C_{b_\infty} = 1.0$, $C_{s_\infty} = 0.4$.

about 2.1 step heights (Figure 3-15), for $C_{s_\infty} = 0.4$ the length is 2.5 step heights (Figure 3-16), and for $C_{s_\infty} = 0.35$ it increases to 4.2 step heights (Figure 3-17). In the computations carried out with lower values of C_{s_∞} than 0.35 it was observed that the boundary condition on k at the outlet (Equation (3.44a)) tended to impair the stability of the solution; and hence an alternative b.c., $\frac{\partial k}{\partial x} = 0$, was used at the outlet to investigate the effect of further decrease in C_{s_∞} on the solution, which appreciably increased the size of the recirculation zone downstream.

The value of 0.1 for C_{μ_∞} was found more suitable than the values of 0.08 and 0.05 as far as the rate of convergence of k and ℓ equations is concerned. Also, this value of C_{μ_∞} has been used by other authors in various turbulent flow situations (see the section on selection of constants). The value of 1.0 for C_{d_∞} and C_{b_∞} has been chosen out of the experience gained by carrying on the computational experiments. Thus with the following set of constants,

$$C_{\mu_\infty} = 0.1 \ ,$$

$$C_{s_\infty} = 0.35 \ ,$$

and

$$C_{b_\infty} = C_{d_\infty} = 1.0 \ ,$$

Floating boundary conditions used at the outlet:

$$\frac{\partial^2 \psi}{\partial x^2} = 0 \text{ with } \frac{\partial \omega}{\partial x} = 0$$

$$\frac{\partial^2 k}{\partial x^2} = 0$$

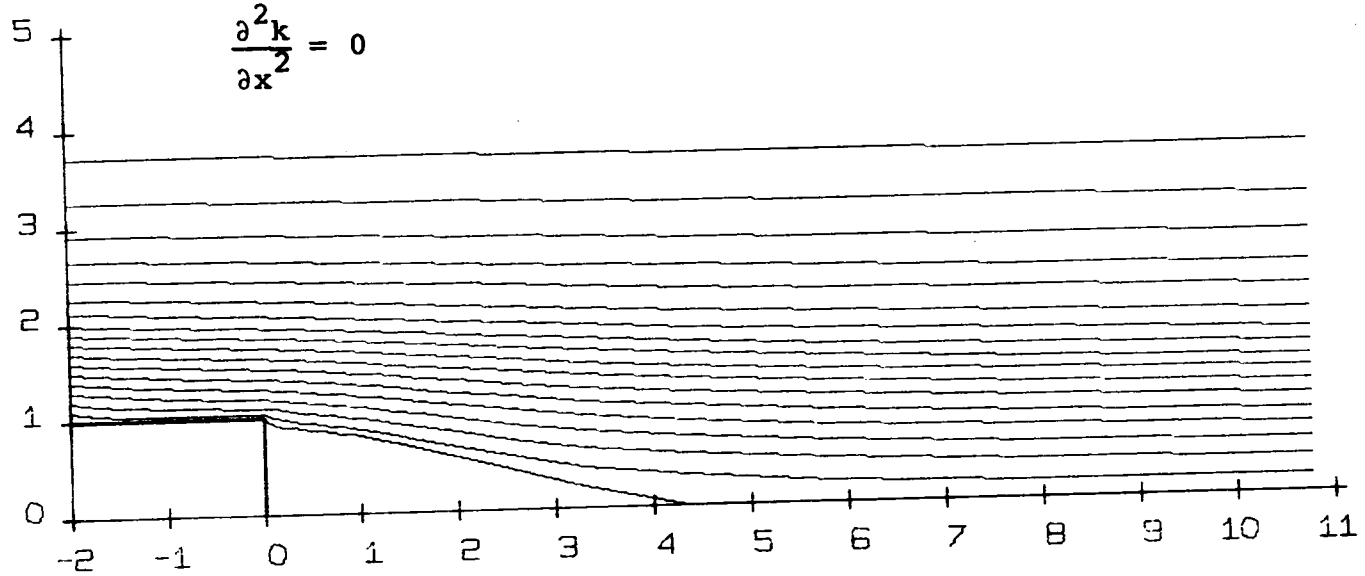


Figure 3-17. Streamlines over a back step in turbulent flow using the TKL model (Reynolds number = 6.9×10^6), $C_{\mu_\infty} = 0.1$, $C_{b_\infty} = C_{d_\infty} = 1.0$, $C_{s_\infty} = 0.35$.

the recirculating flow behind a back step has been well predicted; and they could be used for recirculating flows in different flow situations also. These asymptotic values for the functions, C_μ , C_s , C_d , and C_b , as $R_t \to \infty$, may be the "universal" constants for recirculating flows.

Conclusions and Summary

The present approach of solving the two-dimensional, incompressible turbulent Navier-Stokes equations in their steady form as applicable to atmospheric boundary layer flow has been shown to yield results for recirculating flows behind a backward-facing step in agreement with the experimental findings. Whereas for low and intermediate Reynolds numbers the eddy viscosity model of turbulence introduced into the governing equations has proved satisfactory, it has failed to predict the real flow situation at high Reynolds numbers when the magnitude of the velocity gradients in the flow field is correspondingly large. This is attributed to the fact that in recirculating flows the relation between stresses and the velocity gradients is unknown and more complicated than that assumed by the eddy viscosity model, and that where the velocity gradients vanish in recirculating flows, turbulence does not necessarily become zero. On the other hand, the TKL model of turbulence has been demonstrated to produce realistic results at high Reynolds numbers. The influence of the coefficients in the modeled source terms in the turbulence kinetic energy and turbulence

length scale equations on the predicted results has been computationally investigated, and a set of constants has thus been found for the problem under study.

It is felt that even more accurate predictions can be made with a three-equation model of turbulence in which the third dependent variable can be taken as the turbulent shear stress, $\rho\overline{u'v'}$.

For laminar flows the recirculation bubble was seen to increase in length with Reynolds number, which is physically true. The two contra-rotating eddies resulted in the solution, the corner eddy being the smaller one and rotating in the opposite sense to that of the larger one, the recirculation eddy.

CHAPTER IV

APPROXIMATE INTEGRAL TECHNIQUE

Empirical Information

The approximate integral method to predict the velocity profile in the recirculation region behind a rearward-facing step is based on the experimental information given in [4, 8, 10, 21]. The available data correspond to a "strong perturbation" (see Chapter I) and have been obtained from experiments conducted in wind tunnels at controlled turbulence levels. The results from these investigations correlate well, and the present mathematical model has been shown to reproduce the different features of the flow. In addition, a surface eddy viscosity distribution has resulted in the model which follows the empirically known surface pressure gradient distribution curve. Figure 4-1 shows the surface pressure coefficient plotted against the nondimensional distance, x/h [8], where h is the height of the step, u_r is the velocity in the undisturbed flow, δ_0 is the boundary layer thickness at the separation point, and x_R is the reattachment length. Figure 2-6, page 13, shows the location of the reattachment point (CR = x_R) and the location of the dividing streamline.

The error function profile which is known to approximate the fully developed shear layer profile in the

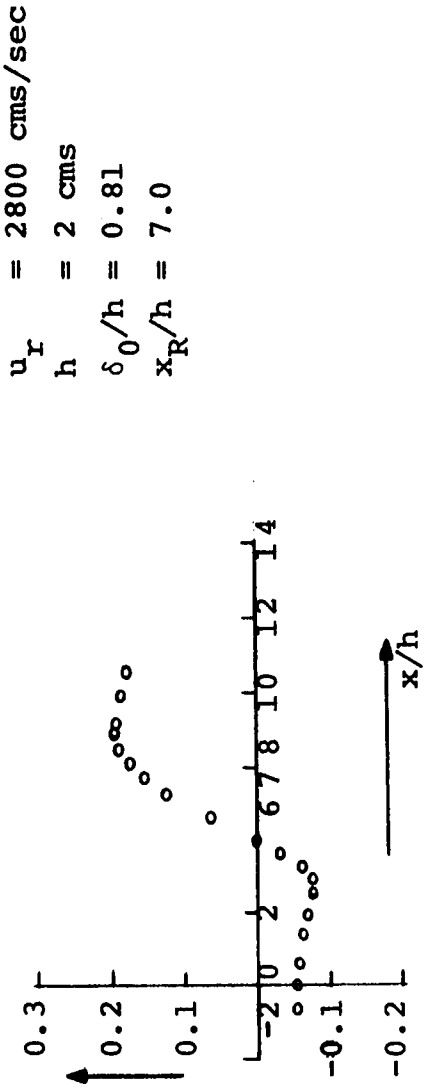


Figure 4-1. Variation of surface pressure coefficient behind a back step [8].

mixing region is given by

$$u_{erf} = \frac{u_e}{2}(1 + \text{erf}\ \frac{\sigma z}{x}) \ ,$$

where u_e is the undisturbed velocity which is asymptotically approached as the transverse coordinate, $\frac{\sigma z}{x} \to \infty$, and σ is the spreading rate parameter; also, $u_{erf} \to 0$ as $\frac{\sigma z}{x} \to -\infty$.

Governing Boundary Conditions for the Problem

To develop the governing equations consider a two-dimensional, steady, incompressible turbulent flow over a rearward-facing step, ABC (Figure 4-2). The separated flow is modeled as shown.

The initial boundary layer at the separation point, B, is considered to be represented by the simple power law profile,

$$\frac{u}{u_r} = (\frac{z}{\delta_0})^{1/n} \ ,$$

where u_r is a reference velocity, the index n = 7, and δ_0 is the initial boundary layer thickness. As the flow separates at B, a new shear layer originating there develops and spreads linearly downstream so that its upper boundary is represented by BB'. The dividing streamline BER coincides with Bx' up to some point, E (refer to Figures 2-3, page 10, 2-6, page 13, and 2-8, page 23). BER encloses the separation bubble in which there are two contra-rotating eddies,

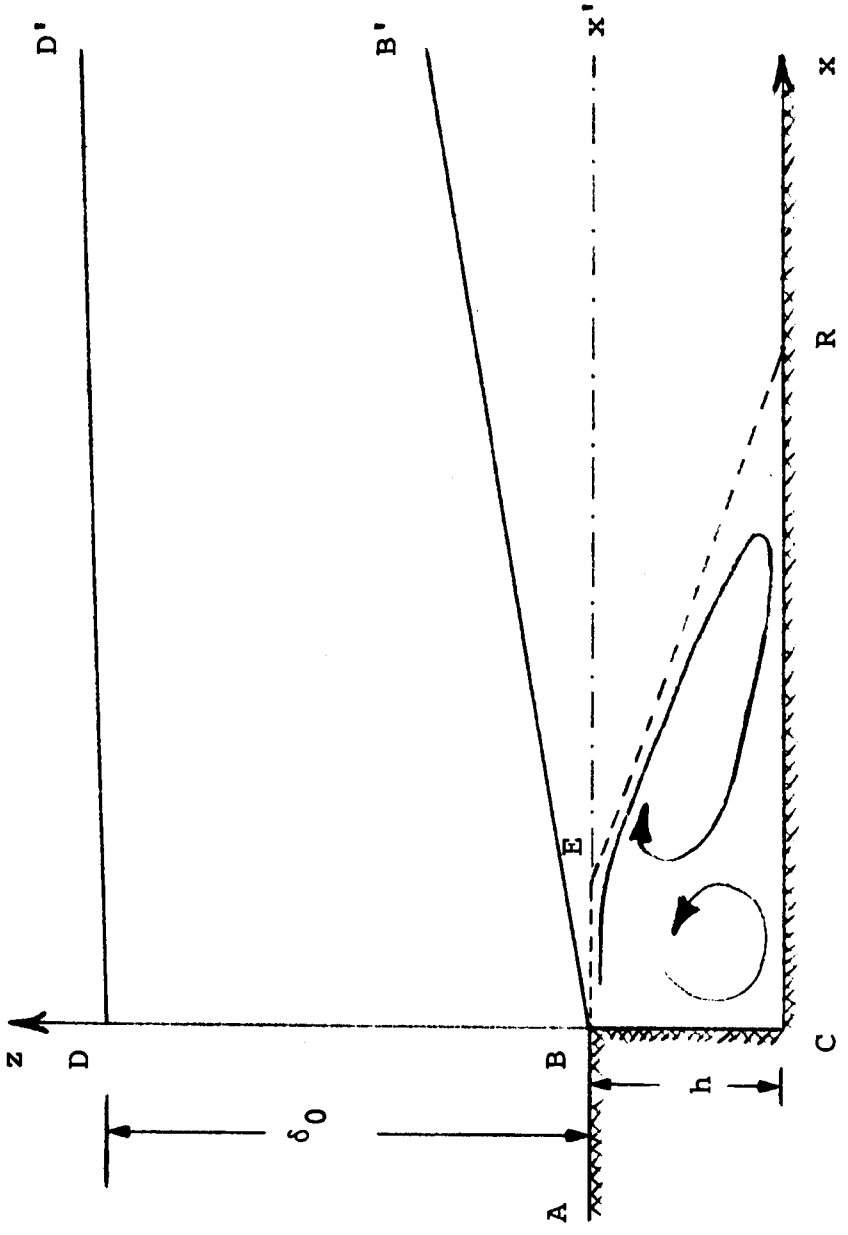


Figure 4-2. Model of separated flow over a back step.

the small corner eddy and the large recirculation eddy. DD' represents the boundary of the slowly growing initial boundary layer of almost constant height (see Figures 2-3, page 10, and 2-21, page 48). Camarata [21] has successfully correlated the error function profiles with the experimental turbulent free shear layer profiles (see Figure 2-24, page 52) by making use of the conservation of momentum principle. Also, the error function profile is shown to match with the outer boundary layer power law profile smoothly except for the upstream segment of the pre-asymptotic region where the slope-matching is discontinuous.

As a first approximation, Bx' is considered as the locus of the $u/u_e = 0.5$ points. Taking Cx and Cz as the abcissa and the ordinate of the Cartesian coordinate system, respectively, the velocity in the new shear layer will be represented by the error function profile.

$$u_{erf} = \frac{u_e}{2} \{1 + \text{erf} \frac{\sigma(z-h)}{x}\} .$$

Referring to Figure 4-3 (EF is a control surface with a unit depth perpendicular to the plane of paper), momentum is conserved between station x = 0 and any other x-station. Assuming that static pressure variations have negligible influence on the momentum balance and that the net momentum in the recirculating region is small, the momentum equation becomes

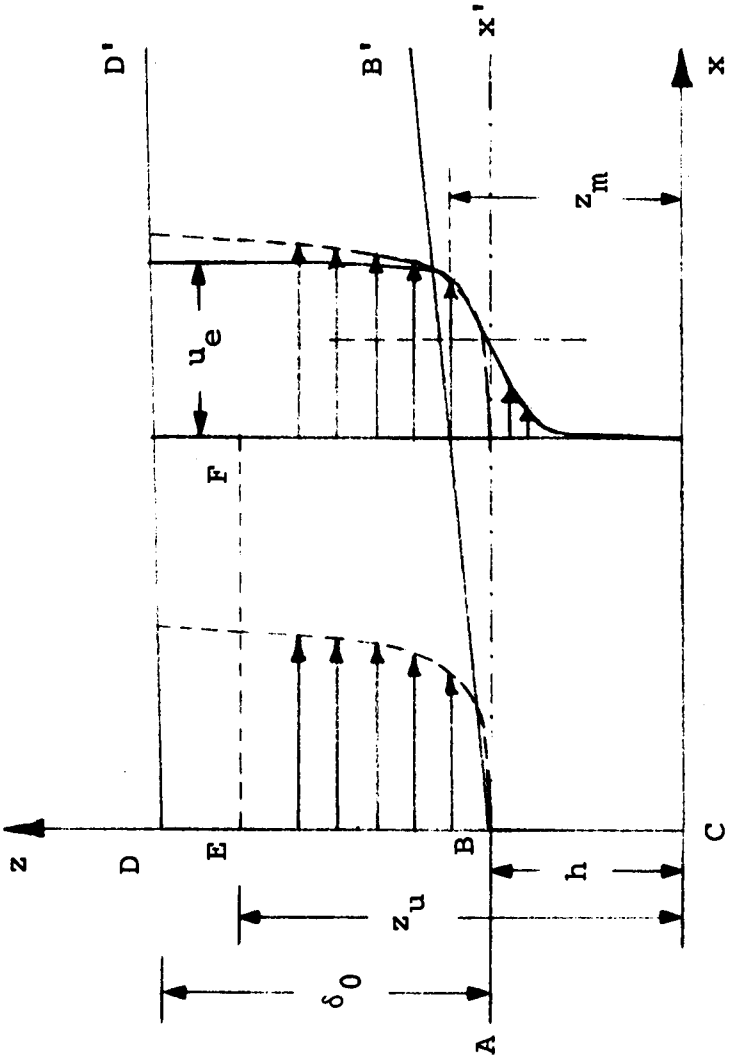


Figure 4-3. Illustration of the conservation of momentum principle.

$$\int_h^{z_u} u^2 dz \Big|_{x=0} = \int_0^{z_m} \left[\frac{u_e}{2}\left\{1 + \text{erf}\,\frac{\sigma(z-h)}{x}\right\}\right]^2 dz + \int_{z_m}^{z_u} u^2 dz \Big|_x$$

or

$$\left(\frac{u_r}{\delta_0^{1/7}}\right)^2 \int_h^{z_m} z^{2/7} dz = \frac{u_e^2}{4} \int_0^{z_m} \left\{1 + \text{erf}\,\frac{\sigma(z-h)}{x}\right\}^2 dz \quad . \quad (4.1)$$

For a continuous velocity profile,

$$u = u_{erf} \text{ , at } z = z_m \text{ ,}$$

or

$$u_r \left(\frac{z_m}{\delta_0}\right)^{1/7} = \frac{u_e}{2}\left\{1 + \text{erf}\,\frac{\sigma(z_m-h)}{x}\right\} \text{ ,}$$

or

$$u_e = \frac{2u_r \left(\frac{z_m}{\delta_0}\right)^{1/7}}{1 + \text{erf}\,\frac{\sigma(z_m-h)}{x}} \quad . \quad (4.2)$$

For a given σ, Equations (4.1) and (4.2) yield z_m and u_e. Thus the error function profile is completely specified.

Referring to Figure 4-4, it is assumed that the recirculation zone velocity profile is expressed by a fifth

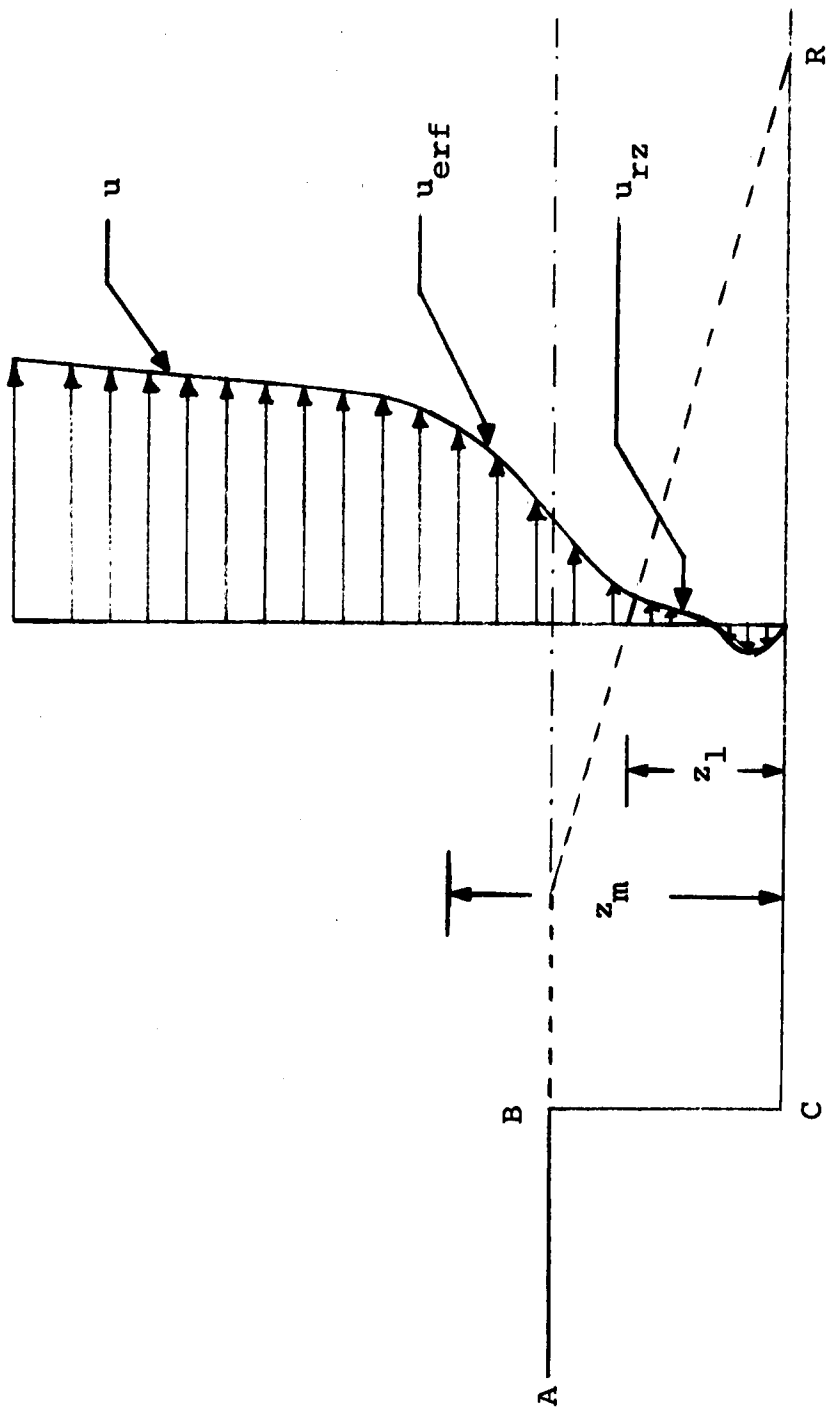


Figure 4-4. Velocity profiles in the recirculation zone, the new shear layer and the initial boundary layer.

degree polynomial as follows:

$$u_{rz} = e(x)z + f(x)z^2 + g(x)z^3 + h(x)z^4 + k(x)z^5 , \quad (4.3)$$

where for a given x the coefficients, e, f, g, h, and k, are constant. This profile should match with the new shear layer profile at a point, z_1 , on the dividing streamline. From experience it was found that for a continuous matching, the following three conditions should be satisfied at $z = z_1$:

1. $$u_{rz} = u_{erf} ,$$

2. $$\frac{\partial u_{rz}}{\partial z} = \frac{\partial u_{erf}}{\partial z} ,$$

3. $$\frac{\partial^2 u_{rz}}{\partial z^2} = \frac{\partial^2 u_{erf}}{\partial z^2} .$$

Mechanics of the flow in the recirculation region suggests that the equation of continuity should be satisfied there which provides the following condition:

4. $$\int_0^{z_1} u_{rz}\, dz = 0 .$$

Also, Equation (4.3) automatically satisfies the no-slip condition at the ground, $z = 0$.

Introducing the x-direction Navier-Stokes equation (Equation (3.2)) at the ground gives

$$\frac{1}{\rho}\frac{dp}{dx} = \frac{\partial}{\partial z}\left[\mu_{eff}\frac{\partial u_{rz}}{\partial z}\right] ,$$

where μ_{eff} is given by Equations (3.5), (3.6), and (3.7).

From Equation (4.3) at z = 0,

$$\frac{\partial u_{rz}}{\partial z} = e .$$

Therefore, at a given x-location, Equations (3.6) and (3.7) yield the following expression for eddy viscosity:

$$\nu_t = \kappa z_0^2 |e| , \tag{4.4}$$

and thus the momentum equation yields an additional condition in the following form:

$$5. \qquad \frac{1}{\rho}\frac{dp}{dx} = \{kz_0^2|e| + \nu\}\frac{\partial^2 u_{rz}}{\partial z^2} .$$

The aforementioned five conditions along with Equations (4.1) and (4.2) constitute the governing boundary conditions for the solution of the recirculation zone velocity profile, and upon simplification take the following form, respectively.

$$ez_1 + fz_1^2 + gz_1^3 + hz_1^4 + kz_1^5 = u_{erf}\Big|_{z_1} , \tag{4.5}$$

where

$$u_{erf}\Big|_{z_1} = \frac{u_e}{2}\{1 + \text{erf}\,\frac{\sigma(z_1-h)}{x}\}\ ,$$

$$e + 2fz_1 + 3gz_1^2 + 4hz_1^3 + 5kz_1^4 = \frac{\partial u_{erf}}{\partial z}\Big|_{z_1}\ , \qquad (4.6)$$

where

$$\frac{\partial u_{erf}}{\partial z}\Big|_{z_1} = \frac{u_e\sigma}{x\sqrt{\pi}}\,[\exp - \{\frac{\sigma(z_1-h)}{x}\}^2]\ ,$$

$$2f + 6gz_1 + 12hz_1^2 + 20kz_1^3 = \frac{\partial^2 u_{erf}}{\partial z^2}\Big|_{z_1}\ , \qquad (4.7)$$

where

$$\frac{\partial^2 u_{erf}}{\partial z^2}\Big|_{z_1} = -\frac{2\sigma^3(z_1-h)u_e}{x^3\sqrt{\pi}}\,[\exp - \{\frac{\sigma(z_1-h)}{x}\}^2]\ ,$$

$$30e + 20fz_1 + 15gz_1^2 + 12hz_1^3 + 10kz_1^4 = 0\ , \qquad (4.8)$$

$$f = \frac{u_r^2\,\frac{dC_p}{dx}}{4\{\nu_t+\nu\}}\ , \qquad (4.9)$$

where

$$\frac{dp}{dx} = \frac{1}{2}\,\rho u_r^2\,\frac{dC_p}{dx}\ .$$

Solution of Equations (4.5) through (4.8) leads to the expression for the coefficients of Equation (4.3) given in Table 4-1.

Normalized Form of the Equations to be Solved

Nondimensionalizing the velocities, u, u_{rz}, u_e, and u_{erf}, with respect to the reference velocity, u_r, and the distances, x, x_R, z, z_0, and δ_0, with respect to the step height, h, gives

$$x_{R_*} = \frac{x_R}{h}$$

$$u_* = \frac{u}{u_r} \quad ; \quad x_* = \frac{x}{h}$$

$$u_{rz_*} = \frac{u_{rz}}{u_r} \quad ; \quad z_* = \frac{z}{h}$$

$$u_{erf_*} = \frac{u_{erf}}{u_r} \quad ; \quad \delta_{0_*} = \frac{\delta_0}{h}$$

$$u_{e_*} = \frac{u_e}{u_r} \qquad z_{0_*} = \frac{z_0}{h} \; .$$

Therefore, Equations (4.1), (4.2), and (4.3), respectively, take the following forms:

$$\frac{1}{\delta_{0_*}^{2/7}} \int_1^{z_{m_*}} z_*^{2/7} dz_* = \frac{u_{e_*}^2}{4} \int_0^{z_{m_*}} \{1 + \text{erf} \frac{\sigma(z_*-1)}{x_*}\}^2 \, dz_* \; , \quad (4.1a)$$

TABLE 4-1

EXPRESSIONS FOR THE COEFFICIENTS OF EQUATION (4.3)

Coefficient	Expression for the Coefficient
k	$\dfrac{\frac{3}{4} z_1^2 \left.\dfrac{\partial^2 u_{erf}}{\partial z^2}\right\|_{z_1} - 6z_1 \left.\dfrac{\partial u_{erf}}{\partial z}\right\|_{z_1} + 2l u_{erf}\Big\|_{z_1} - \frac{1}{2} z_1^2 f}{z_1^5}$
h	$\dfrac{\frac{1}{3} z_1^2 \left.\dfrac{\partial^2 u_{erf}}{\partial z^2}\right\|_{z_1} - z_1 \left.\dfrac{\partial u_{erf}}{\partial z}\right\|_{z_1} + u_{erf}\Big\|_{z_1} + \frac{1}{3} z_1^2 f - \frac{8}{3} k z_1^5}{z_1^4}$
g	$\dfrac{\frac{1}{2} z_1^2 \left.\dfrac{\partial^2 u_{erf}}{\partial z^2}\right\|_{z_1} - z_1 \left.\dfrac{\partial u_{erf}}{\partial z}\right\|_{z_1} + u_{erf}\Big\|_{z_1} - 3hz_1^4 - 6kz_1^5}{z_1^3}$
e	$\dfrac{u_{erf}\Big\|_{z_1} - fz_1^2 - gz_1^3 - hz_1^4 - kz_1^5}{z_1}$

$$u_{e_*} = \frac{2(z_{m_*}/\delta_{0_*})^{1/7}}{1 + \text{erf}\,\dfrac{\sigma(z_{m_*}-1)}{x_*}} , \qquad (4.2a)$$

and

$$u_{rz_*} = e_*(x_*)z_* + f_*(x_*)z_*^2 + g_*(x_*)z_*^3 + h_*(x_*)z_*^4 + k_*(x_*)z_*^5 . \qquad (4.3a)$$

Equation (4.4) in the nondimensional form is

$$|e_*| = \nu_t/(\kappa z_{0_*}{}^2\, hu_r) . \qquad (4.4a)$$

Equation (4.9) becomes

$$f_* = \frac{hu_r dC_p/dx_*}{4(\nu_t+\nu)} . \qquad (4.9a)$$

The expressions for the coefficients, e_* , g_* , h_*, and k_* , remain the same as given in Table 4-1 except that all the quantities used therein are nondimensional.

Thus the problem is reduced to solving Equations (4.1a), (4.2a), and (4.3a) with Equations (4.4a) and (4.9a) and the coefficients of Table 4-1 in the nondimensional form.

Correlation of the Spreading Rate Parameter with the Experimental Data

The error function velocity profile which would approximate the free shear layer velocity profile is assumed

to tend to minus infinity in the negative z-direction [2, 3, 21, 23]. This imposes a restrictive condition on the selection of σ as the transverse coordinate in the error function velocity profile should approximately follow the relation,

$$\frac{\sigma(z_*-1)}{x_*} \geq -2 \ ,$$

at the ground, $z_* = 0$, and for a given x_* [$\text{erf}(-2) \approx -1.0$], that is,

$$\sigma \geq 2x_* \ . \qquad (4.10)$$

Also, as σ determines the rate of spreading of the new shear layer, the development of the line BB' in Figure 4-3, page 141, depends upon the value of σ chosen. Figure 2-3, page 10, shows that the upper boundary of the new shear layer has a dip near the region of sudden pressure rise (Figure 4-1, page 137), that is, the region of rapid distortion as defined by Bradshaw and Wong [4]. The line BB' thus has a downward-going trend until the reattachment point, when the effects of the distortion die out; and it rises again into the initial boundary layer downstream.

It may be noted that a smaller σ gives a larger spreading, and vice versa. Thus either a constant value or a very slowly increasing or decreasing value of σ may be used up to the region of maximum pressure rise subject to the condition of Equation (4.10). Beyond this point, an

increasing value of σ subject to the condition of Equation (4.10) should be used. In Chapter II it has been discussed that varying values of σ have been used for the case of back steps in incompressible flow (range of variation from 9 to 15 for σ).

Solution Procedure

With this information available for the spreading rate parameter, σ, one can proceed to solve the system of the integral equation (Equation (4.1a)) and Equations (4.2a), (4.3a), (4.4a), (4.9a), and those given in Table 4-1, page 148, in the nondimensional form.

For a given σ, Equation (4.1a) with Equation (4.2a) is solved using Simpson's fifth order quadrature formula for integration. The value of z_{m_*} is calculated iteratively. The solution of these two equations gives z_{m_*} and u_{e_*}, and hence the error function velocity profile is completely known. The coefficients in Table 4-1 in the nondimensional form are calculated next and then the recirculation zone velocity profile is determined by Equation (4.3a).

The coefficient, e_*, as calculated from Table 4-1 is compared with Equation (4.4a) as follows: Denoting e_* from Table 4-1 by E1, for compatibility the following should be true:

$$|E1| - \frac{\nu_t}{(\kappa z_{0_*}^2 \, h \, u_r)} = 0 \; . \qquad (4.11)$$

The nonlinear equation (Equation (4.11)) is a monotonically decreasing function of ν_t , and it can be solved for ν_t iteratively. A simple secant method is sufficient to find the zero of this function. Thus the solution results in the value of the eddy viscosity.

The computer code which has been developed to solve the present problem is explained by means of a flow chart as shown in the appendix.

Comments on Convergence, Accuracy, and Economy of the Integral Method

The approximate technique as discussed above is a very fast method of predicting the velocity profiles and the surface eddy viscosity distribution in the recirculation zone behind a back step. The average time for a single x-station computation on an IBM 360/65 computer is about two seconds.

Equation (4.1a) has two solutions for z_{m_*} , as shown in Figure 2-22, page 49. The matching is discontinuous at the lower value of z_{m_*} ; but at the higher value, which is taken as the true solution, it is smooth. However, in the region close to the base of the step, the matching is not smooth (see Figure 4-5). This has been experimentally verified [21], and the reason could be ascribed to the

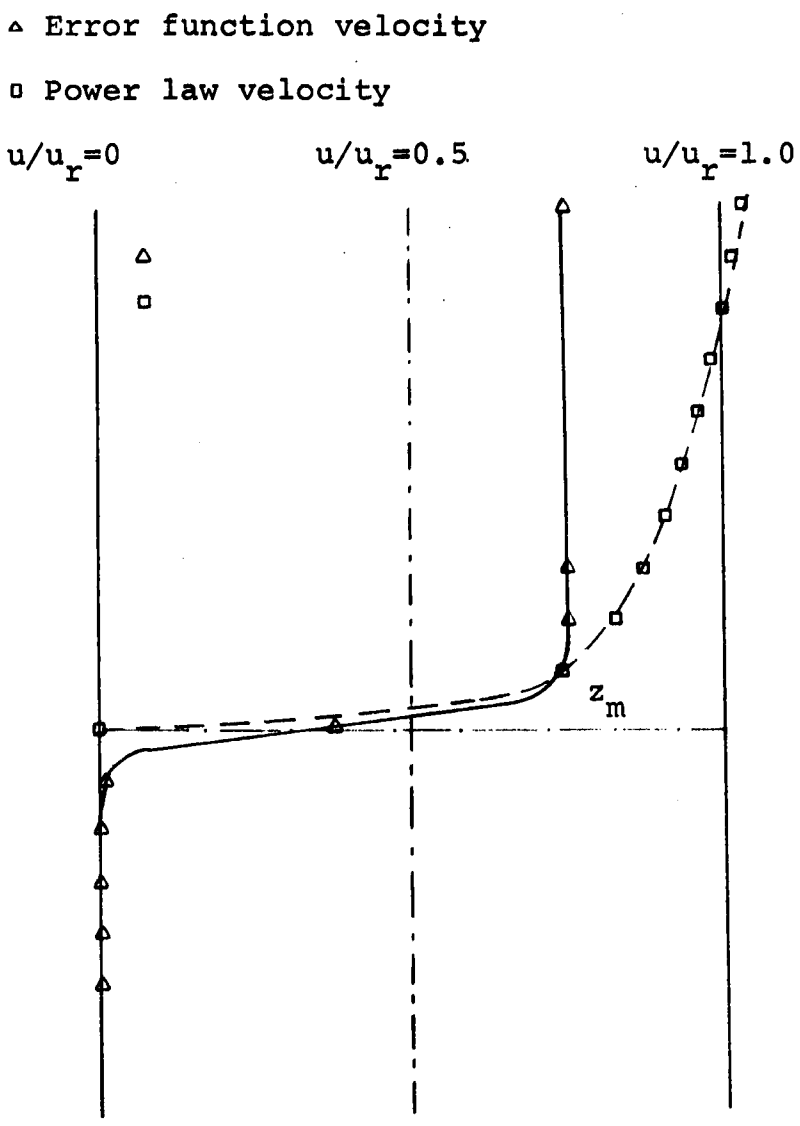


Figure 4-5. Illustration of the matching of the error function and power law profiles in the base region.

interference from the base. Farther downstream, the matching is smooth. Due to the non-uniqueness of the solution for Equation (4.1a) no standard iteration technique, for example, Newton's method, was used; and hence the solutions were determined by regularly incrementing the z_* value from 1.0 upwards. The incremental value chosen was such that the magnitude of the function given by Equation (4.1a) at the root, z_{m_*}, was less than 0.001. This is a satisfactory convergence criterion as is evident from the smooth matching between the error function and the power law profiles shown in Figure 4-6. The convergence of the solution of Equation (4.11) was based on the relative error criterion,

$$\left| \frac{\nu_{t_2} - \nu_{t_1}}{\nu_{t_1}} \right| \leq 0.001 \ ,$$

where ν_{t_1} and ν_{t_2} are the two successive eddy viscosity values at any stage in the iteration process.

Discussion of Results

Referring to Figure 4-7(a) and (b), various values of σ were used in the computation discussed in the section on its correlation with the experimental data. An eddy viscosity distribution along the surface was faired as shown in (b), which follows the magnitude of the surface pressure gradient distribution shown in (a). A constant value of σ equal to 8 was used up to $x_* = 4.0$, and $\sigma = 2x_*$ was used up

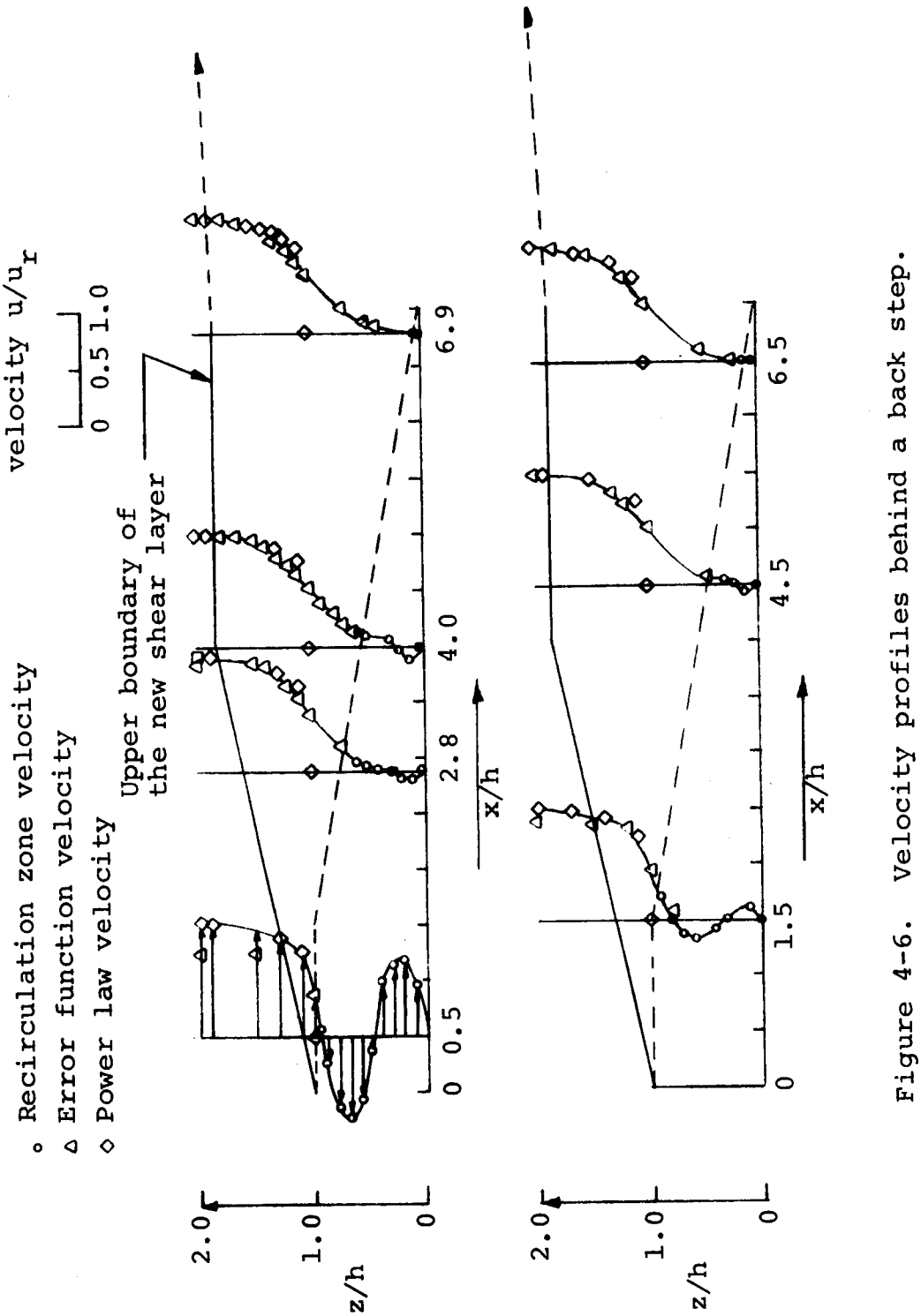
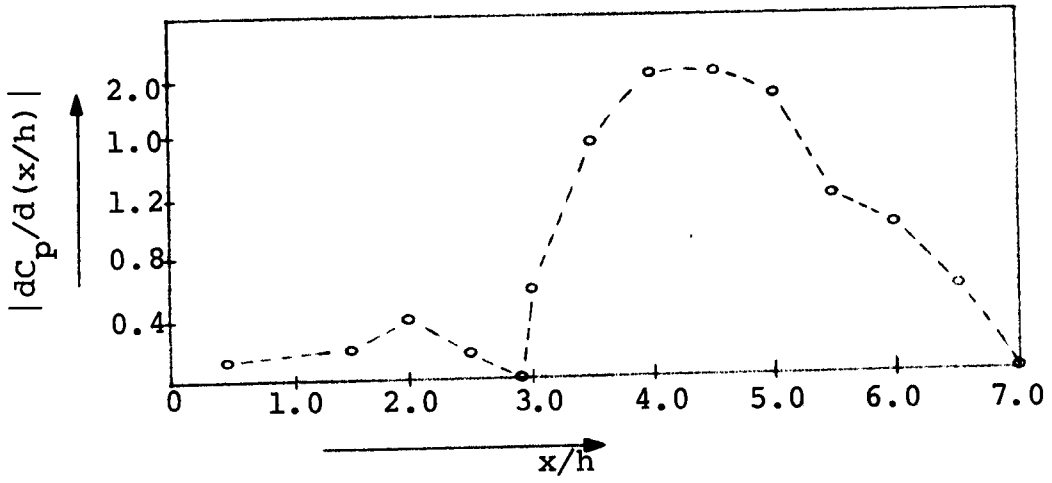


Figure 4-6. Velocity profiles behind a back step.

(a) Magnitude of surface pressure gradient distribution



(b) Surface eddy viscosity distribution

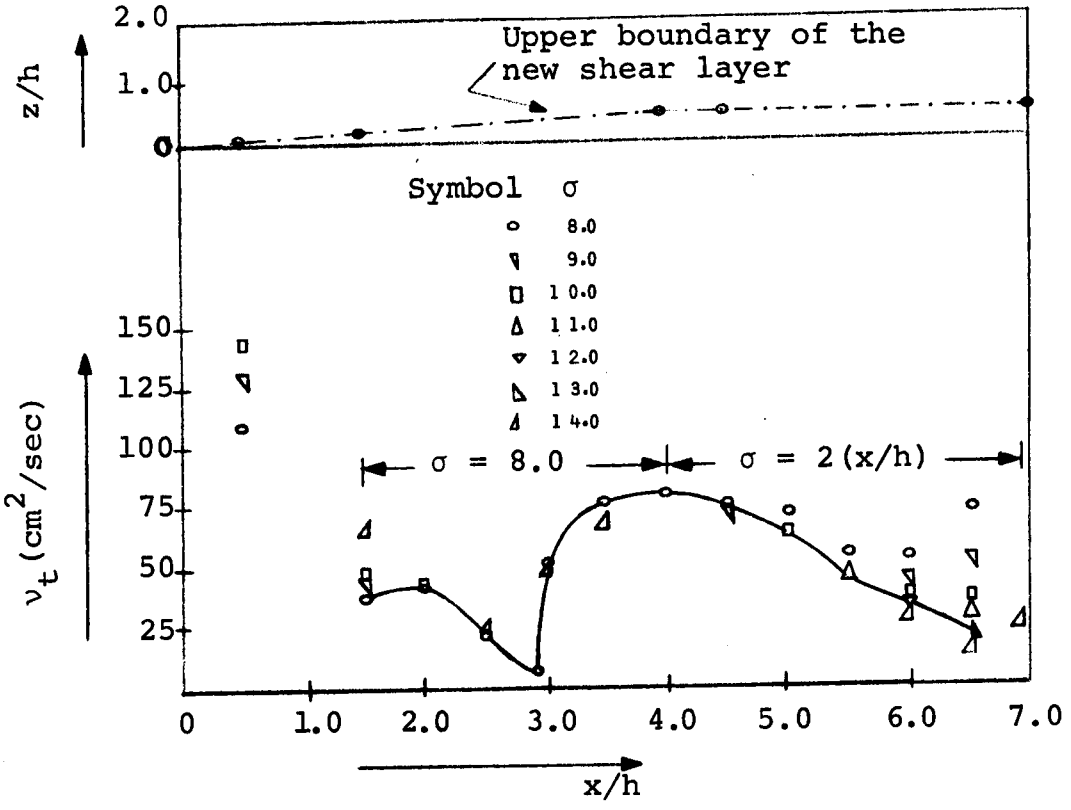


Figure 4-7. Variation of surface pressure gradient and surface eddy viscosity behind a back step.

to $x_* = 6.9$. This variation of σ gives the spreading in the region of rapid distortion as shown in Figure 2-3, page 10. Also, the eddy viscosity, ν_t, follows

$$\left|\frac{dC_p}{dx_*}\right|$$

very realistically. The peak values of ν_t in the region of

$$\left|\frac{dC_p}{dx_*}\right|_{max},$$

defined as the reattachment zone, confirms the high turbulence and hence the high heat transfer rates in this zone. Near the base and very near the reattachment point, however, ν_t does not follow the magnitude of the pressure gradient, which are the regions where no measurements of velocity or of turbulence intensity have been made (see Figure 2-6, page 13), and in which regions the measurements of shear stress are scanty and unreliable. However, it is well documented that the surface shear stress and hence the surface eddy viscosity should increase after the reattachment point. If the reattachment point is located upstream of the point where

$$\frac{dC_p}{dx_*} = 0,$$

then the eddy viscosity distribution as shown in Figure 4-7 is quite realistic. However, due to the lack of experimental evidence, no improvements in the present model have been suggested as far as the eddy viscosity distribution is concerned.

The velocity profiles are shown plotted at various x-stations in Figure 4-6, page 155. The recirculation zone velocity profile matches very smoothly with the error function velocity profile at the dividing streamline. In the region of the negative surface pressure gradient, the presence of the corner eddy with a reversed recirculating flow is confirmed. The large magnitude of the velocity in this region alludes to the presence of a very strong corner eddy near the base. The magnitude of the reversed velocity in the region of the recirculation eddy is of the order of $0.1\ u_r$ (Figure 4-6), and it does not exceed $0.2\ u_r$ at any station. This is in agreement with the experimental results of Bradshaw and Wong [4].

At the dividing streamline, the turbulent shear stress, which is also the maximum shear stress in the shear layer, is given by

$$\tau_t = \rho\kappa(z_{l_*}+z_{0_*})^2 \left\{\frac{\partial u_*}{\partial z_*}\right\}^2_{z_{l_*}} u_r^2 . \qquad (4.12)$$

Nondimensionalizing τ_t with respect to ρu_r^2 ,

$$\tau_{t_*} = \kappa(z_{1_*}+z_{0_*})^2 \left\{\frac{\partial u_*}{\partial z_*}\right\}^2_{z_{1_*}} . \qquad (4.12a)$$

The normalized shear stress, τ_{t_*} , has been plotted against x_* in Figure 4-8. Although the validity of the momentum transfer theory and hence the Prandtl mixing-length theorem (Equation (4.12)) is not quite valid in nonequilibrium layers, especially in the recirculation zone, on comparing Figure 2-7, page 16, and Figure 2-12, page 27, with Figure 4-8, it can be seen that the general trend in the value of shear stress along the dividing streamline to decrease downstream towards the reattachment point, as exhibited by Figure 4-8, is physically correct.

Suggestions to Improve the Model

The fact that the static pressure behind a bluff plate (see Figure 2-13, page 28) varies in the transverse direction entails an improvement in the application of the z-direction momentum theorem in the case of the back step behind which the static pressure variations at different x-stations follow closely those behind a bluff plate. Thus Equation (4.1) will be modified as follows:

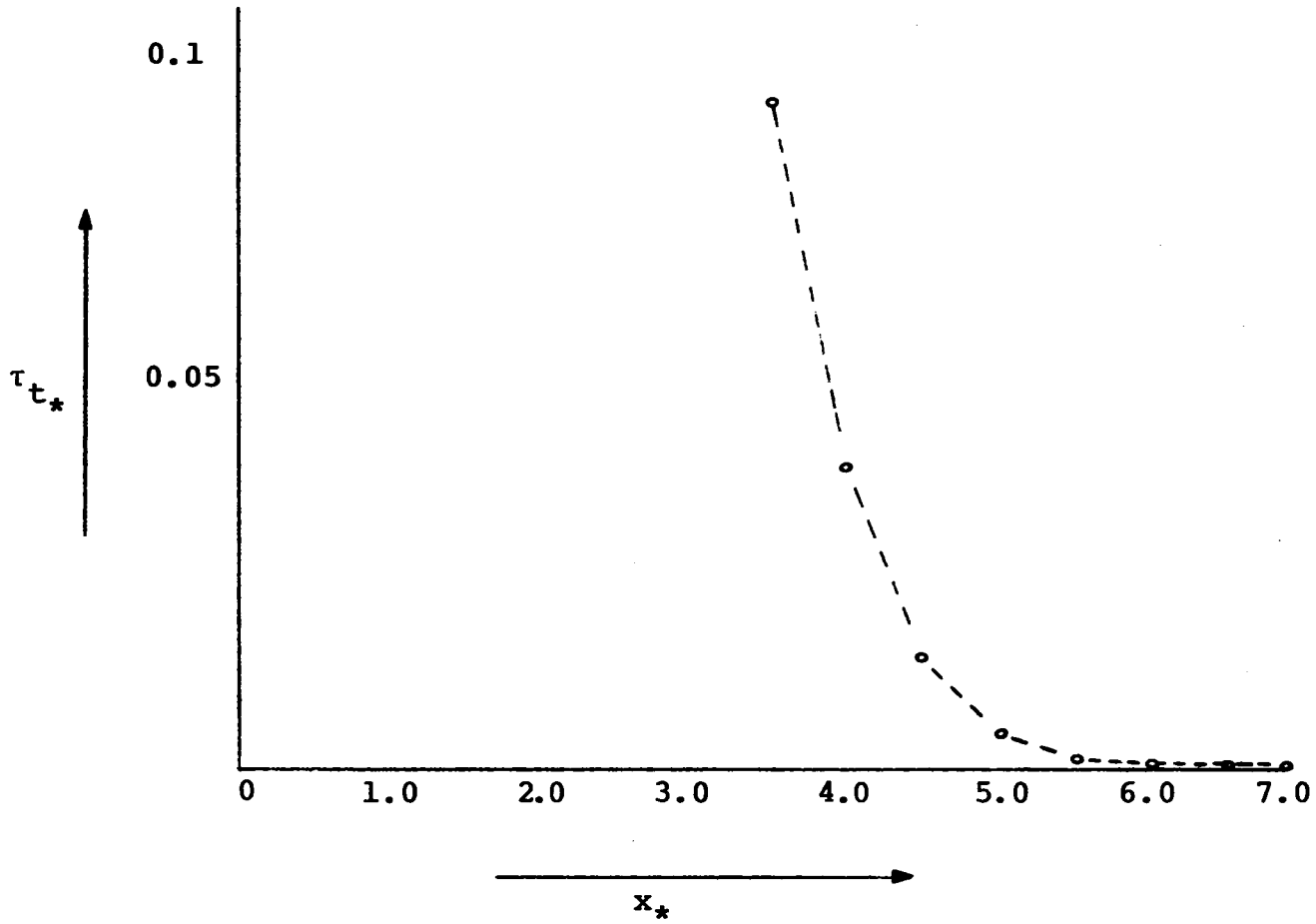


Figure 4-8. Variation of the nondimensional maximum shear stress in the shear layer with the nondimensional distance along the ground.

$$\left(\frac{u_r}{\delta_0}\right)^2 \int_h^{z_m} z^2 dz + \frac{p_r}{\rho}(z_u - h)$$

$$+ \frac{p_b}{\rho} h = \frac{u_e^2}{4} \int_0^{z_m} \left\{1 + \text{erf}\, \frac{\sigma(z-h)}{x}\right\}^2 dz$$

$$+ \frac{1}{\rho} \int_0^{z_u} p\, dz \,, \qquad (4.1b)$$

where p_b and p_r are the base and reference (undisturbed) pressures, respectively.

Solution of the problem under study is strongly dependent upon the value of σ chosen; and therefore, the development of line BB' in Figure 4-3, page 141 (spreading of the upper shear layer), to approximate that shown in Figure 2-3, page 10, would require a different distribution of σ values when Equation (4.1b) is used in place of Equation (4.1), hence giving a more realistic surface eddy viscosity distribution. Equation (4.1b) also takes into account the interfering effect of the base for x-stations close to it, and thus velocity profiles in the region of the corner eddy could be computed to a greater reliability. Also, near the reattachment point where the transverse pressure gradient close to the surface is appreciable, Equation (4.1b) would yield more meaningful results.

BIBLIOGRAPHY

BIBLIOGRAPHY

1. von Doenhoff, A. E. "A Preliminary Investigation of Boundary Layer Transition Along a Flat Plate with Adverse Pressure Gradient," National Advisory Committee for Aeronautics TN 639, Washington, D. C., 1938.

2. Frost, Walter. "Review of Data and Prediction Techniques for Wind Profiles Around Man-made Surface Obstructions." Report prepared under the NASA Marshall Space Flight Center Contract No. NAS8-27387 by The University of Tennessee Space Institute, Tullahoma, Tennessee, May, 1973.

3. Chang, Paul K. Separation of Flow. Oxford: Pergamon Press, Inc., 1970.

4. Bradshaw, P., and F. Y. F. Wong. "The Turbulent Boundary Layer Behind a Separated Region," Journal of Fluid Mechanics, Part 1, 52:113-135, March, 1972.

5. Good, M. C., and P. N. Joubert. "The Form Drag of Two-Dimensional Bluff-Plates Immersed in Turbulent Boundary Layers," Journal of Fluid Mechanics, 31:547-582, June, 1968.

6. Chang, S. C. "Velocity Distributions in the Separated Flows Behind a Wedge Shaped Hill." Unpublished Master's thesis, Colorado State University, Denver, 1966.

7. Arie, M., and H. Rouse. "Experiments on Two-Dimensional Flow Over a Normal Wall," Journal of Fluid Mechanics, 1:24-141, November, 1956.

8. Tani, I., M. Iuchi, and H. Komoda. "Experimental Investigation of Flow Separation Associated with a Step or a Groove," Aeronautical Research Institute Report No. 364, University of Tokyo, April, 1961.

9. Honji, H. "The Starting Flow Down a Step," Journal of Fluid Mechanics, Part 2, 69:229-240, 1975.

10. Mueller, Thomas J., and James M. Robertson. "A Study of the Mean Motion and Turbulence Downstream of a Roughness Element," Developments in Theoretical and Applied Mechanics. New York: Plenum Press, 1963. Pp. 326-340.

11. Charwat, A. F., J. N. Roos, F. C. Dewey, Jr., and J. A. Hitz. "An Investigation of Separated Flows," Journal of the Aerospace Sciences, 28 (Number 6): 457-470, June, 1961; 28 (Number 7): 513-527, July, 1961.

12. Wauschkuhn, P., and V. Vasanta Ram. "The Turbulent Boundary Layer Behind a Separated Region," The University of Bochum Report No. 32, West Germany, 1974.

13. Coles, D. D. "The Young Person's Guide to the Data," Proceedings of the 1968 AFOSR-IFP-Standard Conference on Computation of Turbulent Boundary Layers, S. J. Kline and others, editors. Vol. II. Stanford, California: Stanford University Press, 1969. Pp. 1-19.

14. Townsend, A. A. "Equilibrium Layers and Wall Turbulence," American Institute of Aeronautics and Astronautics Journal, 11:97-120, December, 1961.

15. Wu, J. M., C. H. Chen, and T. H. Moulden. "Experimental Study of Compressible Turbulent Boundary Layer Separation as Influenced by Upstream Disturbances." American Institute of Aeronautics and Astronautics Paper No. 75-830, presented at AIAA Fluid and Plasma Dynamics Conference, Hartford, Connecticut, June 16-18, 1975.

16. Mueller, T. J. "On Separation, Reattachment and Redevelopment of Turbulent Boundary Layers." Ph.D. dissertation, University of Illinois at Urbana-Champaign, Urbana, 1961.

17. Tanner, M. "Theoretical Prediction of Base Pressure for Steady Base Flow," Progress in Aerospace Sciences, D. Küchemann, editor. Vol. 14. New York: Pergamon Press, Inc., 1973. Pp. 177-225.

18. Fage, A., and F. C. Johansen. "The Structure of Vortex Sheets," Phil. Mag. 5, Series 7:417-441, 1928; Aeronautical Research Council Reports and Memoranda No. 1123, London, England, 1927.

19. Korst, H. H., and W. L. Chow. "On the Correlation of Analytical and Experimental Free Shear Layer Similarity Profiles by Spread Rate Parameters." The American Society of Mechanical Engineers Paper No. 70-WA/FE-12, presented at the ASME Winter Annual Meeting, New York, November 29-December 3, 1970.

20. Elassar, R. J., and P. P. Pandolfini. "An Examination of Eddy Viscosity Models for Turbulent Free Shear Flows." The American Society of Mechanical Engineers Paper No. 71-FE-17, presented at ASME Fluids Engineering Conference, Pittsburgh, Pennsylvania, May 9-12, 1971.

21. Camarata, F. J. "A Method for Determining the Effect of Initial Boundary Layer on Turbulent Free Shear Layer Velocity Profiles," Journal of Basic Engineering, 713-715, December, 1971.

22. Schlichting, H. Boundary-Layer Theory. New York: McGraw-Hill Book Company, Inc., 1968.

23. Plate, E. J. Aerodynamic Characteristics of Atmospheric Boundary Layers. United States Atomic Energy Commission, Oak Ridge, Tennessee: Division of Technical Information Extension 25465, 1971.

24. Nash, J. F. "The Effect of an Initial Boundary Layer on the Development of a Free Shear Layer," National Physical Laboratory Aero-Report 1019, Great Britain, June, 1962.

25. Nash, J. F. "An Analysis of Two-Dimensional Turbulent Base Flow, Including the Effect of the Approaching Boundary Layer," Aeronautical Research Council Reports and Memoranda No. 3344, London, England, 1963.

26. Yen, K. T. "On the Indeterminateness of the Boundary Conditions for the Mixing of Two Parallel Streams." The American Society of Mechanical Engineers Paper No. 59-A-68, presented at the ASME Annual Meeting, Atlantic City, New Jersey, November 29-December 4, 1959.

27. Kubota, T., and C. Forbes Dewey, Jr. "Momentum Integral Methods for the Laminar Free Shear Layers." Report prepared under the United States Army Research Office and the Advanced Research Projects Agency Contract No. DA-31-124-ARO(D)-33 by the California Institute of Technology, Pasadena, January, 1964.

28. Chapman, D. R. "Laminar Mixing of a Compressible Fluid," National Advisory Committee for Aeronautics Report 958, Washington, D. C., 1950.

29. Walz, A. "Anwendung des Energiesatzes von Wieghardt auf einparametrige Geschwindigkeitsprofile in laminaren Grenzschichten," Ingenieur-Archiv, 16:243-248, 1948.

30. Tani, I. "On the Approximate Solution of the Laminar Boundary Layer Equations," Journal of the Aeronautical Sciences, 21:487-495, 1954.

31. Lees, L., and B. L. Reeves. "Some Remarks on Integral Moment Methods for Laminar Boundary Layers with Application to Separation and Reattachment." Report prepared under AFOSR 1920 Contract No. AF49(638)-916 by the Graduate Aeronautical Laboratories of the California Institute of Technology, Pasadena, December, 1961.

32. Glick, H. S. "Modified Crocco-Lees Mixing Theory for Supersonic Separated and Reattaching Flows," Graduate Aeronautical Laboratories of the California Institute of Technology Hypersonic Research Project Memorandum No. 53, Pasadena, May, 1960.

33. Mueller, T. J., H. H. Korst, and W. L. Chow. "On the Separation, Reattachment, and Redevelopment of Incompressible Turbulent Shear Flow," Transactions of the ASME Journal of Basic Engineering, 86 (Number 2): 221-226, 1964.

34. Uchida, S., and K. Watanabe. "On a Similar Solution of Curved Half Jet," Proceedings of the 11th International Congress of Applied Mechanics, Henry Görtler, editor. Berlin: Springer-Verlag, 1966. Pp. 677-688.

35. Yen, K. T., and K. Toba. "A Theory of the Two-Dimensional Boundary Layer Over a Curved Surface," Journal of the Aeronautical Sciences, 28 (Number 11):877-884, 1961.

36. Frost, Walter, J. R. Maus, and W. R. Simpson. "A Boundary Layer Approach to the Analysis of Atmospheric Motion Over a Surface Obstruction." Report prepared under NASA Contract No. CR-2182 by The University of Tennessee Space Institute, Tullahoma, Tennessee, January, 1973.

37. Launder, B. E., and D. B. Spalding. Mathematical Models of Turbulence. New York: Academic Press, Inc., 1972.

38. Gosman, A. D., W. M. Pun, A. K. Runchal, D. B. Spalding, and M. Wolfshtein. Heat and Mass Transfer in Recirculating Flows. New York: Academic Press, Inc., 1973.

39. Rotta, J. C. "Statistische Theorie nichthomogener Turbulenz," Zeitschrift für Physik, 129:547-572, and 131:51-77, 1951. Also English translation as Imperial College Mechanical Engineering Department Reports TWF/TN/38 and TWF/TN/39, London, 1951.

40. Orszag, S. A. "Numerical Simulation of Turbulent Flows." Lecture notes at the Short Course on Fundamentals and Applications of Turbulence, The University of Tennessee Space Institute, Tullahoma, Tennessee, April, 1975.

41. Roache, P. J., and T. J. Mueller. "Numerical Solutions of Compressible and Incompressible Laminar Separated Flows." American Institute of Aeronautics and Astronautics Paper No. 68-741, presented at AIAA Fluid and Plasma Dynamics Conference, Los Angeles, California, June 24-26, 1968.

42. Roache, P. J. Computational Fluid Dynamics. Albuquerque, New Mexico: Hermosa Publishers, 1972.

43. Woods, L. C. "A Note on the Numerical Solution of Fourth Order Differential Equations," Aeronautical Quarterly, Part 3, 5:176, 1954.

44. Ng, K. H., and D. B. Spalding. "Turbulence Model for Boundary Layers near Walls," The Physics of Fluids, 15 (Number 1):20-30, January, 1972.

45. Wolfshtein, M. "Convection Processes in Turbulent Impinging Jets." Ph.D. dissertation, Imperial College of Science and Technology Mechanical Engineering Department Report SF/R/I/2, London, England, November, 1967.

46. Harsha, P. T. "Kinetic Energy Methods." Lecture notes at the Short Course on Fundamentals and Applications of Turbulence, The University of Tennessee Space Institute, Tullahoma, Tennessee, April, 1975.

47. Rodi, W., and D. B. Spalding. "A Two-Parameter Model of Turbulence, and its Application to Free Jets," Wärme--und Stoffübertragung, 3 (Number 2): 85-95, 1970.

48. Launder, B. E., A. Morse, W. Rodi, and D. B. Spalding. "Prediction of Free Shear Flows--A Comparison of the Performance of Six Turbulence Models," National Aeronautics and Space Administration SP-321, Washington, D. C., 1973.

49. Jones, W. P., and B. E. Launder. "Prediction of Low Reynolds Number Phenomena with a Two-Equation Model of Turbulence," International Journal of Heat and Mass Transfer, 16 (Number 6):1119-1130, June, 1973.

50. Rotta, J. "Über eine Methode zur Berechnung turbulenter Scherströmungen," Aerodynamische Versunchanstalt Report No. 69A14, Göttingen, 1968.

51. Hastings, R. C. "Turbulent Flow Past Two-Dimensional Bases in Supersonic Streams," Aeronautical Research Council Reports and Memoranda No. 3401, London, England, December, 1963.

52. Hung, Tin-Kan, and E. O. Macagno. "Laminar Eddies in a Two-Dimensional Conduit Expansion," La Houille Blanche Revue International de l'eau, 4:391-401, June, 1966.

53. Alber, I. E., and Lester Lees. "Integral Theory for Supersonic Turbulent Base Flows," American Institute of Aeronautics and Astronautics Journal 6 (Number 7):1343-1351, July, 1968.

54. Hildebrand, F. B. Introduction to Numerical Analysis. New York: McGraw-Hill Book Company, Inc., 1956.

APPENDIX

APPENDIX

The numbers appearing on the left side of the subroutine blocks in the flow chart will be used to describe the function of each subroutine in sequence.

(1) Subroutine CFIT uses the IBM standard subroutines DATSG and DALI. DATSG rearranges the input matrix of x_* and C_p values (see Figure 4-1, page 137) in an ascending order of x_*. DALI interpolates function values of C_p for given argument values of x_* using Lagrangian interpolation with Aitken's Scheme [54]. CFIT returns the interpolated vector, C_p , to the calling program.

(2) Subroutine CALCUE calculates the value of u_{e_*} by solving Equations (4.1a) and (4.2a). It calls the subroutine INTEG which uses Simpson fifth-order quadrature formula for integration to calculate the integral on the right-hand side of Equation (4.1a). The function subprograms, DEF and F, are employed by INTEG and CALCUE to calculate u_{erf_*} and u_* , respectively. The value of u_{e_*} is returned to the calling program.

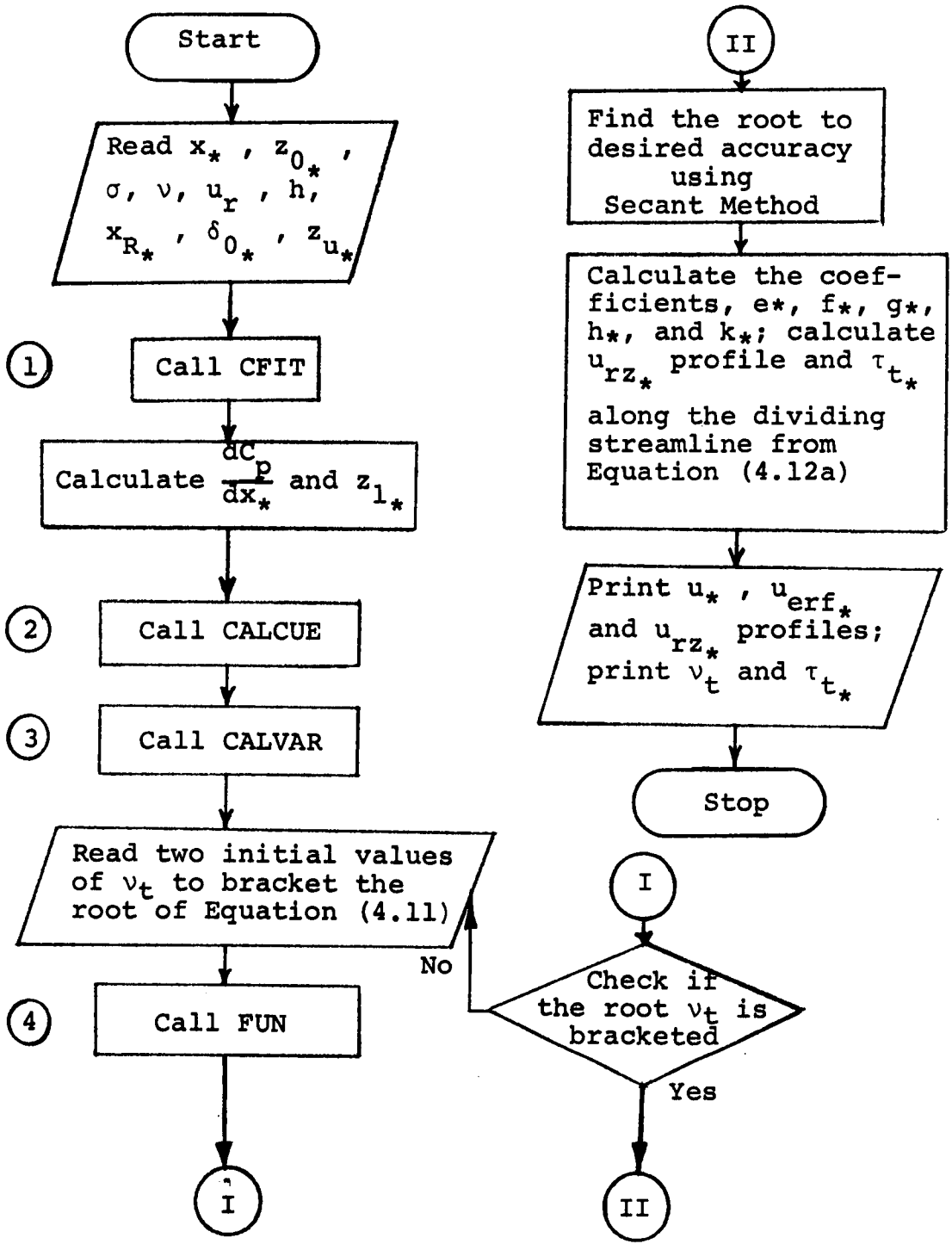
(3) Subroutine CALVAR calculates the values of

$$u_{erf_*}\ ,\ \frac{\partial u_{erf_*}}{\partial z_*}\ ,\ \text{and}\ \frac{\partial^2 u_{erf_*}}{\partial z_*^2}\ \text{at}\ z_{1_*}$$

using the equations associated with Equations (4.5), (4.6),

and (4.7), respectively, in the nondimensional form, and returns them to the calling program.

(4) Subroutine FUN calls the subroutine CALCOF to calculate the coefficients, k_* , h_* , g_* , and e_* , in that sequence each time FUN is called from the calling program. Also, it calculates the function value given by Equation (4.11), and returns it to the calling program.


Start
Read x_* , z_{0_*} , σ, ν, u_r , h, x_{R_*} , δ_{0_*} , z_{u_*}
1
Call CFIT
Calculate $\frac{dC_p}{dx_*}$ and z_{1_*}
2
Call CALCUE
3
Call CALVAR
Read two initial values of ν_t to bracket the root of Equation (4.11)
4
Call FUN
I
II
Find the root to desired accuracy using Secant Method
Calculate the coefficients, e*, f*, g*, h*, and k*; calculate u_{rz_*} profile and τ_{t_*} along the dividing streamline from Equation (4.12a)
Print u_* , u_{erf_*} and u_{rz_*} profiles; print ν_t and τ_{t_*}
Stop
I
Check if the root ν_t is bracketed
No
Yes
II

VITA

Upender Krishen Kaul was born on April 24, 1947, in Srinagar, Kashmir, India. He received his elementary and high school education in Srinagar. In 1966, he was awarded a Bachelor of Science Degree from Jammu and Kashmir University. In 1970, he received a Bachelor of Science Degree in Aeronautical Engineering from Punjab University, India. He worked in the Ministry of Civil Aviation, New Delhi, for some time. In September, 1973, he entered The University of Tennessee Space Institute pursuing a Master of Science Degree in Mechanical Engineering.